

THESIS
2
3
6393 9582

This is to certify that the
dissertation entitled

Optically Transparent Boron-Doped Diamond Electrodes for
Chemical Analysis

presented by

Jason Max Stotter

has been accepted towards fulfillment
of the requirements for the

Doctoral degree in Chemistry

Greg M. Surin
Major Professor's Signature

12-16-04

Date

PLACE IN RETURN BOX to remove this checkout from your record.
TO AVOID FINES return on or before date due.
MAY BE RECALLED with earlier due date if requested.

<u>DATE DUE</u>	<u>DATE DUE</u>	<u>DATE DUE</u>
NOV 12 2006		

OPTICALLY TRANSPARENT BORON-DOPED DIAMOND ELECTRODES FOR CHEMICAL ANALYSIS

By

Jason Max Stotter

A DISSERTATION

**Submitted to
Michigan State University
in partial fulfillment of the requirements
for the degree of**

DOCTOR OF PHILOSOPHY

Department of Chemistry

2004

ABSTRACT

OPTICALLY TRANSPARENT BORON-DOPED DIAMOND ELECTRODES FOR CHEMICAL ANALYSIS

By

Jason Max Stotter

The goal of the research was to develop and characterize the optical and electrochemical properties of boron-doped diamond thin film on quartz to better exploit the superb optical and material stability properties of diamond in the UV-Vis range. Adherent boron-doped diamond thin films were reproducibly deposited on quartz using microwave plasma chemical vapor deposition, with a 0.5% CH₄/H₂ source gas mixture containing 1 to 10 ppm B₂H₆ (200 sccm total gas flow), a system pressure of 45 Torr, and a microwave power of 800 W. Polishing of the quartz with a diamond powder/water slurry resulted in a high density of surface striations which promoted a high instantaneous nucleation density, leading to deposition of a continuous film of small microcrystallites (100-300 nm, 13 nm rms roughness) in a short growth time (1 to 2 h). The useful optical window in the UV-visible region ranged from ca. 225 to 900 nm. Loss of transmitted light was due mostly to reflection and absorption (due to nitrogen impurities and the boron dopant band). The diamond/quartz OTE had a carrier concentration of 10²⁰ cm⁻³ (holes), and low electrical resistivity (0.058 Ω-cm) laterally through the grains and grain boundaries. The electrochemical properties included a wide potential window of nearly 3 V in aqueous solution; a low and stable background current, and fast electrochemical responsiveness for

$\text{Fe}(\text{CN})_6^{-3/-4}$, $\text{Ru}(\text{NH}_3)_6^{+2/+3}$, and $\text{CPZ}^{0/+}$. The spectroelectrochemical performance of the diamond OTE was evaluated in a specially designed, thin-layer cell, using chlorpromazine. Well-defined, thin-layer voltammetry was observed with Q_p^{ox} values independent of scan rate, as expected for thin-layer behavior. The linear dynamic range was from 20 to 100 μM with a limit of detection of 0.5 μM ($\text{S/N} = 3$). A linear Nernst plot was observed with a slope of 56.9 mV ($n = 1$), and an ordinate intercept of 0.41 V. The diamond/quartz OTE possesses material property stability far superior to that of a commonly used OTE material, ITO. After potential cycling in 1 M NaOH and 1 M HNO_3 for over two hours each, optical properties, film morphology, and resistivity of the films were unaffected, and the electrochemistry of $\text{Fe}(\text{CN})_6^{-3/-4}$ and $\text{Ru}(\text{NH}_3)_6^{+2/+3}$ at these electrodes remained active after the polarization treatment. The redox reaction mechanism of the nitro groups of 2-nitrophenol and 4-nitrophenol investigated at the diamond/quartz OTE included an irreversible four-electron reduction at potentials negative of -700 mV, and redox reaction mechanism for 2,4-dinitrophenol appears to be a combination of the features of nitro reduction representing both nitro 2-nitro and 4-nitro groups. When the phenol groups are oxidized, new nitrated species with slightly different nitro group reduction potentials are produced, and there is evidence of polymerization at the electrode surface caused by the oxidation reaction, which may be removed by soaking in warm IPA. These results portend the possibility of using the diamond/quartz OTE for spectroelectrochemical measurements in harsh chemical environments.

Copyright by

JASON MAX STOTTER

2004

ACKNOWLEDGEMENTS

My favorite story from the history of science is that of Tycho Brahe, the Danish nobleman and astronomer with the golden nose. Brahe painstakingly made the most accurate measurements of the movements of heavenly bodies of his time in order to justify the Earth-centered model of the Universe. Following his death, Brahe's assistant Kepler used the measurements to develop his three laws of planetary motion, questioning the Earth-centered model. I hoped in graduate school to be Kepler, but often felt like Brahe. I learned that to research means to re-question, re-plan and re-measure. When I think of the ways I have grown in learning, planning, thinking, and writing while working on this dissertation project, I feel like I am standing at the top of a large mountain that I will likely never climb again. I acknowledge that I did not climb to this point without the generous help and support of many people.

I thank my parents for their encouragement, especially in the most stressful last months of my time at MSU. I am grateful for their encouragement to do the best work possible throughout my life. Dad reminded me to look at my setbacks as possible opportunities. Mom reminded me that what I was studying was difficult, and to keep slogging through to the end. Both set examples in the pursuit of education, the love of knowledge, and in doing right. I thank Justin and Jennifer for their encouragement, for listening to me when I rambled on and on, and for being the best brother and sister anyone could ask for.

Meeting Lauren was the best thing that happened to me while at MSU, and put in perspective life's labors and rewards. I sincerely appreciate and value her sacrifices while I worked on my degree, as well as her encouragement to do my best job. Lauren's perpetual optimism helped me through discouraging days. I also thank Lauren for saving Chapter 5 of this manuscript from the dreaded Microsoft Word monster.

Many past teachers pointed out to me that procrastination and disorganization were holding me back from doing my best work, but Diane Boehm at Saginaw Valley State University helped me to find ways to overcome it. I thank my professors in Chemistry at SVSU for encouraging me to continue my education in graduate school, and for supporting my simple reason for going: to understanding chemistry in more depth.

Dr. Yoshiyuki Show, who taught me how to deposit diamond thin-films, made possible my study of the effect of deposition conditions on the quality of diamond OTEs by graciously depositing many diamond OTEs. Dr. Jerzey Zak, with whom I had the pleasure of working for 6 months, taught me to build small and electronic things, how to prioritize the finding and fixing of experimental problems, and the value of "good junk." Shihua Wang provided the CP-AFM images of diamond/quartz OTEs. Dr. Simon Garrett provided access to the XPS instrument. Dr. David Young at NREL provided the specular reflectance

measurements of diamond/quartz OTEs. Alan McIlwain at Case Western Reserve University provided the boron nuclear reaction analysis data for boron-doped diamond films. Dr. Jim Butler at the Naval Research Laboratory provided the boron-doped diamond freestanding disks.

I owe many thanks to my colleagues in the Swain lab. I have never had the opportunity to work with such a welcoming, encouraging group of people so excited about their work. The lab is a true brain trust. Thank you Jian, Maggie, Matt, Prerna, and Shannon; Ann, Audrey, Bennett, Doug, Gloria, Grace, Josef, Jesse, Karolina, Liz, Pushwinder, Veronika, Wang, Zuzana, and Yang.

In his dissertation, my advisor Greg acknowledged the guidance of his advisor, TK, and hoped that he would serve as the same guide and teacher of careful, quality research in his own students. The growth I have shown in my ability to think through problems, plan experiments guided by theory, interpret data, and report results in person and in writing is evidence that he is living up to this goal. I thank him sincerely for his effort in helping me develop the skills critical to being a scientist through group meeting discussions, encouragement to learn the literature (one article each day), and hours spent revising manuscripts. The best way I can think to show my gratitude is to do good science.

TABLE OF CONTENTS

LIST OF TABLES.....	XI
LIST OF FIGURES	XII
1 INTRODUCTION	1
1.1 Transmission Spectroelectrochemistry and the Need for Stable Optically Transparent Electrodes.....	1
1.2 Properties of Boron-Doped Diamond Electrodes.....	5
1.3 The Development of Boron-Doped Diamond OTEs.....	9
1.4 Outline of the Dissertation	12
2 GROWTH AND CHARACTERIZATION OF BORON-DOPED DIAMOND OPTICALLY TRANSPARENT ELECTRODES	14
2.1 Introduction	14
2.2 Experimental.....	18
2.3 Results and Discussion.....	20
2.4 Conclusion.....	28
3 OPTICAL AND ELECTROCHEMICAL PROPERTIES OF BORON-DOPED	

DIAMOND OPTICALLY TRANSPARENT ELECTRODES	30
3.1 Introduction	30
3.2 Experimental.....	32
3.3 Results and Disussion.....	38
3.4 Conclusion.....	59
4 THE OPTICAL, ELECTRICAL, AND ELECTROCHEMICAL PROPERTY STABILITY OF THE BORON-DOPED DIAMOND/QUARTZ OTE.....	62
4.1 Introduction	62
4.2 Experimental.....	64
4.3 Results and Discussion.....	70
4.4 Conclusion.....	94
5 CYCLIC VOLTAMMETRIC STUDIES OF 2-NITROPHENOL, 4- NITROPHENOL, AND 2,4-DINITROPHENOL AT BORON-DOPED DIAMOND ELECTRODES	96
5.1 Introduction	96
5.2 Experimental.....	106
5.3 Results and Discussion.....	111

5.4	Conclusion.....	135
6	CONCLUSIONS	138
7	REFERENCES	144

LIST OF TABLES

Table 3-1. Carrier concentration and mobility (measured by Hall effect method) and sheet resistivity (measured by four point probe method) data for diamond/quartz OTEs deposited for 1 hour using 1 and 10 ppm B ₂ H ₆	45
Table 3-2. Summary of the cyclic voltammetric data for a diamond/quartz OTE deposited for 1 h using 10 ppm B ₂ H ₆	50
Table 4-1. Resistivity data for ITO/quartz and diamond/quartz OTEs before and after exposure to different organic and aqueous solutions.....	70
Table 4-2. Comparison of ITO and boron-doped diamond resistivity before and after polarization in acidic and alkaline media.....	76
Table 5-1. Cyclic voltammetric peak currents and peak potentials for 4-nitrophenol, 2-nitrophenol, and 2,4-dinitrophenol at a microcrystalline diamond electrode in 10 mM phosphate buffer, pH = 8.0. For 2-nitrophenol and 4-nitrophenol, values are reported for first cycle voltammetric curves. For 2,4-dinitrophenol, values are reported for unchanging voltammetric curves. Case 1 refers to peaks corresponding to 4-nitrophenol, and Case 2 refers to peaks corresponding to 2-nitrophenol. Theoretical peak current values were calculated using an analyte concentration of 0.05 mM, a diffusion coefficient of 9.19×10^{-6} cm ² /sec, and the number of electrons as noted.....	118
Table 5-2. Linear correlation coefficients and slopes of steady-state cyclic voltammetric peak currents vs square root of scan rate ($\mu A/(V/s)^{1/2}$) for 0.05 mM 4-nitrophenol solutions in 10 mM phosphate buffer, pH = 8.0, at three microcrystalline diamond electrodes. Scan rate = 100 mV/sec.....	127
Table 5-3. Steady state cyclic voltammetric peak potentials for 0.05 mM 4-nitrophenol solution in 10 mM phosphate buffer, pH = 5, 6, and 8 at diamond. Values are averaged for measurements at three electrodes. Scan rate = 100 mV/sec.....	129

LIST OF FIGURES

- Figure 1-1. Cyclic voltammetric i-E curves in 1 M KCl for glassy carbon, boron-doped diamond, and ITO electrodes. Scan rate = 100 mV/sec. Geometric area = 0.2 cm² for all electrodes.6
- Figure 1-2. UV-Vis transmission spectra for a freestanding boron-doped (polished), polycrystalline diamond disk and an ITO thin-film deposited on quartz. The film thickness of the ITO was ca. 20 nm, and the diamond disk was 350 μm.7
- Figure 2-1. Clockwise from top-left: A boron-doped diamond thin-film deposited on quartz (10 ppm B₂H₆, 1 h), a polished boron-doped diamond freestanding disk, a polished, boron-doped diamond thin-film deposited on a polished undoped freestanding diamond disk, and a polished, undoped freestanding diamond disk (so-called white diamond). 15
- Figure 2-2. Optical micrograph of boron-doped diamond thin-film deposited for 1 h on a scratched quartz substrate. The optical transparency is evident by the high density of fine scratches seen on the quartz beneath the diamond film.21
- Figure 2-3. Atomic force micrographs of boron-doped diamond films deposited on poorly scratched (a) and properly scratched (b) quartz substrates.22
- Figure 2-4. Raman spectra for boron-doped diamond/quartz OTE (left axis) and HTHP single crystal diamond standard (right axis).23
- Figure 2-5. Optical micrographs of diamond films deposited on quartz substrates for 4 h with a 1% CH₄/H₂ source gas mixture. The quartz substrate was prepared for growth by polishing for different times with different diamond powder particle sizes.26
- Figure 3-1. Diagram of the transmission thin-layer spectroelectrochemical cell: (A) Kel-F body, (B) quartz cuvette, (C) polished quartz, (D) 150-μm silicone gasket, (E) boron-doped diamond OTE, (F) Ag-QRE, and (G) Pt auxiliary electrode.35
- Figure 3-2. UV-visible transmission spectra measured in air for diamond/quartz OTEs deposited for 1 and 2 h. The films were deposited from a source gas mixture of 0.5% CH₄/H₂ and 10 ppm B₂H₆. Film thicknesses are ca. 500 nm

and 1000 nm, estimated by SEM cross-section.....	39
Figure 3-3. Plots of transmittance, reflectance, and absorbance of UV-Vis radiation measured for diamond/quartz OTEs deposited with 10 ppm (top) and 1 ppm (bottom) B ₂ H ₆ . Measurements courtesy of David Young (NREL).	41
Figure 3-4. Plot of the boron concentration in diamond films deposited on p-Si, as determined by boron nuclear reaction analysis, versus the source gas B ₂ H ₆ concentration used during deposition. Deposition time = 1 h. All other deposition conditions were kept constant.	43
Figure 3-5. Cyclic voltammetric i-E curve in 1 M KCl for a diamond/quartz OTE deposited for 1 h with 10 ppm B ₂ H ₆ . Scan rate = 25 mV/s.	47
Figure 3-6. Height-mode (A) and conductivity-probe (B) atomic force micrographs for a diamond/quartz OTE deposited for 1 h with 10 ppm gas phase B ₂ H ₆ . ..	49
Figure 3-7. Background-corrected, thin-layer voltammetric i-E curve for a diamond/quartz OTE, deposited for 1 h using 10 ppm B ₂ H ₆ , in 0.1mM CPZ in 10 mM H ₂ SO ₄ . Scan rate = 2 mV/s.	55
Figure 3-8. (A) UV-visible absorbance spectra at a diamond/quartz OTE, deposited for 1 h using 10 ppm B ₂ H ₆ , for chlorpromazine (CPZ ⁰), at 0.30 V, and the oxidation product (CPZ ⁺), at 0.50 V, in the thin-layer cell. (B) A series of UV-visible absorbance spectra, using the same film, for 0.1 mM chlorpromazine in 10 mM HClO ₄ , as the potential is stepped from 0.32 to 0.47 V vs Ag-QRE.....	57
Figure 4-1. Comparison of UV-vis spectra for as-deposited (A) diamond/quartz and (B) ITO/quartz after a 48 h soak in 1 M NaOH. The spectrum for bare quartz is also shown for comparison.....	72
Figure 4-2. Cyclic voltammetric i-E curves for a diamond/quartz OTE in 1 M HNO ₃ and 1 M NaOH at 25 mV/sec. Electrode geometric area = 0.2 cm ² . ..	75
Figure 4-3. UV-Visible transmission spectra for (a) diamond/quartz OTE after potential cycling in both 1 M HNO ₃ and 1 M NaOH. Potential cycling was performed for 2.5 h	77
Figure 4-4. (a) Cyclic voltammetric i-E curves for an ITO/quartz OTE in 1 M HNO ₃ at 25 mV/sec (cycles number 14-19) (b) transmission spectra for the ITO/quartz OTE after potential cycling in 1 M HNO ₃	78
Figure 4-5. (a) Cyclic voltammetric i-E curves for an ITO/quartz OTE in 1 M NaOH at 25 mV/s (cycle 10) and (B) transmission spectra for ITO/quartz OTE after potential cycling 1 M NaOH. Potential cycling was performed for 10 cycles.....	80

Figure 4-6. Optical micrographs of (A) polarized and unpolarized (1 M NaOH) regions of an ITO/quartz OTE and (B) a polarized (1 M NaOH) ITO/quartz OTE showing the metallic or metal hydroxide phases formed and the bare region where some of these phases were removed by rinsing.	83
Figure 4-7. XPS spectra for (a) In_{3d5} , (b) Sn_{3d5} in an ITO/quartz film before (solid), and after (dashed) polarization in 1 M NaOH.....	86
Figure 4-8. XPS Spectrum for O_{1s} in as-deposited ITO film (solid), and in ITO film after polarization in 1 M NaOH (dashed).....	88
Figure 4-9. AFM micrographs of boron-doped diamond/quartz OTE (top row) and ITO (bottom row). In each row, as deposited (left), after cycling in 1 M HNO_3 (center) and after cycling in 1 M NaOH (right).	90
Figure 5-1. Cyclic voltammetric i-E curve for 0.5 mM NB in 50 mM LiCl at a mercury electrode (radius = 0.046 cm, scan rate = 50 mV/sec). (From McIntire, Blount, 1986).....	98
Figure 5-2. Proposed mechanism for nitrobenzene reduction, based on polarographic measurements at Hg. (From Heyrovsky and Vavricka, 1970)	100
Figure 5-3. Cyclic voltammetric i-E curves for 0.05 mM 2-nitrophenol, 4-nitrophenol, and 2,4-dinitrophenol, in 10 mM phosphate buffer, pH 8.0. Scan rate, 50 mV/sec.....	102
Figure 5-4. UV-Vis absorption spectra for 0.05 mM solutions of 2-nitrophenol, 4-nitrophenol, and 2,4-dinitrophenol in 10 mM phosphate buffer, pH 8.0.	103
Figure 5-5. Cyclic voltammetric i-E curves for 0.05 mM 4-nitrophenol in 10 mM phosphate buffer, pH 8.0 at a polished, planar glassy carbon electrode. (A) First cycle following bubbling with N_2 , (B) tenth cycle (features unchanging with cycle number). Scan rate=50 mV/sec.....	112
Figure 5-6. Cyclic voltammetric i-E curve for 0.055 mM 4-nitrophenol in 10 mM phosphate buffer, pH 8.0, at a planar, microcrystalline diamond electrode. Scan rate=50 mV/sec.	115
Figure 5-7. Steady state cyclic voltammetric i-E curve for 0.05 mM 2-nitrophenol in 10 mM phosphate buffer, pH 8.0 at planar, microcrystalline diamond electrode. Scan Rate = 50 mV/sec.	120
Figure 5-8. Cyclic voltammetric i-E curves for 0.05 mM 2,4-dinitrophenol in 10 mM phosphate buffer, pH 8.0, at a microcrystalline diamond electrode. Steady state curves are presented in (B). Scan rate = 50 mV/sec.....	123
Figure 5-9. i_p values for 4-nitrophenol Peak A (first cycle) at three diamond	

electrodes and theoretically predicted i_p values plotted vs the square root of scan rate. 0.05 mM 4-nitrophenol in 10 mM phosphate buffer solution, pH 6.0..... 125

Figure 5-10. Cyclic voltammetric i-E curves for 0.05 mM 4-nitrophenol in 10 mM phosphate buffer, pH 8.0. 131

Figure 5-11. (a) Cyclic voltammetric i-E curves for 4-nitrophenol (dashed) and 4-nitrocatechol (solid). (b) Background cyclic voltammetric e-E curves after 4-np cycling and 2-propanol rinse (solid) and warm 2-propanol soak (dashed). Scan rate = 50 mV/sec. 133

1 Introduction

1.1 Transmission Spectroelectrochemistry and the Need for Stable Optically Transparent Electrodes

Spectroelectrochemical measurements involve the simultaneous recording of a spectroscopic signal associated with an analyte and a change in redox state brought about by electron transfer with an electrode. Often, the spectrum of the analyte before and after an electrochemical reaction are compared. Identification of an analyte can be made from the characteristics of the spectroscopic signal, the potential at which the electron transfer occurs, and the charge passed associated with the electrochemical reaction. Quantification can be made from both the spectral intensity and the measured current or charge that flows. Furthermore, if multiple analytes are present in a sample and have dissimilar spectra, identification of the individual species can be achieved from the changes in the optical modes upon oxidation or reduction without the need for separation prior to the measurement. Previous applications of spectroelectrochemical measurements include elucidation of redox reaction mechanisms,^{1, 2} analytical sensing of environmentally important inorganic species,^{3, 4} and studies of fundamental electrochemical diffusion processes.⁵ The simplest measurement scheme is in the transmission mode, in which the electrode functions as a transparent optical window as well as a source or sink for electrons. Such a material is known as an optically transparent electrode (OTE). Transmission spectroelectrochemical measurements require an OTE with stable optical and

electrochemical properties.

OTEs come in two types: (1) porous meshes, and (2) transparent solid thin-films. Porous meshes have seen widespread use as OTEs, either in the form of metal minigrids or porous carbon materials. Heineman et al. utilized electroreduction at gold minigrid electrodes in a transmission thin layer cell (TLC) to measure the thermodynamic redox potentials for a series of mammalian heme proteins.⁶⁻⁸ Hawkridge et al. demonstrated the spectroelectrochemical measurement of the reduction of the protein spinach ferredoxin directly at a polymer-modified Au minigrid electrode in a thin layer cell without the need of redox mediators.⁹ The use of vitreous carbon in spectroelectrochemical cells was demonstrated in Norvell and Mamantov for ferri/ferrocyanide, o-tolidine, and MnO_4^- . One advantage of using this type of OTE is the ease of fabrication. Instead of depositing materials on a transparent substrate, materials are simply cut to shape and inserted into the electrochemical cell. Another advantage of these electrodes is a transmission profile that is not selective by wavelength, as long as the pores are larger than the incident wavelengths of light. One disadvantage of this type of OTE is the large background charging current due to the large surface area.¹⁰⁻¹² Another disadvantage is the light throughput, which is limited to ca. 60% for metal minigrids and meshes,⁶ and about 50% for vitreous carbon.¹⁰ This limit is so low because the porosity of the materials is only 50-60%. A third disadvantage for metal minigrids is fragility of the material that limits the useful lifetime of cells constructed using them.⁷

The first reported spectroelectrochemical measurement was made using a thin-film OTE, Sn oxide coated on glass.¹³ Kuwana and Winograd demonstrated the relationship between the change in absorbance of a ferri/ferrocyanide solution and the current response as it was oxidized and reduced at a transparent tin oxide electrode. Hawkrige et al. demonstrated oxidation of Cu at a tin oxide electrode in a thin-layer transmission cell, which lead to the formation of CuO deposits that catalyzed the oxidation of Cu(II) ethylenediamine. The oxidation of Cu(II) ethylenediamine was followed spectroscopically.¹⁴ Hawkrige et al. also measured the dependance of the redox kinetics of myoglobin on ligand identity at ITO electrodes by cyclic voltabsorptometry.¹⁵ A series of papers by Heineman et al. reported on the electrochemically generated change in optical properties of several inorganic systems of environmental interest using an ITO electrode applied in the ATR configuration. The pollutants were sequestered in a sol-gel material deposited on the ITO. Saavedra et al. reported on the spectroelectrochemical detection of submonolayer concentrations of adsorbed methylene blue and ferri/ferrocyanide at an ITO/glass composite ATR device.³ Through careful design of the optical properties of the multi-layer optical device, Saavedra et al. demonstrated the first broadband spectroelectrochemical sensing in the ATR mode for a wide range of the UV-visible spectrum (500 to 700 nm). Absorption spectra of submonolayer amounts of cytochrome C adsorbed on the device surface were recorded.¹⁶ The advantage of using these materials is the high light transmission possible due to

the thinness of the deposited films. These films are also mechanically robust, as they are supported by a substrate.

The indium tin oxide (ITO) electrodes is by far the most commonly used OTE. It typically consists of a ca. 20 nm thick layer of semiconductive metal oxide that is vapor deposited on glass or quartz. While ITO has a high light throughput for wavelengths above 300 nm and is highly conductive, it has physical and chemical properties that limit its application. For example, it is unstable in acidic environments and in some chlorinated organic solvents (e.g., dichloromethane),¹⁷ as well as during cathodic polarization. For example, the material's morphology, microstructure, and chemical properties are altered during cathodic polarization and anodic polarization, which leads to increased film resistance and decreased optical throughput.^{18, 19}

The application of ITO as an OTE in harsh chemical environments is restricted because of the limited stability of the electrode material. A more stable OTE material would enable more widespread application of this informative technique. Considering the shortcomings of existing OTE materials, the ideal OTE would possess (1) a wide optical and potential window, (2) a low and stable background current, and (3) stable optical and electrochemical properties during anodic and cathodic polarization and exposure to harsh chemical environments. Diamond deposited on quartz possess all of these requisite properties and is a new material for use in the UV-Vis region of the electromagnetic spectrum.

1.2 Properties of Boron-Doped Diamond Electrodes

Diamond consists of a crystal lattice of sp^3 -bonded carbon atoms. It is the densest and hardest natural material. Diamond can be synthetically produced by two methods: (1) high temperature and high pressure methods in the presence of a catalyst,²⁰ and (2) low pressure, low temperature chemical vapor deposition (CVD) from a carbon-containing source gas mixture.²¹ CVD methods diamond materials are usually polycrystalline with randomly oriented crystallites and grain boundaries that contain a mixture of sp^2 - and sp^3 -bonded carbon. Diamond is naturally an excellent electrical insulator, but it can be made electrically conducting by doping with boron. Boron dopant atoms substitute for carbon atoms in the crystal lattice during growth and serve as electron acceptors with an activation energy of ca. 0.37 eV.²² As the doping level increases, an acceptor band forms above the valence band, rather than a discrete energy level, with an activation energy as low as 0.01 eV. This results in semiconductor conductivity.^{23, 24}

In recent years, the use of boron-doped diamond thin-films electrodes in electrochemical measurements has received much attention. Much of the work has involved characterization of the physical and electrochemical properties of polycrystalline boron-doped diamond and studying electrode response toward a variety of aqueous and nonaqueous redox systems.^{22, 23, 25-37} Diamond possesses attractive electrochemical properties that set it apart from other

carbon electrodes. Several of these are (1) a low and stable background current over a wide potential range, (2) a hydrogen-terminated surface that is resistive to adsorption and fouling by polar molecules, (3) a wide potential window in aqueous media, (4) morphological and microstructural stability at extreme

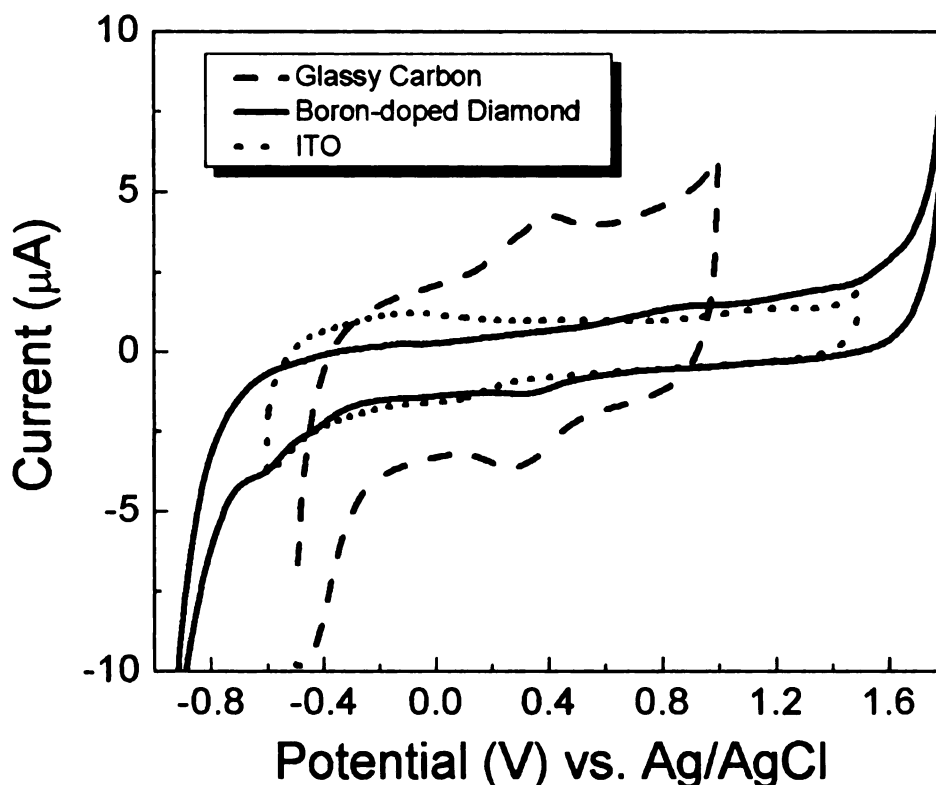


Figure 1-1. Cyclic voltammetric i-E curves in 1 M KCl for glassy carbon, boron-doped diamond, and ITO electrodes. Scan rate = 100 mV/sec. Geometric area = 0.2 cm² for all electrodes.

anodic and cathodic potentials, and large current densities, and (5) relatively rapid electrochemical kinetics for some redox systems without pretreatment.

Figure 1-1 presents a comparison of the background cyclic voltammetric i-E curves for a boron-doped diamond electrode, glassy carbon (another form of

carbon electrode consisting of a network of sp^2 -bonded carbon ribbons) and indium tin oxide (ITO) (a commonly used optically transparent electrode material), all in 1 M KCl. The larger potential window and lower background current for diamond are evident.

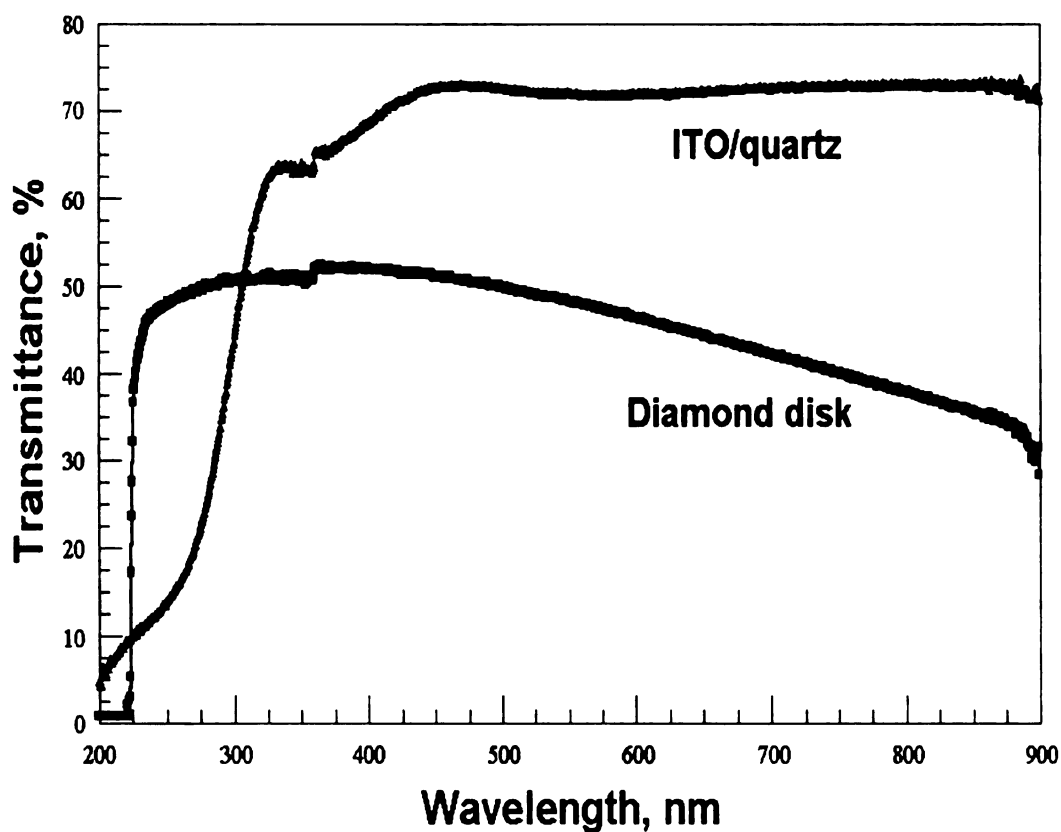


Figure 1-2. UV-Vis transmission spectra for a freestanding boron-doped (polished), polycrystalline diamond disk and an ITO thin-film deposited on quartz. The film thickness of the ITO was ca. 20 nm, and the diamond disk was 350 μ m.

Diamond possesses notable optical properties, as well. Pure diamond has the largest refractive index of any natural material, as well as an optical window that encompasses most of the UV-visible and IR regions of the

electromagnetic spectrum. The optical window is the largest of any natural material.³⁸ Pure diamond is a wide bandgap material with bandgap energy of ca. 5.5 eV. This translates into an absorption cutoff in the UV region of the electromagnetic spectrum at ca. 225 nm. Figure 1-2 compares the UV-vis transmission spectra for a boron-doped, freestanding diamond disk and ITO on quartz. The diamond exhibits higher transmission between 225 and 300 nm, but is limited to ca. 60% transmission in the 300-900 nm range due mainly to reflection losses as the refraction index is quite high (2.41 at 591 nm).³⁹ Further transmission losses in the UV-Vis extending into the near IR are due to the boron dopant band. While the optical properties of polycrystalline, boron-doped diamond films are different from those of pure diamond, they can be controlled, to a large extent, by manipulation of the deposition conditions.

Diamond electrodes also possess superb morphological and microstructural stability--an important property of an OTE. The morphological and microstructural stability of a microcrystalline diamond film supporting Pt catalyst particles was demonstrated after two hours of anodic polarization in 85% H₃PO₄.⁴⁰ During the polarization, the diamond was heated to 170°C and current densities up to 0.1 A/cm² were passed. Diamond electrodes exhibit no observed change in activity of several redox systems after months of storage without any polishing or pretreatment prior to use, other than soaking in distilled 2-propanol.⁴¹ The surface of boron-doped diamond electrodes is hydrogen terminated, which renders the material resistant to molecular adsorption and fouling, particularly by

polar molecules.⁴² Two classes of analytes that can be stably detected with diamond are polyamines⁴¹ and chlorophenols.⁴³ Detection of these analytes with other electrodes is typically prevented by significant electrode fouling.

1.3 The Development of Boron-Doped Diamond OTEs

There has been little work performed, thus far, on the development of new optically transparent electrode materials, including diamond, for spectroelectrochemical measurements. The diamond OTEs reported on so far have been fabricated in the forms of a freestanding disk and a thin-film deposited on a transparent quartz or Si substrate. Zak et al. investigated a freestanding boron-doped diamond disk as an OTE for spectroelectrochemistry in the UV-Vis region of the electromagnetic spectrum.⁴⁴ The polished disk, due to the large thickness (380 μm), transmitted light with a nominal transmission of ca 5.5% at 225 nm, decreasing to ca. 0.1% at 800 nm. An aqueous potential window from -1.5 to +1.5 V vs Ag/AgCl was demonstrated. The OTE was then integrated into a thin-layer spectroelectrochemical cell for transmission measurements in the UV-Vis. Absorption spectra of $\text{Fe}(\text{CN})_6^{-3/4}$ ($\lambda_{\text{max}} = 425 \text{ nm}$) and methyl viologen were recorded at different potentials and the changes in UV-vis spectra were correlated with changes to the systems' redox state. For example, as MV^{2+} was reduced to $\text{MV}^{\bullet+}$, the absorption maximum at 257 nm decreased, while absorption modes at 398 (MV^0) and 605 nm ($\text{MV}^{\bullet+}$) increased. This change in the absorption spectrum was completely reversible with applied potential. As the potential was made

more negative, remaining MV^{2+} and MV^{+} in the cell was reduced to MV^0 . The mode at 257 nm disappeared, the modes at 605 nm decreased, leaving only the mode at 398 nm. Absorbance changes in the thin layer cell were used to calculate the molar absorption coefficients, which all agreed with literature values. This research demonstrated that boron-doped diamond is a practical OTE material for reproducible UV-vis spectroelectrochemical measurements.

Haymond et. al. used a freestanding boron-doped diamond disk to study the redox chemistry of ferrocene in the UV-vis region of the electromagnetic spectrum by transmission spectroelectrochemical measurements.^{45, 46} The diamond OTE, applied in a new thin layer spectroelectrochemical cell, was used to record stable and reproducible absorption spectra for ferrocene ($\lambda = 252, 285$ nm) as a function of the electrode potential in acetonitrile. This work demonstrated the capability of boron-doped diamond to function as an OTE material in nonaqueous media.

Martin and Morrison reported on attenuated total reflectance IR measurements with an optically transparent diamond film during anodic polarization in acid. This goal was to learn what types of oxygen functional groups form on the diamond surface during anodic polarization in H_2SO_4 . An increase in the surface concentration of O-H ($\lambda = 3240$ cm^{-1}) and C-O ($\lambda = 1100$ cm^{-1}) stretching bands was detected after electrochemical polarization in 0.5 M H_2SO_4 .

Haymond et al. reported active and stable electrochemical response for horse heart cytochrome c at a boron-doped diamond thin-film electrode, without pretreatment or surface modification.⁴⁷ At a freestanding diamond OTE (380 μm thick), in a thin layer spectroelectrochemical cell with a pathlength of 100 μm , UV-Vis difference spectra for the oxidized and reduced form were measured, allowing calculation of the formal reduction potential. At a boron-doped diamond/Si OTE, IR difference spectra of the oxidized and reduced forms of the protein were measured, allowing detection of amino acid side chain and peptide backbone vibrations.⁴⁸

While the use of diamond OTEs has been reported on to some extent,⁴⁸ the existing OTEs (freestanding disk) that are transparent in the UV-vis region of the electromagnetic spectrum are difficult to fabricate (long deposition times for thick films and laborious mechanical polishing) and do not offer ideal optical transmission.

The purpose of this dissertation research was to demonstrate a new form of diamond OTE, thin-film diamond deposited on quartz. The diamond/quartz OTE will expand the useful realm of spectroelectrochemical measurements beyond the shortcomings of ITO by exploiting the optical transparency, attractive electrochemical properties, and stability of boron-doped diamond films. This research sought to answer the following questions. (1) Can adherent, boron-

doped diamond thin-films be reproducibly deposited on quartz? (2) What are the optical and electrochemical properties of these diamond/quartz films? (3) How can these basic properties be manipulated through changes in deposition conditions to optimize the light throughput and electrical conductivity? (4) Can the diamond/quartz film be used as an OTE to make reproducible spectroelectrochemical measurements in the UV-Vis region of the electromagnetic spectrum? (5) How does the diamond/quartz OTE compare to the most commonly used OTE material, ITO, in optical properties, electrical conductivity, and chemical stability? (6) What is the voltammetric response and UV-Vis spectroscopy of a redox system of a family of environmental pollutants not measurable in the transparent region, or reducible within the potential window, of ITO for a possible future application of the diamond/quartz OTE.

1.4 Outline of the Dissertation

This work details the development and characterization of a polycrystalline, boron-doped diamond thin-film material, deposited on quartz, which satisfies the conditions for an ideal OTE. After describing the material and its fabrication in Chapter 2, the manipulation of its optical and electrochemical properties is described in Chapter 3. In Chapter 4, the stability of the diamond/quartz OTE's optical and electrochemical properties are demonstrated, as compared to ITO. A study of the chemical changes that occur in ITO films during the blackening process is also presented. An ideal application for the stable diamond/quartz OTE is a spectroelectrochemical assay for nitroaromatics in harsh

chemical environments. In the development of such an assay, preliminary spectroscopic and electrochemical measurements of model nitroaromatics at the diamond/quartz OTE are necessary. The electrochemistry of nitrophenols at boron-doped diamond electrodes is presented in detail in Chapter 5.

2 Growth and Characterization of Boron-Doped Diamond Optically Transparent Electrodes

2.1 Introduction

One type of diamond OTE architecture is a freestanding boron-doped diamond disk, as reported on by Zak et al.⁴⁴ and Haymond et al.⁴⁵ This disk was relatively thick (ca. 350 μm) and laborious to prepare. An optical image of such a diamond disk is presented in the top right of Figure 2-1. The disk has a dark blue hue due to absorption by the boron dopant atoms at wavelengths in the near IR, extending into the far visible. For comparison, the optical clarity of an undoped, polished “white” diamond can be seen in the image in the lower left. The bottom right image shows the same “white” diamond coated with a thin layer of boron-doped diamond. Polishing of the doped diamond layer is necessary to reduce the surface roughness of the polycrystalline film, which causes light scattering. Scattering and reflection losses reduce the light throughput for unpolished films and can preclude their use in UV-Vis spectroelectrochemical measurements. Even with the polishing, these disks are sometimes plagued by an uneven doped diamond layer across the surface. This leads to uneven light transmission and conductivity. Such an OTE is shown in the lower right image of Figure 2-1. Another diamond OTE architecture is a thin-film of boron-doped diamond coated on an optically transparent substrate. Morrison et al.⁴⁹ and Haymond et al.⁴⁷ both reported diamond thin-films deposited on undoped Si substrates for use in IR.

Stotter et al. reported on diamond thin-films deposited on quartz for use in UV-Vis.¹⁷

Our approach was to deposit a thin, continuous layer of boron-doped diamond on quartz. This type of OTE is easier to fabricate than the freestanding disk, exhibits excellent electrochemical properties, and possesses greater light throughput than the disk.

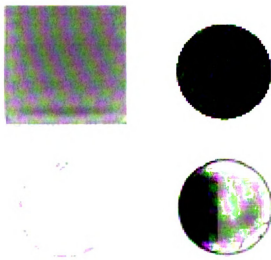


Figure 2-1. Clockwise from top-left: A boron-doped diamond thin-film deposited on quartz (10 ppm B_2H_6 , 1 h), a polished boron-doped diamond freestanding disk, a polished, boron-doped diamond thin-film deposited on a polished undoped freestanding diamond disk, and a polished, undoped freestanding diamond disk (so-called white diamond).

An example of a diamond/quartz OTE is shown in the top left image of Figure 2-1. The film was deposited using conditions that lead to the formation of nanometer sized crystallites.¹⁷ The small (with respect to the wavelength of light) crystallites also obviate the need for polishing, as they are of smaller scale than

the wavelengths passed. Quartz provides adequate mechanical support for the thin-film and is transparent in the 200-900 nm (visible) range of the electromagnetic spectrum.

Coating diamond on glass or quartz substrates is not without challenge. There have been reports of diamond deposition on transparent glass substrates using microwave plasma assisted chemical vapor deposition (MPCVD). Kim et al. deposited diamond microcrystallites on glass substrates.⁵⁰ Their goal was to increase the initial nucleation density on the substrate surface through cyclic control of the methane concentration in the source gas mixture during the early stages of deposition. The glass substrates were pretreated by scratching the surface with 1 μm diamond powder in an acetone slurry. The growth conditions were 200 sccm of H_2 , with CH_4 added at a flow rate of 2-8 sccm. The plasma was ignited with both the H_2 and CH_4 flows on, and then the CH_4 flow was cycled on and off at intervals of 2 min for the first ten minutes. The results clearly demonstrated a higher nucleation density for diamond growth can be achieved using this cyclic technique than without, although SEM images showed incomplete diamond film coverage even after 6 h of growth. Such an undoped film is not suitable for use as an OTE because of the high electrical resistance.

Deposition of diamond on borosilicate glass was reported by Ulczynski et al. using MPCVD. The glass was pretreated with both chemical etching and scratching with diamond powder, and seeding with 0.25 μm diamond powder

prior to growth.⁵¹ The deposition pressure was varied from 5 to 15 Torr, and the plasma power was kept constant at 1 kW microwave power. The conditions were chosen for diamond deposition at temperatures below the glass substrate thermal strain temperature of <500°C. Deposition on substrates scratched with 0.25 μm diamond powder resulted in microcrystallites ca. 0.3-0.4 μm in diameter, and a film thickness of 0.8 μm after an 8 h growth. The optical throughput was limited by scattering when the films were rough, with crystallites of comparable size or larger than the wavelength of light transmitted. When the crystallites were smaller than the wavelength of transmitted light, the optical throughput was dominated by interference between the light reflected from the air/diamond and diamond/glass interfaces. The results demonstrated that continuous, adherent thin-films of diamond may be deposited on glass materials with good adhesion even with the difference in thermal expansion coefficients, when deposition temperature was kept below their thermal strain point temperature.

In this Chapter, the fabrication of a thin, adherent, boron-doped diamond layer on quartz is discussed. The growth conditions required to achieve a continuous diamond film composed of crystallites smaller than 0.5 μm that is electrically conductive, optically transparent, and well adhering to quartz are discussed. The research sought to answer the following questions: (1) can a thin, continuous boron-doped diamond film be deposited reproducibly on quartz, (2) what are the critical factors in the deposition of continuous, adherent, optically transparent and electrically conducting diamond films on quartz?

2.2 Experimental

Diamond Film Deposition. Quartz substrates (1 x 1 x 0.1 cm³) were cut from polished stock, 0.1 cm in thickness. Each quartz substrate was prepared for deposition by mechanically scratching for 5 min with 0.1 μm diamond powder slurried in ultrapure water. The substrate was polished on a Buehler diamond-impregnated, polymer lapping disk attached to a glass optical flat for stability. The polished surface was cleaned of polishing debris by consecutive 5 min ultrasonications in ultrapure water, 2-propanol, acetone, 2-propanol, and ultrapure water. *Removal of the polishing debris from the polishing striations is a key step in the growth of a smooth diamond film on quartz!* The substrate was then dried under a stream of N₂ gas. These polishing and cleaning steps are essential for the deposition of a high-quality boron-doped diamond film on quartz, as the fine scratching of the surface provides a high initial density of nucleation sites. This leads to the growth of a relatively smooth and continuous film in a short period of time. The high nucleation density leads to the formation of small crystallites of diamond, which is essential for minimizing light scattering losses. Before placing the scratched and cleaned substrate into the growth chamber (1-3 at a time), they were first inspected using an Olympus metallurgical microscope (Scope BX60M, Olympus America, Inc., Melville, NY) fitted with a digital camera (DP11, Olympus America, Inc., Melville, NY). Images were collected using an optical polarization filter to highlight scratches. Substrates with a low fraction of non-uniform polishing striations were rejected, as were substrates containing a

large number of pits or large scratches induced by handling.

A boron-doped diamond film was deposited on the scratched quartz by MPCVD using a CH₄/H₂ source gas ratio of 0.5% with 10 ppm B₂H₆ added for doping (0.1% B₂H₆ in H₂). The total gas flow was 100 sccm, the system pressure was 45 Torr, and the microwave power was 600 W. The substrate temperature during deposition was estimated to be 800°C using an optical pyrometer. The growth time was either 1 or 2 h. Following film deposition, the CH₄ and B₂H₆ gas flows were turned off, and the film remained exposed to a H₂ plasma (atomic hydrogen) for 10 min at 600 W and 45 Torr. This was followed by substrate cooling in the presence of atomic hydrogen by reducing the pressure and power. Postgrowth annealing in the presence of atomic hydrogen is essential for removing any adventitious sp²-bonded non-diamond carbon impurity and hydrogen terminating the surface. Adventitious sp²-bonded non-diamond carbon impurity has been shown to affect the electrochemical properties of boron-doped diamond electrodes^{52, 53} and will also reduce the light throughput due to absorption in the visible region. The slow cooling also lessened the film stress. The resulting diamond films were 1 cm² and estimated to be <500 nm in thickness after the 1-h growth and <1000 nm after the 2-h growth. The electrical resistivity of these films was 0.06 Ω-cm, or less, as measured with a tungsten 4-point probe.

Raman Spectroscopy. The Raman spectrograph (Raman 2000, Chromex Inc.,

Albuquerque, NM) consisted of a diode-pumped, frequency-doubled Nd:YAG laser (532 nm excitation at 50 mW, Coherent) used to illuminate the sample surface. The Raman scattered light was collected in a 180° backscattered configuration with a confocal objective lens. Spectra were collected with an incident power density of ca. 500 kW/cm² (100 mW at the sample and 5 μm diameter spot size). The collected light was dispersed with a Chromex 500is spectrograph with a pathlength of 0.5 m and holographic grating with 600 grooves/mm. The dispersed light was detected with a thermoelectrically cooled CCD (1024x246, Andor Tech, Ltd., South Windsor, CT). The spectrograph was calibrated at several points using the spectrum of acetaminophen.

Atomic Force Microscopy (AFM). Atomic force micrographs were captured in the contact mode (in air) with a Nanoscope IIIa instrument (Digital Instruments/Veeco metrology Group, Santa Barbara, CA) using 100-μm narrow-leg, triangular cantilevers with a spring constant of 0.06 N/m.

2.3 Results and Discussion

An ideal diamond OTE for UV-Vis transmission spectroelectrochemical measurements would be an ultrathin, continuous film with a nominal grain or feature size less than the shortest wavelength of light used to minimize light scattering losses.³⁹ Pretreatment of the quartz by uniform scratching and cleaning of these scratched is necessary to achieve such a film. Proper

scratching and cleaning produces a high nucleation-site density on an otherwise smooth quartz surface with the clean striations serving as the initial nucleation sites. This is a key step in the deposition process! The optical micrograph in Figure 2-2, captured through a polarization filter, reveals the high density of scratches on the quartz surface underneath the transparent diamond film. A high initial nucleation density leads to the formation of a thin and continuous film

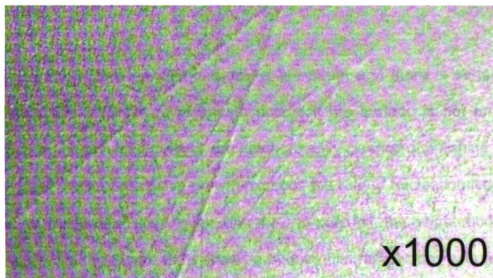


Figure 2-2. Optical micrograph of boron-doped diamond thin-film deposited for 1 h on a scratched quartz substrate. The optical transparency is evident by the high density of fine scratches seen on the quartz beneath the diamond film.

consisting of small crystallites. The adhesion of the diamond to quartz is superb, even after handling, as this one was, for many experiments.

The $3 \times 3 \mu\text{m}^2$ height-mode AFM image, presented in Figure 2-3A, illustrates the nature of diamond growth on a poorly prepared quartz substrate.

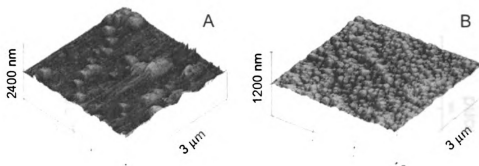


Figure 2-3. Atomic force micrographs of boron-doped diamond films deposited on poorly scratched (a) and properly scratched (b) quartz substrates.

Isolated clusters of large diamond grains are seen, and there is certainly no continuous film. This type of growth occurs if the surface is not uniformly scratched or the resulting grooves are not thoroughly cleaned of polishing debris. In this case, the rate of crystal growth exceeds the rate of nucleation leading to isolated diamond deposition, even after 4 h. In contrast, the height-mode AFM image presented in Figure 2-3B shows a nodular film morphology with features having a nominal diameter of $\approx 100\text{-}200$ nm. The film is relatively smooth and continuous over the surface. The rms surface roughness was found to be 13 nm.

Figure 2-4 presents Raman spectra for a Type IIa HTHP diamond standard reference sample (Harris International, New York, NY) and a boron-doped diamond thin-film deposited on quartz. The first order phonon mode of diamond is Raman active and has been used extensively for characterization of diamond material quality.⁵⁴⁻⁵⁷ The FWHM of the diamond phonon peak is inversely related to phonon lifetime, and therefore to the crystalline quality. The

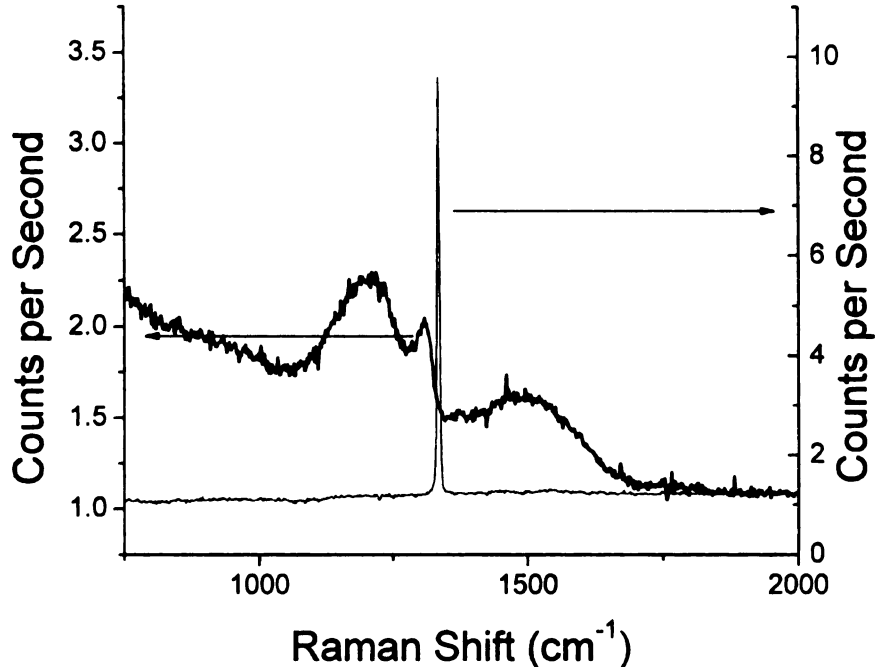


Figure 2-4. Raman spectra for boron-doped diamond/quartz OTE (left axis) and HTHP single crystal diamond standard (right axis).

FWHM for the diamond phonon line is ca. 2 cm^{-1} , indicating a high quality, phase pure diamond crystal low in defects. A Fano interaction causes a shift to lower wavenumbers of the diamond phonon peak, as seen for the boron-doped diamond film on quartz. The shift is caused by a resonance between the boron impurity band and the lattice phonon.²⁴ It is also significantly attenuated due to the increased optical density caused by the boron doping. The phonon peak for the diamond standard is symmetrical about 1332 cm^{-1} , and the baseline at wavenumbers below the peak is flat. Therefore, no Fano interaction is observed for the standard, which is undoped. The baseline at wavenumbers above the peak is also flat, where scattering by sp^2 -bonded carbon is observed (ca. 1500

cm⁻¹). With visible excitation, the Raman cross-section for sp²-bonded carbon (graphite as the model) is 50 times larger than that for diamond. Therefore, the technique is quite sensitive to the presence of sp²-bonded carbon. The absence of scattering intensity in this region indicates there is no measurable contribution from graphitic impurity in the diamond standard.

The Raman spectrum for the diamond/quartz OTE shows scattering intensity for the diamond one-phonon mode at 1312 cm⁻¹. The most striking difference between the two spectra is the lower intensity of the diamond phonon peak for the boron-doped diamond/quartz OTE. This is likely due to a reduced number of scatterers, given the thinness of the thin boron-doped diamond film. The boron-doped diamond film on quartz is ca. 500 nm thick, as estimated by SEM cross-section, while the standard is ca. 500 μm thick. The one-phonon mode for the diamond/quartz OTE is centered at 1312 cm⁻¹, and significantly shifted from the expected position at 1332 cm⁻¹. The observation of a Fano effect is expected in a film of dopant concentration of ca. 10¹⁹ cm⁻³ or greater (boron nuclear reaction analysis measurements, detailed in Chapter 3, revealed a boron concentration of ca. 3200 ppm, or ca. 5x10²⁰ cm⁻³). The Fano interaction shifts the diamond phonon peak to lower wavenumbers and disrupts the peak's baseline at wavenumbers below that of the diamond peak. The 20 cm⁻¹ shift may be also partly due to tensile stress in the film. Polycrystalline diamond films deposited on substrates may experience one of two types of stress. First, there can be an intrinsic tensile stress.⁵⁸ Second, there can be a compressive stress

upon post-growth cooling, caused by the mismatch in thermal expansion coefficients.⁵¹ Mermoux et al. have demonstrated that compressive stresses in the diamond film cause an increased shift in the diamond Raman peak, and tensile stresses cause a decreased shift.⁵⁹ The shift observed in this case, to lower wavenumbers, indicates tensile stress is stronger in this film than compressive stress, supporting the strong adhesion of the film to the quartz, and the ability to grow at a temperature below the quartz strain temperature. The FWHM of the one phonon line for the diamond/quartz OTE is ca. 30 cm^{-1} , much larger than the ca. 2 cm^{-1} seen for HTHP standard, or even the ca. 8 cm^{-1} typically observed for polycrystalline diamond films grown on Si.⁵² A peak intensity at 1200 cm^{-1} is observed, which has been attributed in heavily boron-doped diamond films to asymmetry in the diamond lattice caused by boron atoms.²⁴ The FWHM to a first approximation is usually related to the phonon lifetime. Grain boundaries and defects reduce the lifetime. The diamond film on quartz is composed of small nodular features 100-200 nm in size. The spectrum also shows a peak centered at 1500 cm^{-1} . We suppose that the scattering intensity results from a combination of sp^2 -bonded carbon at the quartz/diamond interface and sp^2 -bonded carbon atoms in the grain boundaries.⁵⁴

The images in Figure 2-5 reveal how the surface scratching procedure affects the morphology and crystallite size of the resulting diamond film. Presented are optical micrographs of undoped diamond films deposited under identical growth conditions on quartz substrates that were pretreated by different

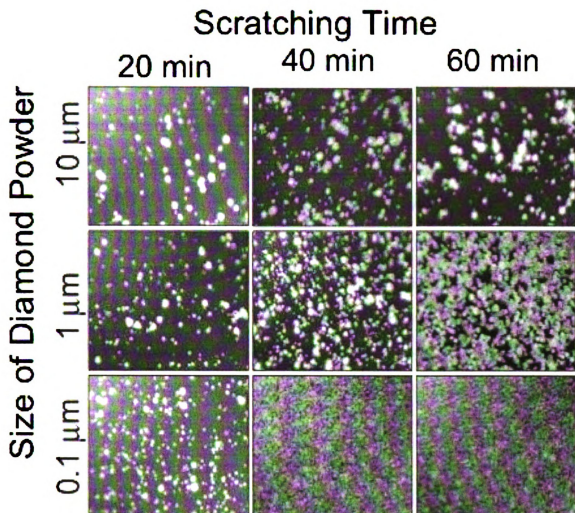


Figure 2-5. Optical micrographs of diamond films deposited on quartz substrates for 4 h with a 1% CH_4/H_2 source gas mixture. The quartz substrate was prepared for growth by polishing for different times with different diamond powder particle sizes.

polishing steps. The CH_4/H_2 source gas ratio for all the growths was 1%, and the system pressure was 45 torr. All deposition times were 4 h using a microwave power of 800 W. The difference between the nine films is the amount of time the quartz substrate was scratched in a diamond/water slurry (20, 40, and 60 min), and the size of the diamond powder used for scratching (0.1, 1, and 10 μm)

nominal diameter).

The substrate polished for 20 min with 10 μm powder exhibits the least continuous coverage and a wide range of features. Uncoated regions are dark and the diamond growths are light. The wide range of feature sizes (clusters of diamond particles) is due to the differences in rate of crystal growth across the surface. As the scratching time increases for the three films polished with 10 μm diamond powder, the density of diamond deposits increases slightly, but at the longest scratching time, the deposits are still isolated and not continuous over the surface. The increased scratching time increases the nucleation density somewhat due to a higher number of scratches, but the scratches are still large in size. As a result, diamond growth occurs as large, isolated crystallites or aggregates of crystallites.

For the quartz scratched with a 1 μm diamond powder slurry, the same trend is observed--a higher nucleation density at longer scratching times. Importantly, the diamond crystallites are noticeably smaller, compared to those on quartz scratched with 10 μm diamond powder. It is noteworthy that the film grown on the quartz polished for 60 min has a high nucleation density such that many of the crystallites are interconnected.

For the quartz scratched with a 0.1 μm diamond powder slurry, the diamond particles are even smaller in size due to the smaller scratches. The

high scratch density promotes a high instantaneous nucleation density and the formation of small crystallites of diamond. Complete film coverage is seen for the 40 min deposition. The same trend holds as for the other two powders; increasing scratching time leads to a higher nucleation density and more complete film coverage. Scratching of the quartz substrate plays a significant role in determining the quality of the resulting film. The films were sufficiently conductive to support electrochemical measurements and sufficiently transparent for use as optically transparent electrodes for spectroelectrochemical measurements. A full description of the optical and electrochemical properties of boron-doped diamond/quartz OTEs deposited on quartz, and the adjustment of the above described deposition conditions to improve these properties, are presented in Chapter 3.

2.4 Conclusion

Thin, continuous, boron-doped diamond films can be reproducibly deposited on quartz substrates using MPCVD. The optimum deposition conditions in our CVD reactor design were determined. Also, an appropriate substrate preparation procedure was developed. Raman spectroscopy confirmed the presence of a highly boron-doped diamond film. Atomic force microscopy revealed a relatively smooth and continuous film across the quartz with crystallite size in the 100-300 nm range, and a surface roughness of 13 nm (rms). The substrate preparation by mechanical scratching and cleaning pretreatment procedure is key to the formation of a smooth and well adhering

film. The high density of surface scratches promotes a high instantaneous nucleation density, which leads to deposition of a continuous film of small microcrystallites (100-300 nm) in a short growth time.

3 Optical and Electrochemical Properties of Boron-Doped Diamond Optically Transparent Electrodes

3.1 Introduction

Following the successful deposition of an adherent boron-doped diamond thin-films on quartz, the optical and electrochemical properties were comprehensively characterized. The goal of this work was to develop a film with more ideal optical and electrochemical properties. An ideal OTE would have a wide optical window and stable optical properties over a wide range of wavelengths. For the diamond/quartz OTE, the boron doping level must be optimized to make the film sufficiently electrically conducting while maintaining relatively high light throughput. The transmission through diamond is limited by absorbance, scattering, and reflectance losses. The blue hue of the boron-doped diamond film is due to absorption in the far visible and near IR by the boron acceptor band.⁶⁰ Impurity atoms such as nitrogen also cause absorption and scattering in the UV-Vis region.⁶¹ Controlling the dibornate level is important for maximizing the optical transparency. The film thickness can also be varied to control the transparency, according to the Beer's law relationship between light path and absorption. Light scattering is controlled by the surface roughness, which may be controlled by substrate pretreatment procedures, as discussed in Chapter 2.³⁹ In summary, the optical and electrical properties can be controlled by adjustments in the deposition conditions. Reflection at the air/diamond or

solution/diamond interface is also a mechanism for light loss and is governed by diamond's high refractive index (2.41 at 591 nm). In practice, factors that influence the film optical properties of diamond also affect the electrical properties (e.g., electrochemical properties).

An ideal OTE would also possess the following electrochemical properties: good electrical conductivity, a wide and stable potential window, a low and stable background current, and good activity for redox systems without the need for pretreatment. The conductivity of diamond films increases with the boron doping level, which increases the carrier concentration. While the carrier concentration increases, the carrier mobility decreases due to scattering processes. The boron doping level is adjusted by varying the B_2H_6 concentration in the deposition source gas. The wide potential window and the low, stable background current can be controlled during the deposition process by choosing conditions that limit the adventitious incorporation of sp^2 -carbon impurity in the diamond film. Wang et al. described the effect of the ratio of carbon source (CH_4) to hydrogen in the growth plasma on the resulting amount of adventitious sp^2 -bonded carbon in the resulting films.⁵³ The sp^2 -bonded carbon has the effect of narrowing the aqueous potential window and increasing the magnitude of the background current. The films in this research were deposited with a C/H ratio of 0.5%. This ratio was demonstrated to provide a relatively rapid diamond growth rate, but a low adventitious sp^2 -bonded carbon growth rate. All diamond crystallites deposited in hydrogen plasma have a hydrogen-terminated surface, which has been

demonstrated to resist fouling and exhibit relatively rapid electron transfer kinetics for several inner-sphere and outer-sphere redox couples.^{52, 62}

This research sought to answer the following questions: (1) what are the basic optical and electrochemical properties of the diamond/quartz OTE, (2) how can these properties be optimized for increased light throughput and electrical conductivity through manipulation of the deposition conditions, and (3) do these films offer sufficient light transmission and electrical conductivity to support reproducible spectroelectrochemical measurements in the UV-Vis region of the electromagnetic spectrum? The surface roughness and particle size were deemed to be close to optimal for use in UV-vis measurements, as described in Chapter 2, as was the 0.5% C/H ratio in the source gas mixture. The two remaining changes to the deposition conditions were variation of the film thickness (growth time) and the boron dopant concentration (source gas B₂H₆). The following is an explanation of how boron-doped diamond/quartz OTE properties were adjusted by changes in the deposition conditions, along with a detailed characterization of the optical and electrochemical film properties. A transmission spectroelectrochemical measurement of an organic molecule, chlorpromazine, was made to demonstrate the optimized diamond/quartz OTE.

3.2 Experimental

Optical Transmission Measurements. The diamond and ITO OTEs were rinsed with distilled 2-propanol (IPA) and allowed to dry in air, prior to making any

optical measurement. The electrode was mounted vertically for the UV-Visible measurements and was placed orthogonal to and facing the incident light beam. The electrode was held in place over the aperture of the sample holder using a small piece of double-sided adhesive tape along one edge. The spectrum for an uncoated and unscratched quartz substrate, cleaned in the same manner, was used as the background. UV-visible spectra were recorded with a computer-controlled Shimadzu UV-2401 PC spectrophotometer (Shimadzu Corp., Columbia, MD) using a slit width of 5 nm and a 210 nm/min scan rate.

Electrochemical Measurements in a Glass Electrochemical Cell. Electrochemical measurements were made with a computer-controlled potentiostat (Model 650A, CH Instruments, Inc., Austin, TX) in a three-electrode configuration. No iR correction was used in any of the reported measurements. The electrodes were clamped over the bottom opening of a single-compartment, glass electrochemical cell.⁶³ A viton o-ring (i.d. 0.5 cm), placed between the cell opening and the electrode surface, ensured that a controlled nominal surface area of 0.2 cm² was exposed to the electrolyte solution. Contact was made to the working electrode by pressing a piece of nickel foil against the surface. The foil was roughly the size of the electrode with a portion in the center removed just larger in diameter than the o-ring. A spacer was cut from a rubber sheet to the same dimensions as the nickel foil and was used to press the foil against the electrode surface. The o-ring was sonicated for 10 min in ultrapure water, rinsed with distilled IPA, and dried under a stream of N₂ (before mounting a diamond electrode in the cell).

Once mounted in the cell, the electrode was exposed to IPA and allowed to soak for 30 min. The electrode was then rinsed thoroughly with distilled water, and the cell was filled with the electrolyte solution of interest. Nitrogen was bubbled through the solution for 10 min to remove dissolved oxygen. All measurements were made with the solution blanketed by the gas. The auxiliary electrode was a large-area carbon rod, and the reference was a commercial Ag/AgCl electrode filled with 4 M KCl saturated with AgCl. Both the auxiliary and reference electrodes were placed in fritted capillaries filled with the supporting electrolyte. The frit for the auxiliary electrode did not add significant resistance to the flow of current through the cell, as cyclic voltammograms for $\text{Ru}(\text{NH}_3)_6^{+2/+3}$, measured with and without the frit, were identically shaped.

Spectroelectrochemical Measurements in a Thin-Layer Cell. Cyclic voltammetric and chronoamperometric/absorption measurements were carried out in a homemade, thin-layer spectroelectrochemical cell. The cell design is shown in Figure 3-1. The main body of the cell was constructed with Kel-F plastic and optical-quality quartz. The entire body fits in a standard 10 x 10 mm quartz cuvette. A silicone rubber gasket, placed between the quartz insert and electrode surface, creates a thin-layer cavity 150 μm thick with a volume of 4.8 μL . Electrical contact with the electrode was made by pressing a Pt wire along one edge of the electrode surface not in contact with the electrolyte solution. Another coil of Pt wire was used as the auxiliary electrode, and Ag wire was used as a quasi-reference electrode (QRE). The thin-layer cavity is open at the

bottom, allowing it to be filled with electrolyte solution through capillary action when the quartz cuvette is partially filled with solution. The auxiliary and reference electrodes were positioned in the electrolyte solution (below the cell insert) in the assembled and filled cell.

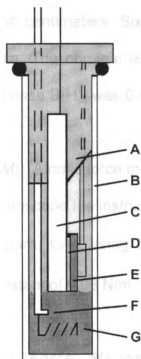


Figure 3-1. Diagram of the transmission thin-layer spectroelectrochemical cell: (A) Kel-F body, (B) quartz cuvette, (C) polished quartz, (D) 150- μm silicone gasket, (E) boron-doped diamond OTE, (F) Ag-QRE, and (G) Pt auxiliary electrode.

Four-Point Probe Resistivity Measurements. The resistivity of the diamond/quartz and ITO/quartz electrodes was measured with an in-line arrangement, tungsten-tip, four-point probe connected to an HP 3478A multimeter (HewlettPackard, Palo Alto, CA), which was operated in the four-wire

resistance measurement mode. The probe spacing was 0.1 cm. The measured resistance from i-V data was converted to resistivity according to the equation,⁶⁴

$$R_s (\Omega \cdot \text{cm}) = 4.532 \times t \times R(\Omega)$$

where t is the film thickness in centimeters. Six measurements were made at different locations on each film. The nominal resistivity of the diamond/quartz OTE, doped with 10 ppm gas phase B_2H_6 , was 0.026 $\Omega\text{-cm}$.

Atomic Force Microscopy (AFM). Atomic force micrographs were captured in the contact mode (in air) with a Nanoscope IIIa instrument (Digital Instruments/Veeco Metrology Group, Santa Barbara, CA), using 200 μm narrow-leg, triangular cantilevers having a spring constant of 0.06 N/m.

Conductivity-Probe Atomic Force Microscopy (CP-AFM). CP-AFM measurements made with a Digital Instruments NanoScope IIIa AFM (Veeco, Santa Barbara, CA), including a Digital Instruments Signal Access Module and a lab-built current-voltage amplifier. A Gold-coated silicon tip was used in the contact mode (NPG-20, Veeco, Santa Barbara, CA). Electrical contact was made between the diamond/quartz OTE and the metal sample holder by applying conductive carbon tape along two edges of the OTE. A bias voltage of -2.0 V was applied between the sample and the tip. The current-voltage amplifier was used to convert the current measured across the tip/electrode contact to a

voltage signal. The voltage signal was read by the NanoScope IIIa Signal Access Module and recorded at each point across the surface as the height mode image was captured. In this way, complementary height mode and conductivity images of the surface were captured.

Chemicals. KCl (1 M, Mallinckrodt ACS, or Baker ACS, 99.9%), 0.1 M NaOH (Mallinckrodt ACS, 99%), and 10 mM HClO₄ (Aldrich, 70% in water from 99.999%) were each prepared once a week with 18 MΩ-cm ultrapure water from a Barnstead E-pure water purification system. K₄Fe(CN)₆ (Aldrich ACS, 99%), Ru(NH₃)₆Cl₃ (Aldrich ACS, 98%) in 1 M KCl, and chlorpromazine hydrochloride (Sigma) in 10 mM HClO₄ were all prepared fresh daily.

Boron Nuclear-Reaction Measurements. The boron dopant concentration was determined by boron nuclear-reaction analysis (Surface Characterization Facility, Case Western Reserve University). Calibration was performed with a piece of high-quality boron-nitride, which is a stable and rich source of boron. The samples were irradiated with a 1 MeV proton beam and the resulting α spectrum was compared to that of a boron nitride standard. The reaction $^{11}\text{B}(p,\alpha)^8\text{Be}$ yields a high energy alpha particle (6 to 8 MeV) that can be detected by a silicon barrier back-scatter detector at energies well above those of the elastically scattered protons. The spectra gathered were integrated over a fixed energy range chosen so that the lowest energy was well above the energy for protons backscattered from the sample. The boron concentration was calculated by

taking the ratio of the number of alphas measured in the unknown and the standard material, corrected for the differing particle doses and density.

Hall Effect Measurements. The carrier concentration and mobility was determined by David Young (NREL) through a Hall measurement (Model HL5500, Bio-Rad Microscience, England) performed at room temperature under a magnetic field of 0.492 T. Electrodes were covered with photoresist material with only small areas of the four corners left exposed. Films were placed in a vacuum deposition chamber and titanium metal (600 Å thick) was evaporated onto the exposed corners of the diamond film. The photoresist material was then chemically removed from the films. The specific electrical measurements for the Hall effect followed the American Society for Testing and materials designation F 76 - 86 "Standard Test methods for measuring resistivity and Hall coefficient and determining Hall mobility in single-crystal semiconductors".

3.3 Results and Discussion

Diamond/Quartz Optical Properties. At least five factors influence diamond's optical transparency in the near-UV and visible regions of the electromagnetic spectrum: (i) the substitutional boron in the lattice, which increases the optical density with a broad absorbance continuum above 600 nm, (ii) scattering losses due to the polycrystalline morphology, (iii) structural defects (e.g., grain boundaries) containing sp²-bonded carbon and boron, (iv) chemical impurities, such as substitutional nitrogen, that result in absorption below 300 nm,^{22, 38} and

(v) reflectance losses.³⁹

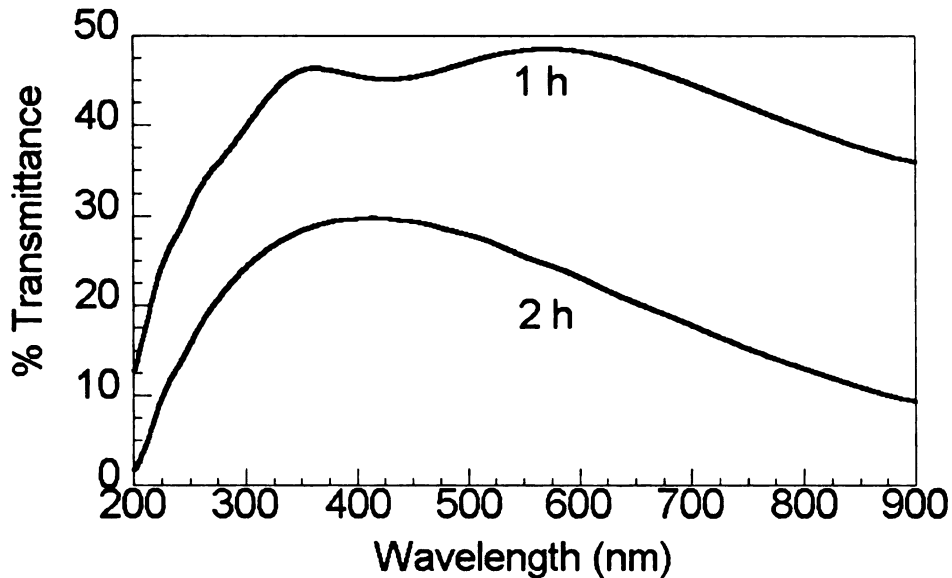


Figure 3-2. UV-visible transmission spectra measured in air for diamond/quartz OTEs deposited for 1 and 2 h. The films were deposited from a source gas mixture of 0.5% CH₄/H₂ and 10 ppm B₂H₆. Film thicknesses are ca. 500 nm and 1000 nm, estimated by SEM cross-section.

Background-corrected UV-Vis transmission spectra for two different diamond/quartz films are shown in Figure 3-2. The films were grown for 1 and 2 h, respectively, leading to films of different thicknesses. For both the 1- and 2-h films, the transmittance significantly decreases below 300 nm, because of (i) absorption by nitrogen impurities (i.e., electronic transition from nitrogen impurity levels to the conduction band)⁶⁵ and (ii) the indirect band gap absorption below 225 nm (i.e., electronic transition from the valence band to the conduction band).³⁹ Nitrogen is a common impurity in chemical vapor deposition (CVD) diamond arising from either contamination of the source gases or atmospheric

leakage into the reactor. The A aggregate of nitrogen, comprising a nearest-neighbor pair of substitutional nitrogen atoms, is the dominant impurity in most natural diamonds.²² This A aggregate behaves as a deep donor with an ionization energy of 4 eV and may be responsible for the absorption between 225 and 300 nm. The transmittance of the 1-h film is relatively constant at 40-50% between 300 and 800 nm. The transmission decreases at wavelengths longer than 600 nm due to absorption by the boron dopant band.⁶⁰ The adsorption of this band increases proportionately with doping level. The 2-h film is thicker and presents a longer path length, hence the reduced transparency.

Figure 3-3 shows plots for light transmitted, reflected, and absorbed by two diamond/quartz OTEs, deposited for 1 h with 10 ppm (top) and 1 ppm (bottom) B_2H_6 , measured by our collaborator at NREL, David Young. Reflectance (dashed line) for the film doped with 10 ppm B_2H_6 represents less than 10% of the transmission loss below 400 nm. Rather, this transmission loss is due to absorption of light by the material, nearly 90% at 200 nm (the material's band-gap cutoff). The amount of absorbed light decreases to ca. 45% at 400 nm. The loss due to absorption remains constant at about 45% from 400 to 1000 nm. Reflectance losses gradually increase to 20% at wavelengths between 600 and 1000 nm. The transmission spectrum shown in this figure is similar in shape to the spectra presented above in Figure 3-2, but without periodic variations in transmission with wavelength. As demonstrated by the reflectance spectra, the periodic variation in the transmission spectra is due to wavelength dependant

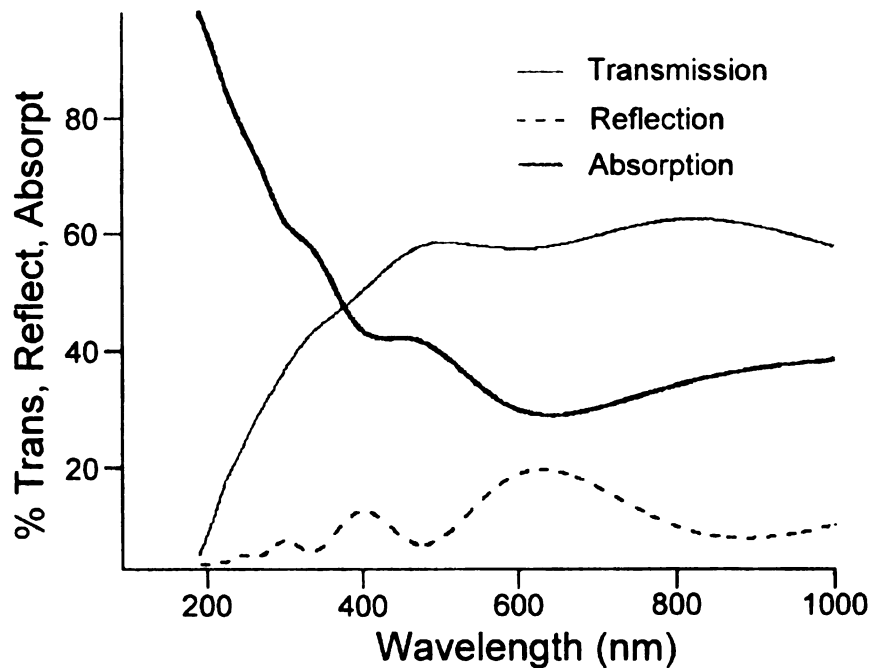
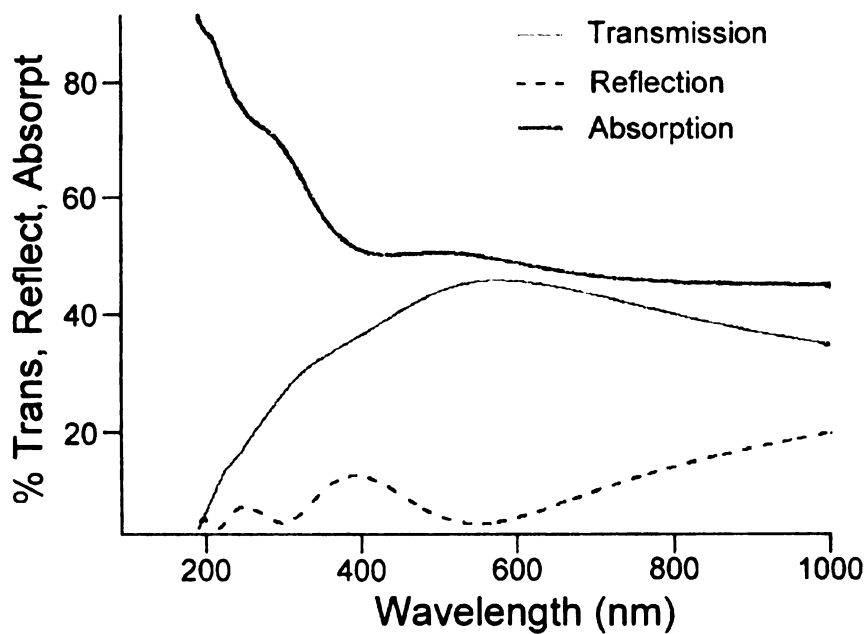


Figure 3-3. Plots of transmittance, reflectance, and absorbance of UV-Vis radiation measured for diamond/quartz OTEs deposited with 10 ppm (top) and 1 ppm (bottom) B₂H₆. Measurements courtesy of David Young (NREL).

variations in the film reflectance. Reflectance spectra have been shown to vary in this manner for thin-films of diamond deposited on glass substrates.⁵¹ The variation likely arises from constructive/destructive interference of the light reflected from both surfaces of the thin diamond film.³⁹

The transmission, reflectance, and absorption spectra for the diamond/quartz OTE deposited for 1 h with 1 ppm B₂H₆ in Figure 3-3 (bottom) have the same shapes but different magnitudes than the spectra for the the 10 ppm film. The light transmitted is greater, because the light absorbed by boron in this film in the 400-900 range is significantly less than for the 10 ppm film. The fringes in the reflectance spectra are slightly shifted for the 1 and 10 ppm films. This is explained by the difference in film thickness. The increased boron dopant concentration has been shown to change film morphology and increase the diamond growth rate.⁶⁶

In summary, the diamond/quartz OTE has optical transmission in the UV-Vis region that is limited to ca. 80% by reflection due to diamond's high refractive index. There is no transmission at wavelengths less than 225 nm, the wavelength corresponding to the diamond bandgap energy of 5.5 eV. Transmission is further decreased by the absorbance by nitrogen impurity modes at wavelengths less than 300 nm, and boron dopant and modes at wavelengths greater than 600 nm. The absorption due to boron dopant modes can be limited by decreasing the concentration of gas phase B₂H₆ (ca. 50% for 10 ppm B₂H₆

and ca. 30% for 1 ppm B_2H_6). The transmission varies inversely with film thickness, which is controlled by varying the deposition time. The periodic variation in transmission is likely due to wavelength-dependant reflection.

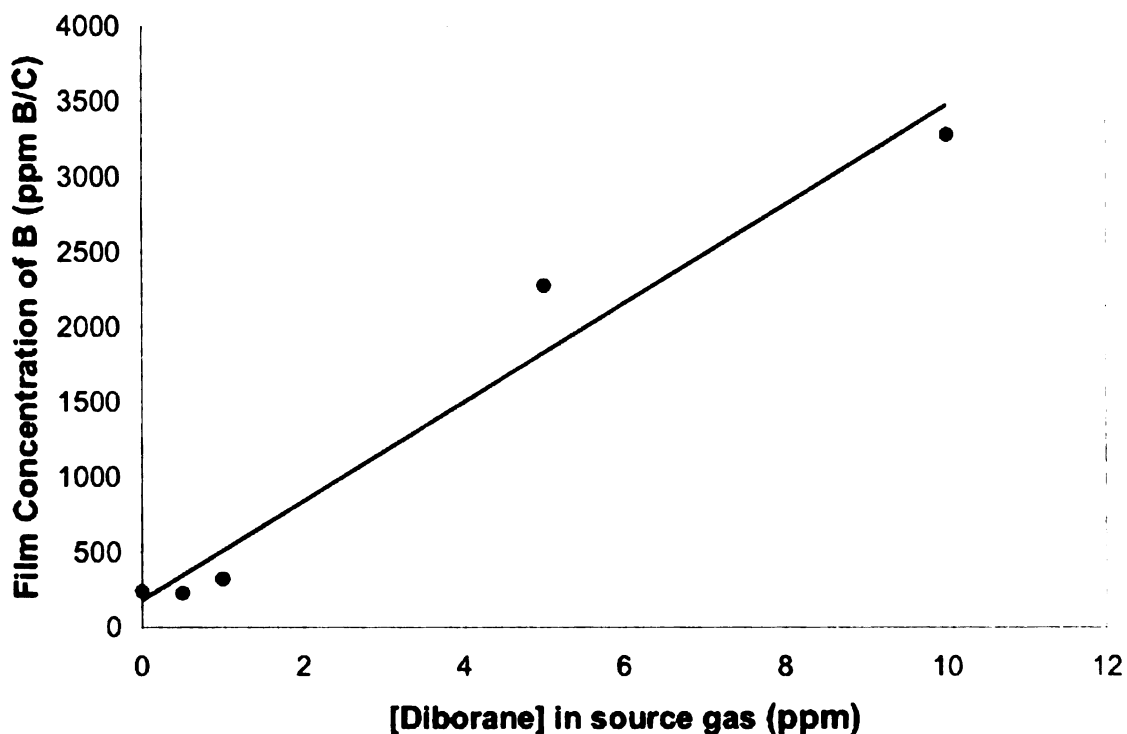


Figure 3-4. Plot of the boron concentration in diamond films deposited on p-Si, as determined by boron nuclear reaction analysis, versus the source gas B_2H_6 concentration used during deposition. Deposition time = 1 h. All other deposition conditions were kept constant.

Electronic Properties. The carrier concentration in diamond films can be varied by manipulating the gas phase B_2H_6 concentration in the source gas mixture during deposition. While no measurements of boron concentration in the diamond/quartz OTE have been made, data are available for films deposited on Si using similar deposition conditions (0.5% CH_4/H_2). Presented in Figure 3-4 is

the concentration of boron atoms in diamond films deposited on Si, plotted against the concentration of diborane gas in the source gas mixture (0, 0.1, 0.5, 1, 5 and 10 ppm). These boron concentration measurements were made by our colleagues at Case Western Reserve University. While the B₂H₆ concentration was varied, the other deposition conditions were kept constant. Clearly demonstrated in this plot is the linear dependence of the boron concentration in the film with the diborane concentration in the source gas. This relationship is expected to extend to the present boron-doped diamond films deposited on quartz.

The conductivity of the diamond film on quartz varies with the boron concentration. The film conductivity and carrier concentration of the diamond/quartz OTE deposited with 10 ppm B₂H₆ in the source gas are greater than the values for the OTE deposited with 1 ppm B₂H₆. The resistivity of the 10 ppm electrode was 0.026 Ω-cm, as measured by 4-point probe, and 0.058 Ω-cm as determined from a Hall effect measurement (Table 1). These measurements revealed a carrier concentration of ca. 10²⁰ cm⁻³. The 1 ppm, 1 h film, possessed significantly higher optical throughput, but had five times fewer carriers and larger electrical resistivity (0.17 Ω-cm) than did the film grown with 10 ppm B₂H₆. This resistivity proved too large to support reasonably fast electrochemical reactions. Consequently, the 10 ppm OTE was characterized in more detail and used in the spectroelectrochemical measurements discussed below. The resistivity of the film grown with 10 ppm gas phase B₂H₆ is of the same order of magnitude as

boron-doped microcrystalline films grown under the same conditions on Si (0.5 % CH₄/H₂ and 10 ppm gas phase B₂H₆), <0.01 Ω-cm.⁴¹ The dopant concentration is similar in both films, so the carrier concentration is expected to be similar (Hall effect measurements of polycrystalline films deposited on Si are currently underway). The lower conductivity for the diamond/quartz OTE can be explained by a lower carrier mobility. The carrier mobility in the diamond/quartz OTE grown with 10 ppm gas phase B₂H₆ (0.311 cm²/V-s) is lower than values reported in the literature for polycrystalline boron-doped diamond films (1-50 cm²/V-s).⁶⁷ The lower mobility is caused by a high density of grain boundaries due to the smaller crystallite size (100-200 nm), as compared with microcrystalline films.⁶⁸ The dramatic effect of grain boundary scattering on carrier mobility was shown by the comparison of the room temperature carrier mobilities for homoepitaxial and polycrystalline diamond films grown under the same conditions with the same boron dopant concentration and carrier concentration (2 x 10⁸ cm⁻³).⁶⁹ The

Table 3-1. Carrier concentration and mobility (measured by Hall effect method) and sheet resistivity (measured by four point probe method) data for diamond/quartz OTEs deposited for 1 hour using 1 and 10 ppm B₂H₆.

Source Gas B₂H₆ Concentration (ppm)	Carrier Concentration (cm⁻³)	Carrier Mobility (cm²/V-s)	Resistivity, Hall (Ω-cm)	Resistivity, 4-point probe (Ω-cm)
1	6.4x10 ¹⁹	0.572	0.17	N/A
10	3.5x10 ²⁰	0.311	0.058	0.026

mobility in the homoepitaxial film (no grain boundaries) was $520 \text{ cm}^2/\text{V-s}$ and the mobility in the polycrystalline film (high density of grain boundaries) was only $33 \text{ cm}^2/\text{V-s}$.

In summary, the diamond/quartz OTE has a conductivity that varies with the gas phase B_2H_6 concentration ($0.17 \text{ } \Omega\text{-cm}$ for 1 ppm B_2H_6 , $0.06 \text{ } \Omega\text{-cm}$ for 10 ppm B_2H_6). The carrier concentration in the diamond/quartz OTE grown for 1 h with 10 ppm gas phase B_2H_6 was similar to that for polycrystalline boron-doped diamond thin-films (ca. 10^{20} cm^{-3}) grown on Si, but the resistivity was slightly greater (factor of 5-7). This increased resistivity is attributed to the lower carrier mobility in the diamond/quartz OTE ($0.311 \text{ cm}^2/\text{V-s}$ versus $1\text{-}50 \text{ cm}^2/\text{V-s}$), which is caused by the higher density of grain boundaries.

Electrochemical Properties. A background cyclic voltammetric i-E curve in 1 M KCl for a diamond/quartz OTE deposited for 1 h with 10 ppm B_2H_6 is shown in Figure 3-5. This measurement, and those discussed below, was made in a standard, single compartment electrochemical cell. The response is featureless over the entire potential range, but the current magnitude is slightly larger than that normally observed for boron-doped diamond thin-film deposited on Si. The anodic current density at 0.1 V is $7 \text{ } \mu\text{A}/\text{cm}^2$, compared to $2 \text{ } \mu\text{A}/\text{cm}^2$ for a diamond film on Si.^{52, 62} The larger background current could be due to (i) a higher density of reactive grain boundaries due to the small crystallite size, and/or (ii) a higher

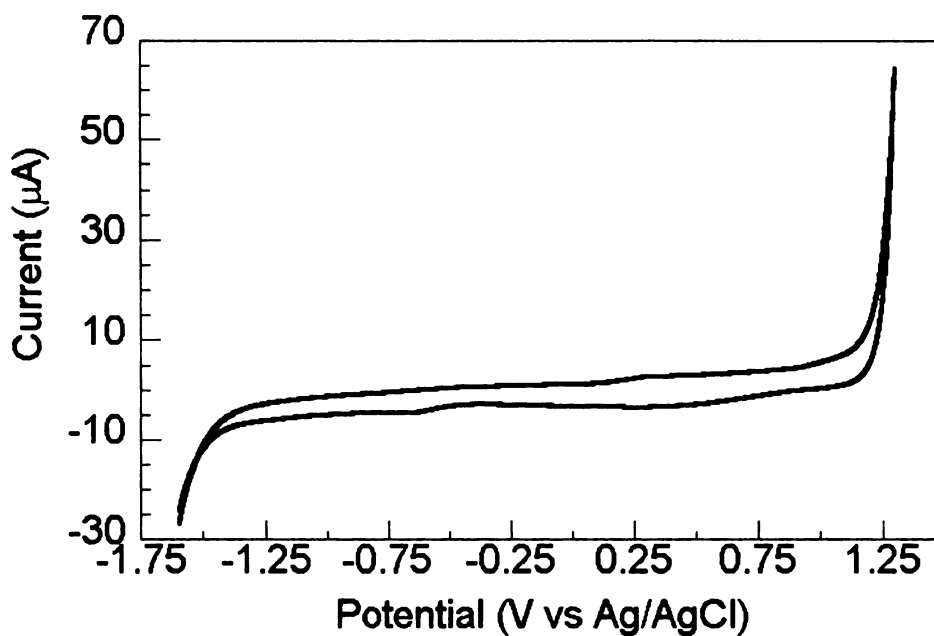


Figure 3-5. Cyclic voltammetric i-E curve in 1 M KCl for a diamond/quartz OTE deposited for 1 h with 10 ppm B₂H₆. Scan rate = 25 mV/s.

density of conductive diamond areas. The grain boundaries likely contain some sp²-bonded carbon which exhibits a larger capacitance than diamond.⁷⁰ Because the diamond/quartz OTE has smaller crystallites than does a typical microcrystalline diamond film deposited on Si, the density of grain boundaries in the diamond/quartz OTE is higher. To determine the fraction of conductive regions on the diamond/quartz OTE, the surface was mapped using CP-AFM. By comparing topographical and conductive images of the same electrode area, Wang et al.⁷¹ and Holt et al.³⁷ showed that the polycrystalline diamond surface is made up of conductive and non-conductive areas, with the conductive areas corresponding to clusters of grains and grain boundaries. With increased boron

dopant concentration, the fraction of the surface that is conducting increased. Presented in Figure 3-6 is a topographical image (A) and a conductivity image (B) of the diamond/quartz OTE deposited for 1 h with a concentration of 10 ppm gas phase B_2H_6 . The light color in Figure 3-6B represents areas of high conductivity, and the dark color represents areas of low conductivity. The vertical scale of Figure 3-6B can be converted to a current scale by multiplying the voltage values (0 to 10 V) by the gain value of the current-voltage amplifier ($3.3 \mu A/V$), giving a range of 0 to $33 \mu A$. Given the bias voltage of 2 V applied between the tip and the electrode surface, the light areas correspond to a resistance of up to ca. $60 k\Omega$. Line scans across the current image show that the dark areas correspond to the zero current line, or an infinite resistance. This implies that the light areas represent conductive particles surrounded by insulating material. When Figure 3-6B is compared to the topographical image in Figure 3-6A, it is clear that most conductive areas in the film do not correspond to large diamond features. Rather, the most conductive areas are clusters of smaller features and the boundaries between the larger features. A rough estimate of conductive area based on the conductivity image is ca. 50%. This is higher than the conductive area previously reported for polycrystalline diamond films grown with 10 ppm gas phase B_2H_6 .³⁷ The larger conductive area may be explained by the smaller features of this film. The conductive areas are predominantly the smaller features and grain boundaries between features, and with the smaller feature size in the diamond/quartz OTE, the film contains a higher density of grain boundaries. It is reasonable that the diamond/quartz OTE

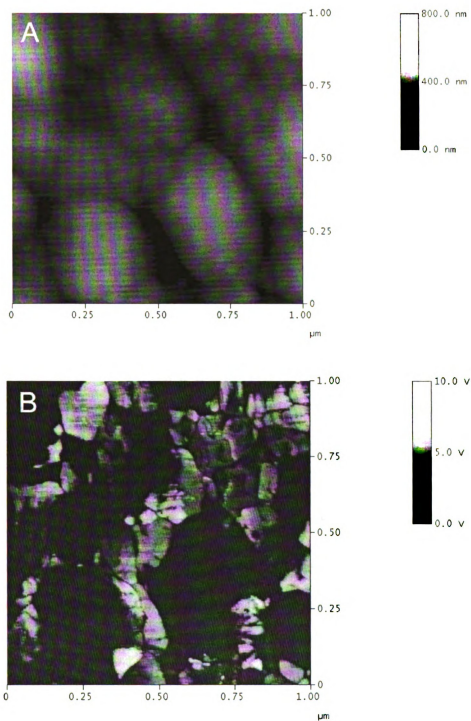


Figure 3-6. Height-mode (A) and conductivity-probe (B) atomic force micrographs for a diamond/quartz OTE deposited for 1 h with 10 ppm gas phase B_2H_6 .

has larger background current because of both the higher density of active grain boundaries and the larger electronically-active surface area.

In Figure 3-5, the anodic current at 1.25 V is due to the onset of chlorine evolution and the cathodic current at -1.6 V is attributed to hydrogen evolution. The shape was unchanged with repeated cycling, a characteristic that is typical for diamond films void of appreciable quantities of electroactive, sp²-bonded carbon impurity at the surface.⁵²

Table 3-2. Summary of the cyclic voltammetric data for a diamond/quartz OTE deposited for 1 h using 10 ppm B₂H₆.

Redox system	ΔE_p (mV)	$E_{p/2}$ (mV vs Ag/AgCl)	i_p^{ox} (mA)	i_p^{ox}/i_p^{red}	Q_p^{ox}/Q_p^{red}
Ru(NH ₃) ₆ ^{+2/+3}	59	-165	5.0	0.99	1.1
Fe(CN) ₆ ^{-3/-4}	67	276	6.3	1.1	1.0
CPZ	84	652	5.6	1.5	1.5

Cyclic voltammetry was used to investigate the electrochemical properties of the diamond/quartz OTE deposited for 1 h using 10 ppm B₂H₆. The following redox systems were employed: 0.1 mM Ru(NH₃)₆^{+2/+3} + 1 M KCl, 0.1 mM Fe(CN)₆^{-3/-4} + 1 M KCl, and 0.1 mM chlorpromazine (CPZ) + 10 mM HClO₄. A summary of the data is presented in Table 3-2. The cyclic voltammetric ΔE_p for Ru(NH₃)₆^{+2/+3} is relatively insensitive to the surface microstructure and chemistry of diamond, and other electrodes, such as glassy carbon, but is relatively

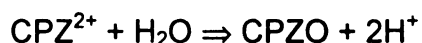
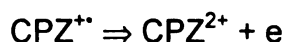
sensitive to the electronic properties (i.e., density of states) near the standard reduction potential for the redox couple.^{62, 72, 73} Therefore, this redox system is useful for probing the diamond film's electronic properties. ΔE_p is 59 mV at this scan rate (100 mV/s), indicating the electrode has a high density of electronic states at these potentials, sufficient to support rapid electrode-reaction kinetics. As expected for currents limited by semi-infinite linear diffusion, i_p^{ox} varies linearly ($r^2 > 0.99$) with the scan rate^{1/2}. The i_p^{ox}/i_p^{red} and Q_p^{ox}/Q_p^{red} ratios are near 1.0 for scan rates between 10 and 500 mV/s. The slope of the line of best fit for the i_p^{ox} plotted versus the scan rate^{1/2} is $7 \mu A/(V/sec)^{1/2}$. The theoretical value for this slope at room temperature for a reaction involving one electron, an electrode area of 0.2 cm^2 , a diffusion coefficient of $7.8 \times 10^{-6} \text{ cm}^2/\text{sec}$,⁷⁴ and a solution concentration of 0.1 mM is $14 \mu A/(V/sec)^{1/2}$. This discrepancy in slopes can be explained by the roughly 50% of actual active electrode area out of the 0.2 cm^2 nominal area demonstrated by the CP-AFM measurements discussed above.

ΔE_p for $\text{Fe}(\text{CN})_6^{-3/4}$ is relatively insensitive to the surface microstructure of diamond but is very sensitive to the electronic properties and surface chemistry.^{52, 62} ΔE_p is very sensitive to the surface microstructure, chemistry, and electronic properties of glassy carbon, as well.^{72, 73} For example, ΔE_p is much larger at diamond electrodes terminated with oxygen functional groups than at electrodes terminated with hydrogen.⁵² The oxygen functional groups apparently block reaction a site for this surface-sensitive redox system that is available on the hydrogen-terminated surface; hence, the reaction kinetics are more inhibited.

Therefore, this redox system is useful for probing both the electronic properties and the extent of hydrogen surface termination. ΔE_p for this redox couple is 67 mV at this scan rate (100 mV/s), indicating the electrode has a high density of electronic states at these potentials and the surface is predominately hydrogen-terminated. The voltammetric responses for these two redox systems were unchanged, even after the numerous electrochemical measurements. The i_p^{ox} for this analyte varies linearly ($r^2 > 0.99$) with the scan rate^{1/2}, indicating that the current is limited by semi-infinite linear diffusion of the reactant to the interfacial reaction zone. The i_p^{ox}/i_p^{red} and Q_p^{ox}/Q_p^{red} ratios are stable and near 1.0 for scan rates between 10 and 500 mV/s.

The cyclic voltammetric ΔE_p for CPZ is relatively insensitive to the surface chemistry and microstructure of diamond but is relatively sensitive to the electronic properties.^{62, 75} CPZ has also been shown to undergo rapid electron transfer at polished glassy carbon (sp²-bonded carbon), behaving as an outer-sphere system with respect to electron transfer.⁷⁶ CPZ shows a tendency to adsorb on glassy carbon, but inhibiting adsorption by surface modification has little effect on the electrode kinetics.⁷⁶ No significant adsorption, however, has been found for hydrogen-terminated, boron-doped diamond.^{62, 75, 77} ΔE_p for CPZ is relatively insensitive to the surface chemistry at both diamond and glassy carbon.^{62, 75, 76} However, i_p^{ox} varies linearly with scan rate at glassy carbon, as expected for an adsorbed species, and it varies linearly with (scan rate)^{1/2} at diamond, as expected for a species diffusing to the interfacial reaction zone.

CPZ undergoes two one-electron oxidation reactions in acidic media, according to the following reaction sequence.⁷⁸



The first one-electron oxidation reaction to form $\text{CPZ}^{+\bullet}$ is reversible, but the second one-electron reaction to form CPZ^{2+} is chemically irreversible, because the dication product undergoes rapid reaction with water to form an electroinactive sulfone.^{78, 79} The voltammetric results reported herein are for the first one-electron redox reaction only. The cyclic voltammetric *i*-*E* curve for 0.1 mM CPZ + 10 mM HClO_4 is similar in shape to curves previously reported for diamond electrodes.^{62 75-77, 80} The ΔE_p is 84 mV at 100 mV/s. The i_p^{ox} value varies linearly with the scan rate^{1/2} between 20 and 500 mV/s. These results indicate that the diamond electrode surface is predominately composed of sp^3 -bonded diamond with low levels, if any, of sp^2 -bonded amorphous carbon impurity, although this conclusion was not confirmed by acid washing and rehydrogenating the diamond/quartz OTE. The $i_p^{\text{ox}}/i_p^{\text{red}}$ and $Q_p^{\text{ox}}/Q_p^{\text{red}}$ ratios are greater than 1. This is attributed to the fact that some production of CPZ^{2+} occurs during the positive sweep due to the closeness of the potentials for these two reactions. The current response during the positive sweep of the background corrected *i*-*E* curve in Figure 3-7 does not return to 0 A at the end of

the sweep because the wave for the next oxidation step is beginning at that potential. The produced CPZ²⁺ quickly undergoes hydrolysis and is unavailable for reduction during the reverse sweep.

Normally, for conductive diamond films deposited on electrically conducting substrates, the current is passed through the diamond film and the conductive substrate to a metal current collector in backside contact with the substrate. In the case of the diamond/quartz OTE, such a current path is not possible. Therefore, the charge transport occurs laterally through the electrode to a metal current collector positioned near the edge of the film. This means that both through-grain and through-grain-boundary paths are possible. The low ΔE_p values suggest that the grains are in good electronic communication with the grain boundaries, providing a low-resistance current pathway.

Figure 3-7 presents a background-corrected cyclic voltammetric i-E curve for 0.1 mM CPZ + 10 mM HClO₄, measured in the thin-layer spectroelectrochemical cell. The scan rate was 2 mV/s. The Q_p^{ox}/Q_p^{red} ratio is ca. 1, and the peaks are approximately Gaussian in shape with no evidence of diffusional tailing. i_p^{ox} and i_p^{red} varied linearly with the scan rate, while Q_p^{ox} and Q_p^{red} were independent of the scan rate. These trends are predicted for thin-layer voltammetric behavior.^{63, 81, 82} ΔE_p is 68 mV and is larger than the 0 mV expected if the electrode kinetics are fast relative to the scan rate. We suppose the larger-than-expected ΔE_p is due, at least in part, to some uncompensated

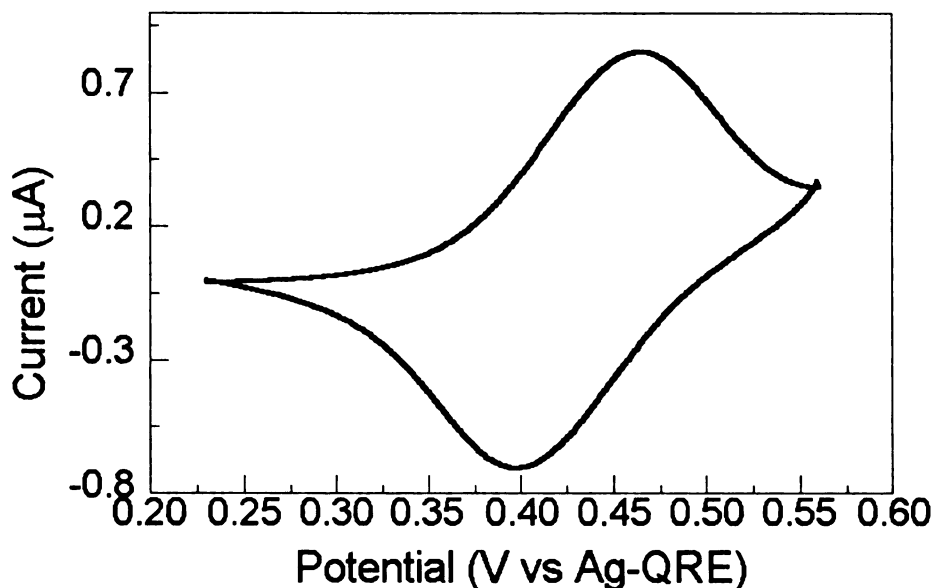


Figure 3-7. Background-corrected, thin-layer voltammetric i-E curve for a diamond/quartz OTE, deposited for 1 h using 10 ppm B₂H₆, in 0.1mM CPZ in 10 mM H₂SO₄. Scan rate = 2 mV/s.

ohmic resistance in the cell. The Q_p^{ox} value of 56 μC is consistent with the charge calculated for 4.8 μL of 0.1 mM CPZ ($n = 1$), 46 μC . The peak current for a cyclic voltammetric i-E curve under thin –layer conditions is predicted to be^{63, 81,}

82

$$i_p = 9.39 \times 10^5 n^2 \nu V C^*$$

where n is the number of electrons transferred per equivalent, ν is the scan rate (V/s), V is the cell volume (cm^3), and C^* is the bulk concentration (mol/cm^3). The

i_p^{ox} value for the curve in Figure 3-7 of $0.86 \mu\text{A}$ is in good agreement with the predicted value of $0.90 \mu\text{A}$.

In summary, the diamond/quartz OTE possesses a background capacitance larger than that for a polycrystalline boron-doped diamond film on Si grown with 10 ppm gas phase B_2H_6 . The smaller feature size of the diamond/quartz OTE leads to a higher density of active grain boundaries and a higher proportion of conductive area. The background cyclic voltammetric i-E curve is stable, with a potential window in 1 M KCl of nearly 3 V. The diamond/quartz OTE possess electrochemical responsiveness to several redox systems similar to that of polycrystalline boron-doped diamond films on Si grown with 10 ppm gas phase B_2H_6 . The peak currents for these redox systems were ca. 50% of the currents predicted by theory for the nominal electrode area, agreeing with the CP-AFM measurement of the ca. 50% conductive electrode area. The relatively rapid redox kinetics of these systems at the diamond/quartz OTE indicate that it is sufficiently conducting, has a hydrogen terminated surface chemistry, and is predominately comprised of sp^3 -bonded diamond.

Spectroelectrochemical Measurements. UV-Vis spectroelectrochemical measurements for the first one-electron transfer reaction of chlorpromazine, $\text{CPZ}^{0/+}$, were performed and the absolute spectra recorded during anodic (0.5 V) and cathodic (0.30 V) potential steps are presented in Figure 3-8A. The spectral changes for CPZ are recorded on a sloping background, as the diamond OTE

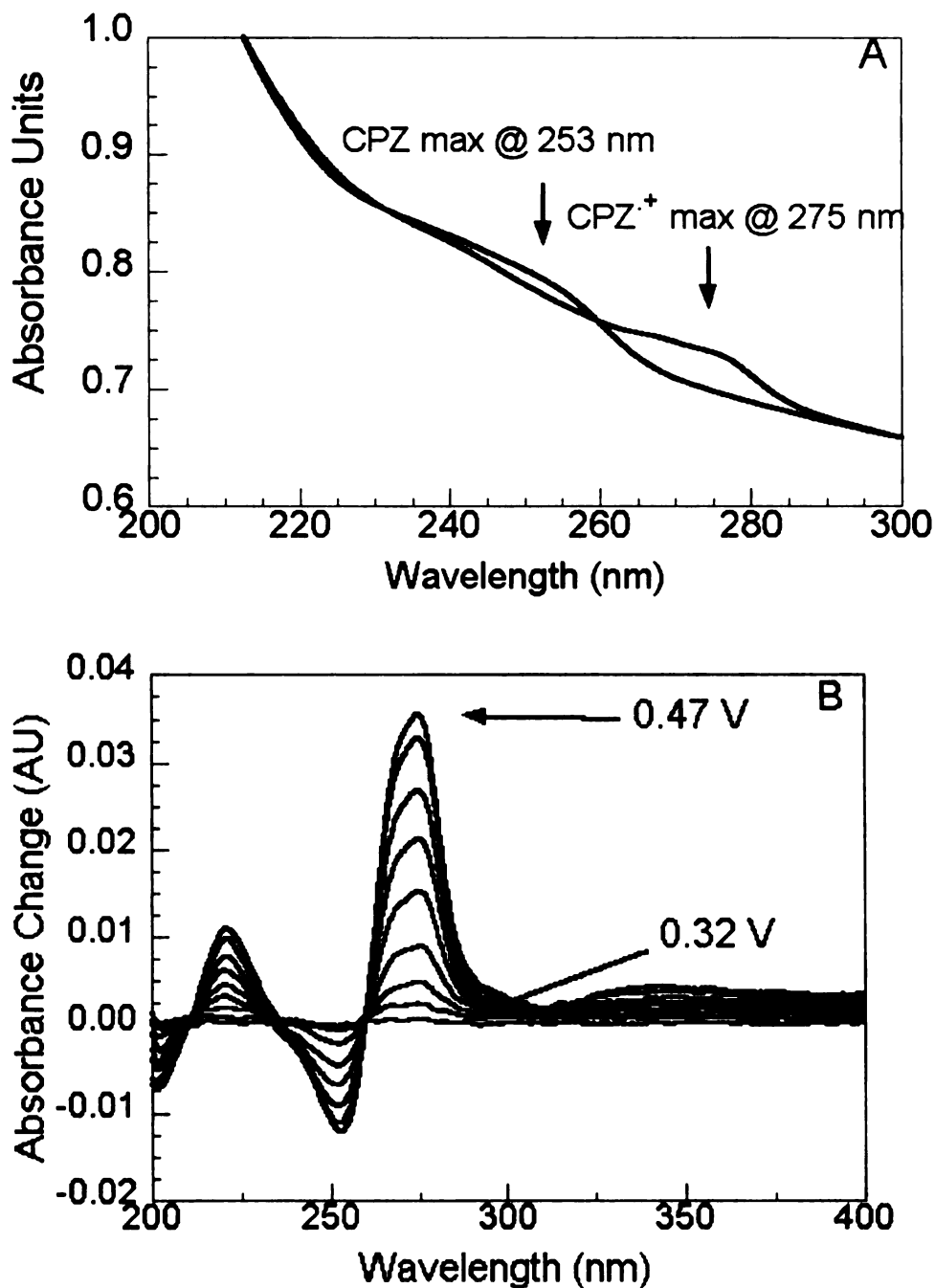


Figure 3-8. (A) UV-visible absorbance spectra at a diamond/quartz OTE, deposited for 1 h using 10 ppm B₂H₆, for chlorpromazine (CPZ⁰), at 0.30 V, and the oxidation product (CPZ^{•+}), at 0.50 V, in the thin-layer cell. (B) A series of UV-visible absorbance spectra, using the same film, for 0.1 mM chlorpromazine in 10 mM HClO₄, as the potential is stepped from 0.32 to 0.47 V vs Ag-QRE.

exhibits a changing transmittance at these wavelengths (see Figure 2). CPZ has an absorbance maximum at 253 nm due to a $\pi \rightarrow \pi^*$ transition ($\alpha = 10\,000$ L/mol-cm), while the radical cation produced by a one-electron oxidation has an absorbance maximum at 275 nm.⁷⁹ This is presumably also due to a $\pi \rightarrow \pi^*$ transition ($\alpha = 20\,000$ L/mol-cm).

In Figure 3-8B, a series of difference spectra (oxidized form - reduced form) are presented for different applied potentials going from less positive to more positive values. Each potential step was applied until measured spectral features were stable with scanning (ca. 1 min). As the potential stepped positively from 0.32 to 0.47 V, the peak at 253 nm gradually decreases and the peak at 275 nm increases. A peak at 224 nm also develops as the applied potential is made more positive. The spectral features can be reversibly formed with changes in the applied potential. A background spectrum for the cell containing fully reduced CPZ was subtracted from each of the spectra to present the absorbance changes relative to a flat baseline. When overlaid, the spectra show well-defined isosbestic points. The isosbestic point near 260 nm indicates that the species responsible for the absorbance peaks on either side of the point are stoichiometrically related. Here, these peaks are due to CPZ and CPZ^{•+}.

A calibration curve was constructed from the absorbance change at 275 nm as a function of solution concentration. The plot was linear between 20 μ M and 1 mM, with a linear regression correlation coefficient of 0.9996 and a near-zero

(0.0095 AU) ordinate intercept. The absorbance change was measured during a potential step from 0.30 to 0.50 V. This linear response curve indicates that the diamond OTE provides an analytically useful signal for the detection of CPZ. A 0.5 μM limit of detection ($S/N = 3$) is estimated from the data. A Nernst plot of applied potential versus $\ln [O]/[R]$, calculated from absorbance changes at 253 nm, was also constructed. The plot was linear, as predicted, with a linear regression correlation coefficient of 0.9990, and has an intercept of 0.41 V, close to the $E_{p/2}$ of 0.43 V, determined from the thin-layer cyclic voltammetric i-E curve presented in Figure 3-5. The slope of this plot was 56.9 mV, and is close to the 59.2/n mV ($n = 1$) predicted by the Nernst equation. The slope also indicates that the oxidation of CPZ to CPZ^{•+} involves the loss of 1 electron.

3.4 Conclusion

Diamond/quartz OTEs have optical and electrochemical properties that can be adjusted for specific applications through manipulation of the deposition conditions. The boron doping level was adjusted so as to maximize the electrical conductivity and optical transparency. The deposition conditions were adjusted to limit losses due to absorption by limiting the film thickness and dopant concentration, and the losses due to scattering by growing a relatively smooth diamond film (roughness = 13 nm rms). A boron concentration of 10 ppm B_2H_6 source gas was selected for doping the film to produce sufficient conductivity. The diamond/quartz OTE has a high carrier concentration, 10^{20} cm^{-3} (holes), and a low electrical resistivity ($0.058 \Omega \cdot \text{cm}$) laterally through the grains and grain

boundaries.

The electrode utilized in the spectroelectrochemical measurements presented here exhibited a useful optical window in the UV-visible region from ca. 225 to 900 nm. The percent transmission was between 10 and 45% between 225 and 400 nm, and relatively constant near 50% from 400 to 900 nm. The periodic variation in transmittance was found to be due to reflection losses within the film. The electrochemical properties were demonstrated to be similar to those reported for other high quality boron-doped diamond thin-film electrodes. This includes a wide potential window of nearly 3 V in aqueous solution, a low and stable background current, and good electrochemical responsiveness for $\text{Fe}(\text{CN})_6^{-3/4}$, $\text{Ru}(\text{NH}_3)_6^{+2/+3}$, and $\text{CPZ}^{0/+}$. CP-AFM measurements indicated that the fraction of conductive area (electrochemically active area) is ca. 50% of the nominal area. Consistent with this was the i_p^{ox} variation with v in cyclic voltammetric i - E curves for $\text{Fe}(\text{CN})_6^{-3/4}$. The slope of the experimental curve was half as steep as the theoretical value suggesting that only half of the experimental area was electrochemically active. The film resistivities are a factor of 5-7 larger than the typical boron-doped polycrystalline films deposited on Si under similar conditions. This is believed to be due to the low carrier mobility (grain boundary scattering) in the diamond/quartz film. Even so, the resistivity is low enough to allow for relatively rapid electron transfer reaction kinetics for several redox systems (i.e., minimal ohmic effects). The electrochemical redox probes further demonstrate that the diamond/quartz OTE consists of mostly

hydrogen-terminated sp^3 -bonded carbon, with no measurable contribution to the electrochemical signal by adventitious sp^2 -bonded carbon impurity.

The optimized diamond/quartz OTE was used for reproducible transmission spectroelectrochemical measurements. The spectroelectrochemical performance of the diamond OTE was evaluated in a specially designed, thin-layer cell, using chlorpromazine as a test analyte. Well-defined, thin-layer voltammetry was observed with Q_p^{ox} values independent of scan rate, as expected for thin-layer behavior. For the CPZ measurements, the linear dynamic range was from 20 to 100 μM and the estimated limit of detection was 0.5 μM (S/N = 3). A linear Nernst plot of the absorbance data observed with a slope of 56.9 mV, reflective of 1 electron being transferred per equivalent during the oxidation of CPZ and CPZ^{+} and an ordinate intercept of 0.41 V, a value representative of the formal potential for the redox system, E° .

4 The Optical, Electrical, and Electrochemical Property

Stability of the Boron-Doped Diamond/Quartz OTE

4.1 Introduction

In Chapter 3, it was shown that diamond thin-film coated on quartz possesses (i) an optical window in the UV-Vis region of the electromagnetic spectrum that extends from the diamond band-gap absorption edge (225 nm) out to ca. 900 nm, (ii) a working potential window of nearly 3 V in aqueous media, (iii) a low and stable background current, and (iv) relatively rapid electrode kinetics for several redox systems without pretreatment. The usefulness of this new OTE for the transmission spectroelectrochemical measurement of $\text{Fe}(\text{CN})_6^{-3/4}$, methyl viologen, ferrocene, chlorpromazine, and cytochrome c has been demonstrated.^{44, 46, 83, 84} However, in order for the diamond/quartz OTE to be practical for widespread application, it must also possess superb optical and electrochemical property stability during anodic and cathodic polarization and in a wide variety of chemical environments. In this Chapter, the stability of the optical, electrical, and electrochemical properties of the diamond/quartz OTE is compared with that of the most often used OTE, tin-doped indium oxide (ITO), during exposure to strongly acidic and alkaline solutions, organic solvents, and anodic and cathodic polarization.

ITO is a commonly used OTE for spectroelectrochemical measurements,¹³ as well as an optical material for optoelectronic devices including liquid crystal

displays and organic LEDs,⁸⁵ energy-efficient windows,⁸⁶ and aircraft window coatings. ITO, chemically vapor deposited onto quartz, is a highly transparent optical material in the near-UV and visible regions of the electromagnetic spectrum. In particular, greater than 70% transmittance is typical at wavelengths longer than the band-gap absorption edge at 275 nm. Indium oxide is a semiconductor. However, substitutional insertion of Sn⁴⁺ for In³⁺ imparts electrical conductivity to the material (typical resistivity = 10⁻⁵ Ω-cm). The Sn⁴⁺ dopant is an acceptor, meaning that holes are the primary charge carrier.⁸⁷ The optical and electrical properties of tin oxide,⁸⁸⁻⁹⁰ Sb-doped tin oxide^{91, 92} and Sn-doped indium oxide⁹² films during exposure to various chemical and electrochemical environments have been reported on, at least to some extent. While this material possesses excellent electrical conductivity, ITO is notoriously plagued by variable optical and electrochemical properties due to variations in the bulk and surface chemical composition from source-to-source.⁹² Additionally, due to chemical stability issues, the material has limited usage in strongly acidic solutions, in some chlorinated organic solvents (e.g., dichloromethane), and during cathodic polarization.

The research sought to answer the question of how the diamond/quartz OTE compares to a commonly used OTE material such as ITO. A comprehensive optical and electrochemical property study of the diamond/quartz and ITO/quartz OTEs is presented herein. The optical transmission, electrical resistivity, surface morphology, and electrode activity were investigated before

and after exposure to strongly acidic and alkaline aqueous solutions, organic solvents, and anodic and cathodic polarization in acidic and alkaline media.

4.2 Experimental

The Deposition of Diamond Thin-Film on Quartz. Boron-doped diamond electrodes were deposited on quartz as described in detail in Chapter 2. Briefly, the quartz was prepared for diamond growth by, first, manually polishing the surface with a 0.1 μm diamond powder. The polishing debris and excess diamond polishing powder were then removed by extensive sonication and solvent rinsing. A high density of scratches leads to a high initial nucleation density and a small nominal grain size. A source gas mixture of 0.5% CH_4 , diluted in H_2 , was employed for the deposition. The source gas mixture also contained 10 ppm B_2H_6 for boron doping. Growth was carried out at a system pressure of 45 torr, a microwave power of 600 W, and a growth temperature of ca. 800°C. The last step in the deposition process was a short, postgrowth anneal in a H_2 plasma (45 torr, 600 W) to remove any adventitious nondiamond sp^2 carbon impurity and to fully hydrogen terminate the surface. The resulting films were ca. 500 nm thick (1-h growth). The electrical resistivity of these films was 0.06 $\Omega\text{-cm}$, or less.

ITO Electrodes. Commercial ITO films with a nominal resistivity of ca. 3.3×10^{-5} $\Omega\text{-cm}$, as measured with a four-point probe, were vapor-deposited on a fused

quartz microscope slide (Delta Technologies, Ltd, Stillwater, MN). Individual ITO/quartz samples were cut into 1 cm² pieces by scoring along the uncoated surface and breaking. Films from three different batches were used in the research. The film thickness reported by the manufacturer of 20 nm was used for the resistivity calculations.

Solution Exposure Tests. The diamond/quartz and ITO/quartz OTEs were soaked for 48 h at room temperature in neat toluene (MCB Manufacturing Chemists, Inc., ACS), hexane (Baker, ACS, 97%), methanol (Baker, ACS, 99.8%), dichloromethane (Mallinckrodt, ACS), 1 M HNO₃ (Cleveland Chemical Industries, 70% ACS), and 1 M NaOH (Spectrum, ACS) to test the electrical and optical property stability. The aqueous solutions were prepared with ultrapure water. The transmission spectrum in the UV-Vis region and in-plane resistivity (both as described in Chapter 3) were recorded before and after solution exposure to probe for changes.

UV-Vis Transmission Measurements. A film was rinsed with ultrapure water and distilled 2-propanol, and dried under a stream of N₂ before recording a transmission spectrum. A plastic mask/holder, shaped to fit into the Shimadzu UV2401-PC UV-Vis spectrophotometer, was used to mount the samples in the optical path, with the light incident on the coated side of the sample. The film was placed over the hole in this mask and secured in place with double-sided adhesive tape on the uncoated side of the substrate. Transmission spectra were

collected before and after the solution exposure tests and the electrochemical polarizations. The latter are described below. The films remained attached to the mask during the electrochemical measurements to ensure that the spectra were collected for the same region exposed to the solution. This was accomplished by using the mask and a glassware ball-joint clamp to press the electrodes against an o-ring at the bottom of the glass cell. All transmission spectra were recorded against air in the reference beam path.

Electrochemical Polarization Tests. The optical, electrical and electrochemical property stability of the diamond/quartz and ITO/quartz OTEs were evaluated after anodic and cathodic polarization in both acidic and alkaline media. The diamond/quartz OTE was polarized by sweeping the potential between the oxygen and hydrogen evolution regions at a rate of 25 mV/sec over a 2.5 h period in each medium (>28 cycles). The potential limits used were -1.5 and +2.0 V in acid, -2.0 and +2.0 V in base (Ag/AgCl reference electrode). The current at the potential limits exceeded ± 1 mA (± 5 mA/cm²). The ITO/quartz OTE was polarized by sweeping the potential between the oxygen and hydrogen evolution regions at a rate of 25 mV/sec until electrical communication was lost. The potential limits used were -1.0 and +2.5 in acid and -1.6 and +1.75 in base.

Electrochemical Measurements. Electrochemical measurements were made using a computer-controlled potentiostat (Model 1200, Cypress Systems, Inc., Lawrence, Kansas) in a standard, three-electrode configuration.⁶³ The electrode

was clamped to the bottom of a single compartment, three-neck, glass electrochemical cell. A Viton o-ring (i.d. 0.5 cm) placed between the cell opening and the electrode surface ensured that a reproducible area of 0.2 cm² was exposed to electrolyte solution. Contact was made to the diamond electrode by pressing a piece of nickel foil against the entire film surface outside the o-ring. A neoprene rubber spacer was cut to the same dimensions of the nickel foil and used to press the foil into contact with the electrode surface. Contact to the ITO electrode was made with a toothless alligator clip clamped to a portion of the conductive surface outside the o-ring. The o-ring was sonicated for 10 min in ultrapure water, rinsed with distilled isopropanol (IPA), and dried under a stream of N₂ before use. Once mounted in the cell, the electrode was soaked in distilled isopropanol (IPA) for 20 min and then rinsed thoroughly with distilled water. The cell was then filled with the electrolyte solution of interest. N₂ was bubbled through the solution for 10 min to remove dissolved oxygen and the solution was blanketed with the gas during the entirety of a measurement. The auxiliary electrode was a large-area carbon rod, rinsed with distilled IPA and dried under N₂ between measurements. The reference was a commercial Ag/AgCl electrode filled with 4 M KCl saturated with AgCl (0.197 V vs NHE). The reference electrode was placed in a cracked-glass capillary filled with the supporting electrolyte.

Optical Microscopy. Optical micrographs were captured using an Olympus metallurgical microscope (Scope BX60M, Olympus America, Inc., Melville, NY)

fitted with a digital camera (DP11, Olympus America, Inc., Melville, NY). Images were collected using an optical polarization filter in order to highlight the different domains in the ITO film.

Electrochemical Atomic Force Microscopy (ECP-AFM) Measurements. Scanning probe microscopy was performed using a Nanoscope IIIa multimode microscope (Digital Instruments/Veeco Metrology Group, Santa Barbara, CA). Double-sided tape was used to attach the ITO electrode to the magnetic sample holder disk, which held the sample in place on the piezo X-Y scanner. Electrical connection between the conductive surface of the ITO and the magnetic disk was made with Ag paint applied to the corners of the square sample. Electrical connection to the conductive surface of the diamond/quartz OTE was made with fine wire affixed to the corners with conductive tape. A small volume of the electrolyte solution was applied to the electrode surface using a syringe with a luer-style connection that was inserted into a port in the glass cantilever holder. An Ag wire served as a quasi-reference electrode, and a coiled Pt wire was used as the counter electrode. The reference and counter electrodes were inserted into the electrolyte solution through separate ports in the cantilever holder. The electrolyte solution was removed and replaced periodically as the gas bubbles evolved during polarization collected in the cell. The cantilevers used were 200 μm narrow-leg and triangular with a spring constant of 0.06 N/m. Roughness calculations were made using the root-mean-square (rms) roughness calculation script available in the image analysis software. The films were extremely flat, so

the roughness calculation was performed without the use of any plane fitting scripts.

XPS Measurements. XPS spectra for the ITO film were obtained with a Perkin Elmer XPS system using the $K\alpha$ line of an Al anode operated at 15 kV and 300 mA, at 90° incidence. An aperture of 4 mm was used. The sample chamber was maintained at a base pressure of ca. 10^{-10} Torr. The ITO/quartz OTE was mounted on a steel sample holder, and electrical connection was made from the conductive ITO surface to the metal holder with a small piece of Cu. The effectiveness of this electrical connection at reducing surface charging was confirmed by measuring the C(1s) spectrum with and without the Cu foil, and noting a significant peak shift. The reported spectra are accumulations of 25 scans, except in the case of Sn, for which 50 scans were accumulated. In calculations of the relative atomic percent, the increased number of Sn scans was corrected by dividing the Sn intensity by a factor of two. The following sensitivity factors were used in the calculations: In, 2.85; Sn, 3.2; O, 0.66.⁹³ Peaks were fit using XPS Peak 4.0 software and applying a Shirley baseline. No In or Sn oxide or metal reference materials were analyzed, as in the work by Donley et al.,⁹⁴ therefore, peak deconvolution was not possible.

4.3 Results and Discussion

Solution Exposure Tests. The stability of the optical, electrical, and electrochemical properties of diamond and ITO film electrodes were compared before and after the solution exposure tests. In the first series of tests, the electrodes were soaked for 48 h in different organic solvents, and in strong acid and alkaline solutions at room temperature. UV-Vis transmission spectra and electrical resistivity measurements were made for the electrode. The resistivity values are summarized in Table 4-1.

Table 4-1. Resistivity data for ITO/quartz and diamond/quartz OTEs before and after exposure to different organic and aqueous solutions.

<i>Solvent/Solution</i>	ρ ($\Omega\text{-cm}$) <i>before soak</i> <i>ITO</i>	ρ ($\Omega\text{-cm}$) <i>after soak</i> <i>ITO</i>	ρ ($\Omega\text{-cm}$) <i>before soak</i> <i>Diamond</i>	ρ ($\Omega\text{-cm}$) <i>after soak</i> <i>Diamond</i>
Hexane	3.8×10^{-5}	3.8×10^{-5}	4.2×10^{-2}	5.4×10^{-2}
Toluene	3.8×10^{-5}	3.8×10^{-5}	4.2×10^{-2}	6.0×10^{-2}
Methanol	3.8×10^{-5}	3.7×10^{-5}	4.2×10^{-2}	5.5×10^{-2}
1 M NaOH	3.8×10^{-5}	$> 10^3$ 4.82×10^{-5}	4.2×10^{-2}	4.7×10^{-2}
1 M HNO ₃	3.7×10^{-5}	$> 10^3$ 3.46×10^{-5}	4.2×10^{-2}	5.1×10^{-2}
dichloromethane	3.8×10^{-5}	$> 10^3$	4.2×10^{-2}	4.5×10^{-2}

There were no significant changes in the electrical resistivity of either the

diamond/quartz or the ITO/quartz OTE after soaking in hexane, toluene, or methanol. It is clear from the data that ITO possesses a lower resistivity than diamond. Even so, the resistivity of the diamond/quartz OTE is sufficiently low for electrochemical measurements to be made. In dichloromethane, the resistivity of the diamond/quartz OTE was unchanged; however, the resistivity of the ITO/quartz OTE increased by several orders of magnitude. This solvent appears to dissolve the ITO from the quartz surface. Optical microscopy revealed that the dissolution occurs only in some regions, leaving behind isolated patches of ITO poorly connected with one another. Therefore, the resistivity increases.

Immersion in the two aqueous solutions causes no change in the resistivity of the diamond/quartz OTE. The variability in the properties from batch-to-batch are, however, revealed in the ITO/quartz data, as resistivity measurements for two different batches are presented. For one batch, the resistivity is unchanged after exposure to either strong acid or base. On the other hand, the resistivity of another batch increased by several orders of magnitude after immersion in either solution. For this film, optical microscopy revealed the film dissolved from the surface, causing the increased resistivity. In summary, the electrical resistivity of the diamond/quartz OTE is quite stable in all the organic and aqueous solutions tested. The resistivity of the ITO/quartz OTE is stable during exposure to hexane, toluene, and methanol. The ITO/quartz OTE can clearly not be used in dichloromethane, and some batches are

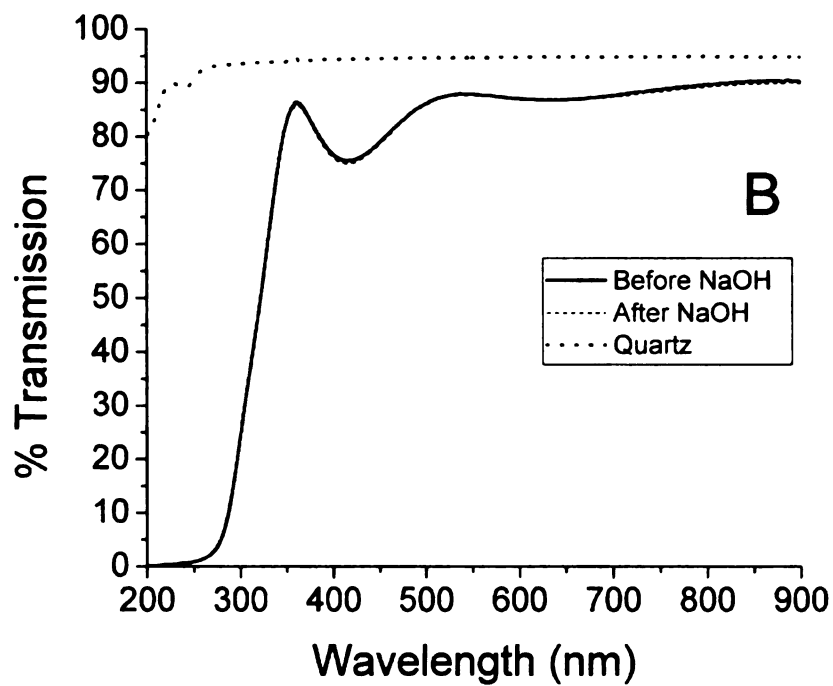
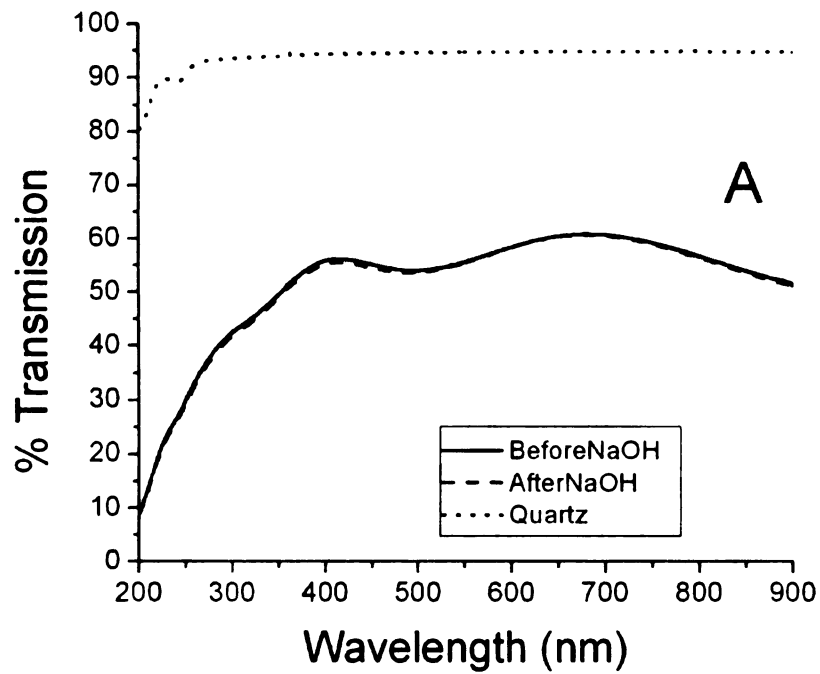


Figure 4-1. Comparison of UV-vis spectra for as-deposited (A) diamond/quartz and (B) ITO/quartz after a 48 h soak in 1 M NaOH. The spectrum for bare quartz is also shown for comparison.

chemically unstable in strong acid or alkaline solution.

Figure 4-1A presents transmission spectra for the diamond/quartz OTE before and after soaking in 1M NaOH. The transmission spectrum for uncoated quartz is shown for comparison. Like the electrical resistivity, it is clear that no change in the optical properties occurs during immersion. The same excellent stability is observed for the electrode after exposure in 1 M HNO₃. Transmission in the visible region is ca. 60%, whereas transmission for a 20 nm-thick ITO/quartz OTE, presented in Figure 4-1B is ca. 80% and is unchanged after immersion in NaOH. As discussed in the previous Chapter, the majority of the attenuation for diamond results from absorbance losses due to the nitrogen and boron impurity bands, based on preliminary specular reflectance/transmittance measurements.

Transmission spectra for an ITO/quartz OTE, before and after soaking in 1 M NaOH, are presented in Figure 4-1B. The reference spectrum for bare quartz is also presented. Clearly, no differences exist in the optical throughput for this particular film after solution exposure. There were also no significant changes in the optical properties of this particular batch of ITO after soaking in 1 M NaOH.

If the solution exposure causes film dissolution or chemical attack (oxidation), as in the case for the one batch of ITO studied, an increase in the

optical transmission (especially below 300 nm) would be expected and was in fact observed. In summary, the optical properties of the diamond/quartz OTE are extremely stable during exposure to strong acidic and alkaline media. The stability was reproducible from film-to-film. On the other hand, one batch of ITO/quartz exhibited excellent optical property stability during exposure to strong acid or base, while another exhibited poor stability due to film dissolution.

Polarization Experiments. Cyclic voltammetric i-E curves for a diamond/quartz OTE in 1M HNO₃ and 1 M NaOH are presented in Figure 4-2A. Diamond has a larger potential window in acid than does ITO (ca. 3 V vs. 2.5 V). The same i-E curves are plotted in an expanded version in Figure 4-2B. The curve exhibits a stable current (unchanging with time) within the featureless double layer region. The magnitude of the anodic current at +100 mV is 1 μA at 25 mV/sec. This value agrees with low background current previously reported for diamond/quartz electrodes,³ which tend to be slightly larger than the current for films deposited on Si.¹⁶ The curve in acid is stable and featureless over the entire potential range between the anodic current increase at 1200 mV, presumably due to oxygen evolution, and hydrogen evolution at -700 mV. The cathodic current at -700 mV may also contain a contribution from the reduction of oxygen, which is presumably generated during the positive sweep. The UV-Vis transmission spectrum in Figure 4-3 shows no change in the optical properties of the film following potential cycling in acid. Table 4-2 demonstrates that there is also no change in resistivity following polarization in 1 M HNO₃.

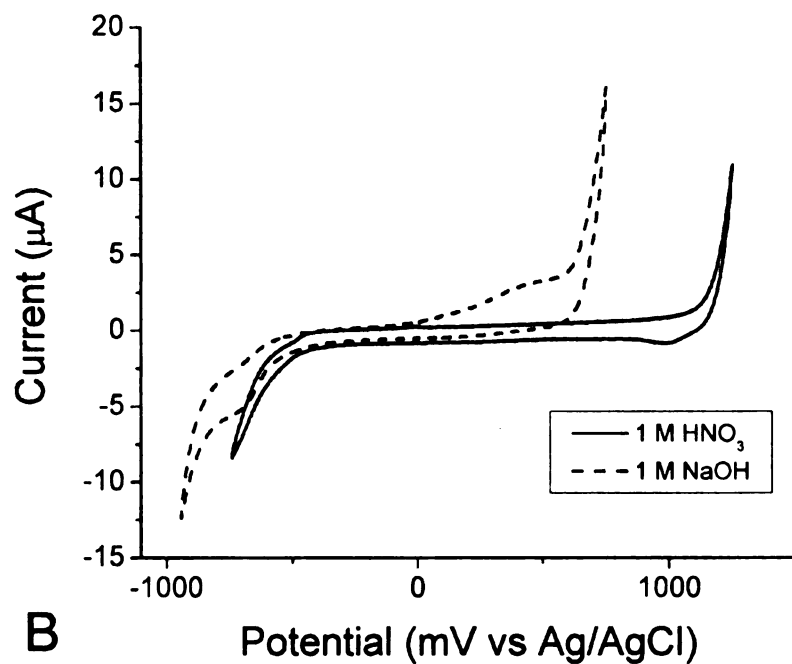
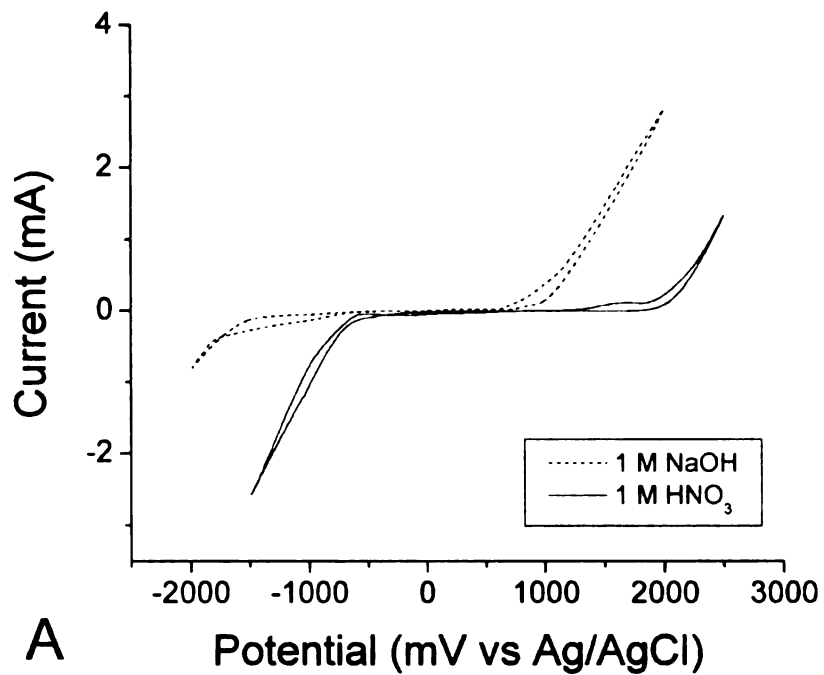


Figure 4-2. Cyclic voltammetric i-E curves for a diamond/quartz OTE in 1 M HNO₃ and 1 M NaOH at 25 mV/sec. Electrode geometric area = 0.2 cm².

Table 4-2. Comparison of ITO and boron-doped diamond resistivity before and after polarization in acidic and alkaline media.

<i>Film Treatment</i>	<i>ITO Resistivity ($\Omega\text{-cm}$) (Several films)</i>	<i>Boron-Doped Diamond Resistivity ($\Omega\text{-cm}$) (One film)</i>
As Deposited	$3.46(\pm 0.3) \times 10^{-5}$	$9.1(\pm 2) \times 10^{-2}$
Polarize in 1 M HNO ₃	∞	$9.9(\pm 3) \times 10^{-2}$
Polarize in 1 M NaOH	∞	$8.9(\pm 3) \times 10^{-2}$

The diamond/quartz OTE was cycled between -2.0 to +1.8 V at 25 mV/sec in 1 M NaOH at 25 mV/sec. The cyclic voltammetric i-E curve is presented in Figure 4-2A, and in Figure 4-2B. In 1M NaOH, anodic current begins to flow near 250 mV. This current flows just prior to the onset of oxygen evolution at 500 mV. On the reverse sweep, cathodic current begins to flow at ca. -750 mV, prior to the onset of hydrogen evolution at -950 mV. The current at -750 mV is likely associated with the reduction of dissolved oxygen formed during the positive sweep. These features appear to be linked, as the anodic feature is not observed when the negative-going scan is reversed at -300 mV. The polarization experiment in alkaline media revealed that the electrical and optical properties are extremely stable. There was no change in the UV-Vis transmission spectrum for the diamond/quartz OTE after cycling in 1 M NaOH, as shown in Figure 4-3. The transmission spectrum for the diamond/quartz OTE

was unchanged after polarization in either 1 M HNO₃ or 1 M NaOH. Table 4-2 shows that there was also no significant increase in the resistivity after the over 2-h polarization in 1 M NaOH.

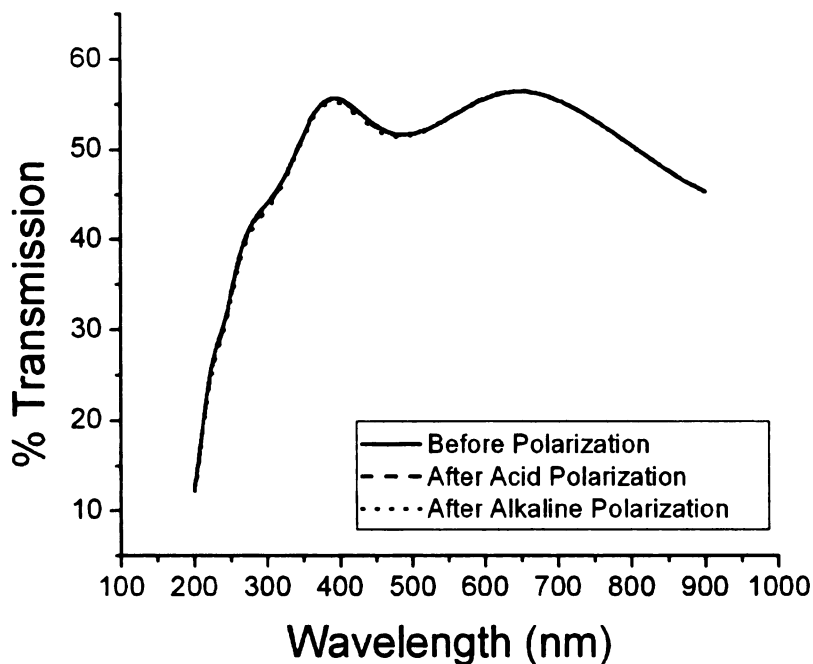


Figure 4-3. UV-Visible transmission spectra for (a) diamond/quartz OTE after potential cycling in both 1 M HNO₃ and 1 M NaOH. Potential cycling was performed for 2.5 h

The ITO/quartz OTE was also polarized in acidic and alkaline media at 25 mV/sec. Cycling was performed until electrical contact with the electrodes was lost due to film degradation, usually this occurred within 10-15 cycles (0.5 to 1 h). UV-Vis transmission spectra and resistivity measurements were made before and after the polarization. Figure 4-4A presents a series of cyclic voltammetric i-E curves in 1M HNO₃. The potential was cycled between 2.6 and -0.9 V vs

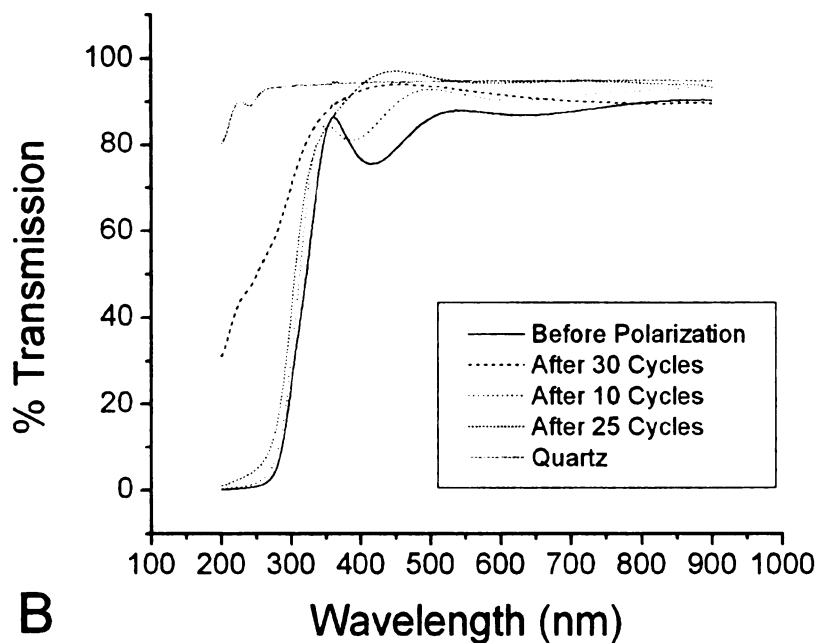
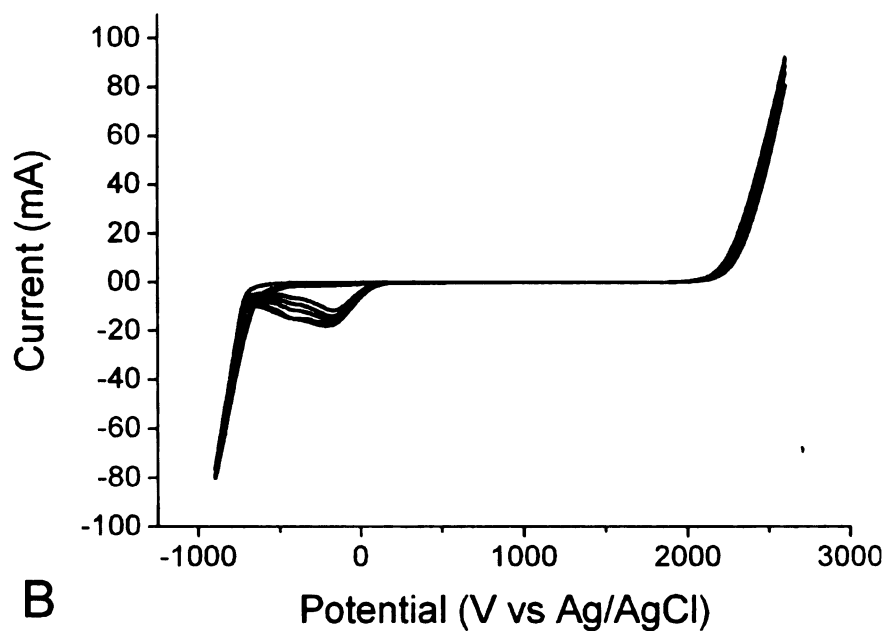


Figure 4-4. (a) Cyclic voltammetric i-E curves for an ITO/quartz OTE in 1 M HNO_3 at 25 mV/sec (cycles number 14-19) (b) transmission spectra for the ITO/quartz OTE after potential cycling in 1 M HNO_3 .

Ag/AgCl, and curves are presented for cycle numbers 14 through 19. Oxygen and hydrogen evolution currents in excess of 7 mA (35 mA/cm²) are observed at the potential limits. The large cathodic current feature at ca. -0.25 V is attributed to the reduction of oxygen produced at the electrode surface during the positive sweep. Evidence for this is the fact that the current was not observed in cycles immediately after degassing of the solution with N₂, or if the positive-going scan was reversed at 300 mV (prior to O₂ evolution). The current crossover observed in the curves extending to -1.9 V is evidence for some sort of change in the film microstructure and or chemistry. The current crossover may be associated with the reduction of the Sn and/or In oxides in the film. Based upon the standard reduction potentials of Sn⁴⁺/Sn⁰, Sn²⁺/Sn⁰, and In³⁺/In⁰, we suppose that both the Sn and In cations may be reduced to their metallic states during the negative potential excursion to -1.0 V. The standard reduction potentials for Sn^{4+/2+} and Sn^{2+/0} are +0.154 V and -0.138 V, respectively.⁹⁵ The standard reduction potential for In^{3+/0} is -0.335 (as Pt and Hg amalgams).⁹⁶ In acidic solution, it is our contention that the metal oxides in the film are reduced to a product that is soluble in the solution and removed from the surface.

Dissolution of the oxide reduction reaction products would be expected to increase the optical transmission. The transmission spectra for the ITO/quartz OTE before and after cycling in 1 M HNO₃, are seen in Figure 4-4B. The feature at ca. 375 nm decreases in magnitude with cycle number, completely

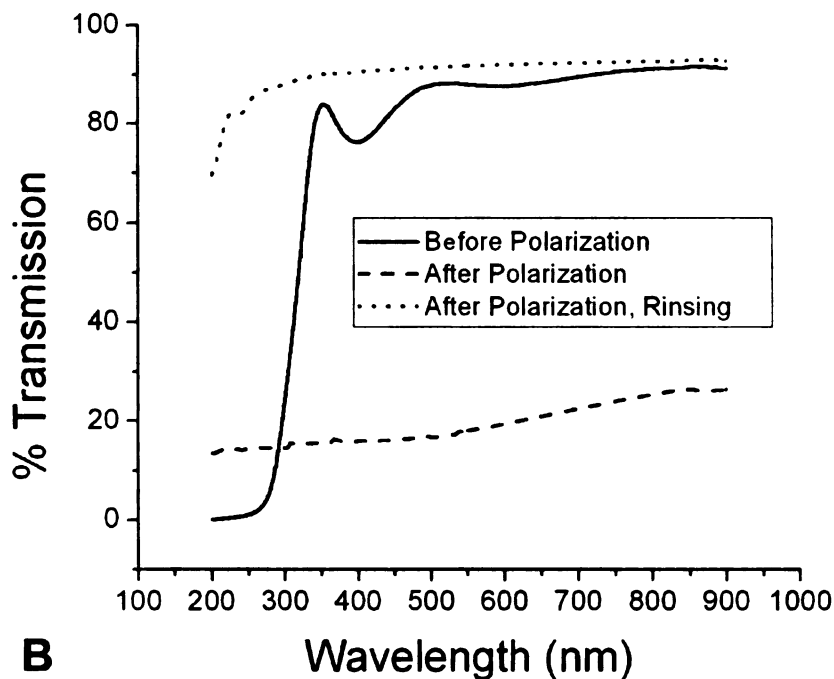
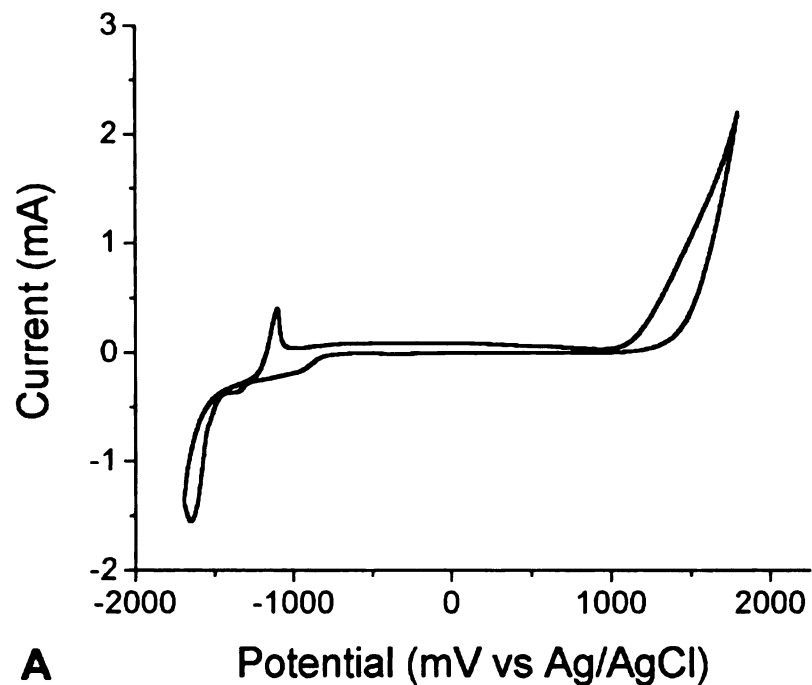


Figure 4-5. (a) Cyclic voltammetric i-E curves for an ITO/quartz OTE in 1 M NaOH at 25 mV/s (cycle 10) and (B) transmission spectra for ITO/quartz OTE after potential cycling 1 M NaOH. Potential cycling was performed for 10 cycles.

disappearing after 30 cycles. The absorption edge at ca. 300 nm progressively shifts toward shorter wavelengths and the transmissivity increases in this region with potential cycling. This is attributed to the progressive loss of some ITO from the quartz surface. Consistent with this is the fact that the film resistivity increased to greater than 300 M Ω -cm. The data are consistent with isolated loss of ITO from the quartz surface.

A cyclic voltammetric *i*-*E* curve for an ITO/quartz OTE cycled in 1 M NaOH, between 1750 and -1700 mV at 25 mV/sec, is shown in Figure 4-5A. The onset potentials for oxygen and hydrogen evolution are offset from those in 1 M HNO₃ by ca. 1000 mV, which is close to the 840 mV shift predicted based upon the 14 unit pH difference between the two solutions (60 mV/pH). Sweeping the potential in the positive direction from 0 V causes anodic current to flow at ca. 1000 mV. Presumably, this current is associated with O₂ evolution. This anodic current reaches a maximum of 2 mA at the reversal potential of 1750 mV. On the reverse sweep, cathodic current begins to flow at ca. -800 mV and reaches a relatively constant value of a few hundred microamps. This is followed by a sharp increase in cathodic current starting at ca. -1500 mV, which is presumably due to hydrogen evolution. On the positive sweep, the cathodic current flow decreases without crossover. At -1100 mV, a sharp and symmetric anodic current feature is observed. This peak is far negative of the thermodynamic redox potentials of either Sn or In, so it does not likely represent stripping of

these metals from the ITO surface. This current feature decreased in magnitude with cycle number. In alkaline media, we propose that insoluble reduction reaction products, perhaps hydroxides, remain on the surface. Pourbaix diagrams show that the thermodynamically stable form of In at -0.8 V vs Ag/AgCl is In^0 at $\text{pH} = 0$, and InO^{2-} in $\text{pH} = 14$.⁹⁶ Similarly, the thermodynamically stable form of Sn at this potential is Sn^0 at $\text{pH} = 0$ and SnO^{2-} at $\text{pH} = 14$.⁹⁵ It can be surmised from this thermodynamic information that the In_2O_3 and SnO_2 species in the ITO film would not be stable during cathodic potential sweeps in either acidic or alkaline media.

Upon removal from the cell, the ITO electrode was discolored and opaque after potential cycling in 1 M NaOH. The opaque material reduced the amount of light transmitted through the film. The opaque material was easily rinsed from the quartz surface, though, with a stream of water, and this increased the amount of light transmitted through the film. These changes in optical properties are shown in Figure 4-5B. This is consistent with the removal of a possible metal hydroxide phase from the quartz surface. This increase in transmissivity together with the increased electrical resistivity is consistent with the removal of ITO from the quartz substrate. Blackening of SnO_2 films during positive potential sweeps immediately following negative polarization was first reported by Kirkov.⁸⁸ Laitinen et al. suggested the blackening of the film was due to the reduction of SnO_2 electrodes to Sn^0 during polarization in 1 N HCl to potential limits of $+1.5$ and -0.5 V vs SCE.⁹⁰ However, this report did not confirm whether the observed

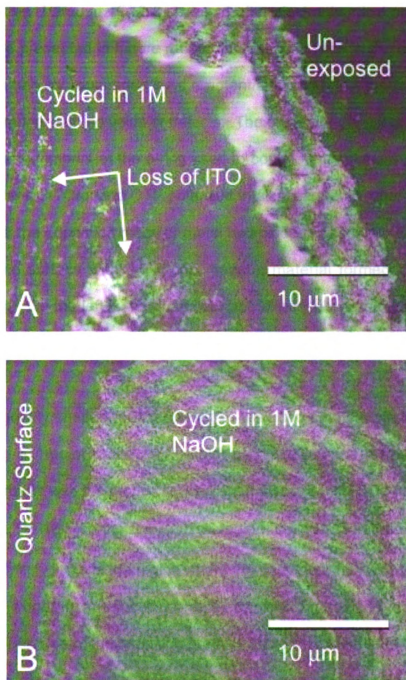


Figure 4-6. Optical micrographs of (A) polarized and unpolarized (1 M NaOH) regions of an ITO/quartz OTE and (B) a polarized (1 M NaOH) ITO/quartz OTE showing the metallic or metal hydroxide phases formed and the bare region where some of these phases were removed by rinsing.

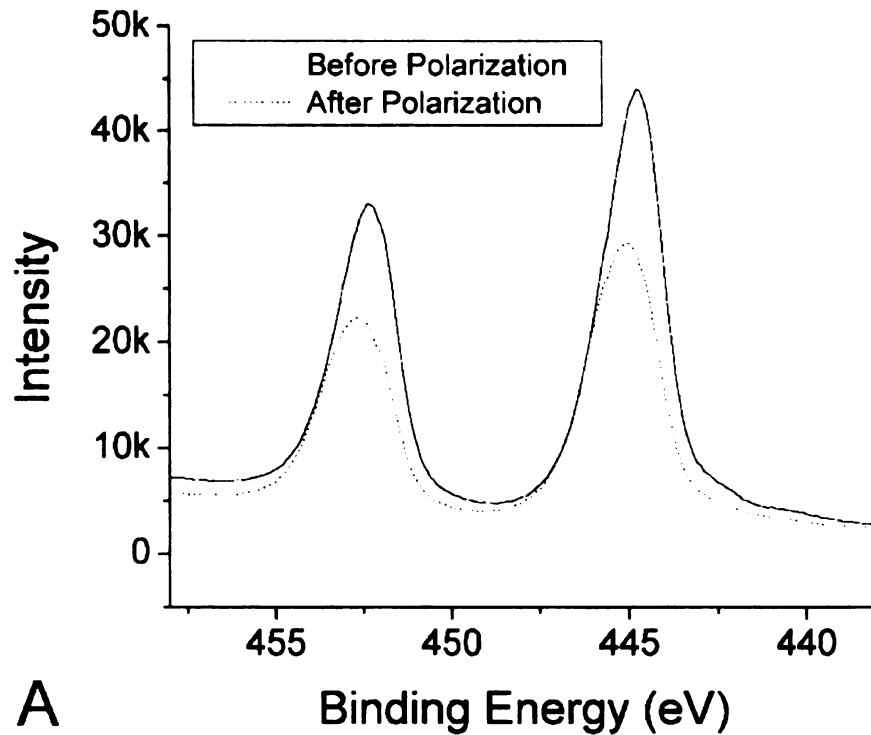
change in the film was the reduction of the SnO₂, or another process. Optical micrographs of the ITO/quartz OTE before and after electrochemical polarization in 1M NaOH are presented in Figure 4-6A. The exposed area in the bottom-left of the image is heavily roughened by the potential cycling, but the unexposed area appears smooth with no voids or defects. The observed disruption between the two areas is the imprint of the o-ring used to confine the solution. Figure 4-6B shows a different ITO/quartz OTE polarized in alkaline media, after rinsing to remove some of the deposited metal or metal hydroxide phases. On the right of the image is the surface with the rough, opaque material formed during the potential cycling. On the left is the quartz surface exposed where the stream of water rinsed away the reaction product(s).

The irregularly shaped, opaque features were too small to measure their resistivity using a 4-point probe. Two-point probe resistance measurements were therefore made with the probes spaced apart by ca. 2 mm. The resistances measured were ca. 18 Ω in the unpolarized region, ca. 110 Ω in the discolored regions, and infinitely large in the region where the dark material was removed by rinsing. If the oxides are reduced to metal or metal hydroxides insoluble in alkaline media, particles of the reduction product would be expected to crystallize from solution, possibly on the electrode surface near the location of their reduction. In this scenario, the discolored regions of increased resistivity could represent discontinuous domains of intact polycrystalline ITO, hydroxide, and metal particles, with a disrupted, less conductive structure than the unpolarized

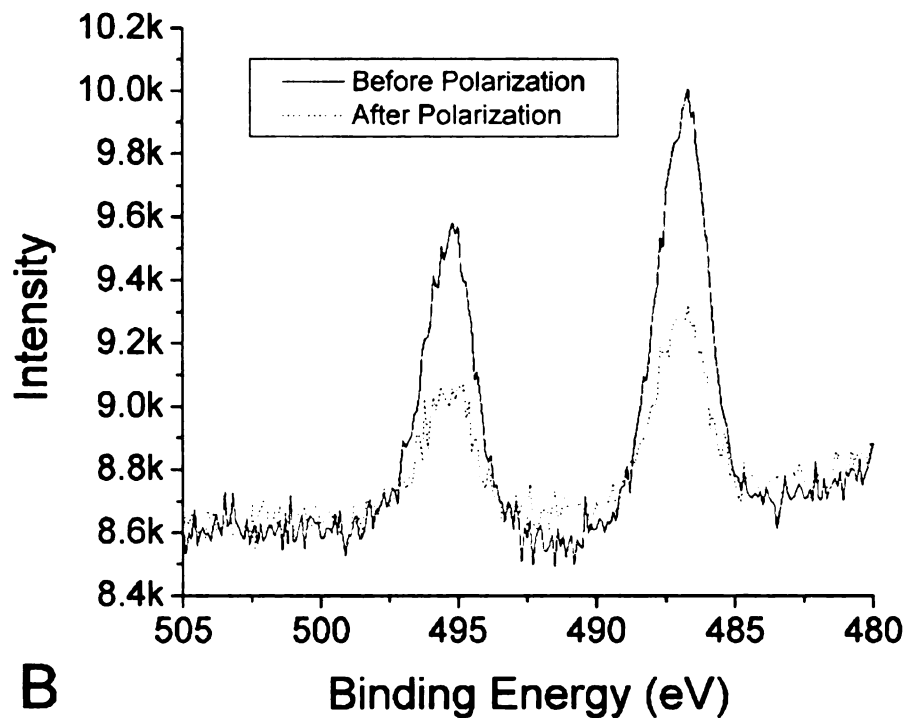
ITO.

The reproducibility of the diamond/quartz OTE's optical, electrical, and electrochemical properties were superb from film-to-film. On the other hand, ITO is notoriously variable in terms of (i) its chemical nature, (ii) the distribution of crystalline and amorphous regions, (iii) the tin oxide, indium oxide and hydroxide content,⁹⁴ and (iv) electronic properties.⁹⁷ The surface chemistry, modified by either intentional modification or adventitious adsorption of contaminants, can impact the properties of ITO, particularly the work function.⁹⁸ Thus, the heterogeneous nature of ITO often leads to significant variability in the optical and electrochemical properties from film to film.^{94, 97, 98}

XPS measurements. XPS was used to explore the chemical nature of the films before and after polarization in 1 M HNO₃. Because ITO consists of In₂O₃ and SnO₂, chemical shifts for In, Sn, and O were used in the analysis. In previous studies, XPS and Auger spectra for ITO films were compared with those for In foil, Sn foil, SnO₂, In₂O₃, and In(OH)₃ standards, revealing that the surface chemistry varies with source and method of pre-treatment.^{94, 99} In the present work, no spectra were measured for standards. Therefore, reliable identification of individual chemical species cannot be made based on the present research. However, shifts in the peak binding energies and changes in the relative elemental ratios are reported as a demonstration of chemical instability.



A



B

Figure 4-7. XPS spectra for (a) In_{3d5} , (b) Sn_{3d5} in an ITO/quartz film before (solid), and after (dashed) polarization in 1 M NaOH.

Figure 4-7A presents the In_{3d5} spectra for an ITO/quartz film before and after polarization in 1 M NaOH. The majority of the material in the as-deposited film is expected to be in the In_2O_3 form, which makes up the bulk of ITO crystallites. A smaller amount may be in the $\text{In}(\text{OH})_3$ form, produced by hydrolysis of In_2O_3 , and previously shown to have a chemical shift of higher energy (444.8 eV).



The shift for In^0 has been reported at a lower binding energy than In_2O_3 , 443.2 eV. Upon polarization in 1 M NaOH, the peaks in Figure 4-7A are decreased in area and intensity, and exhibit a small shift to higher binding energy from 444.8 to 445.1 eV. The Sn_{3d5} spectra for these films are presented in Figure 4-7B. The S/N ratio is too low in this measurement to report whether the peaks are shifted after polarization, however, a decrease in peak intensity after polarization is observed. The decrease in the peak intensities upon polarization in 1 M NaOH for both In and Sn is consistent with a loss of material from the surface. This result is in agreement with the increase in film resistivity and loss of electrical contact upon polarization discussed earlier. While contact was lost with the ITO/quartz OTE during polarization in 1 M NaOH, the XPS spectra reveal In and Sn still exist on the electrode, but in lesser amounts. This indicates that domains on the surface are not in good electrical contact with one another. A ratio of $\text{Sn}_{3d5}/\text{In}_{3d5}$ peak intensities, corrected for elemental sensitivity factors and

sampling time, decreased slightly upon polarization, from 1.5% to 1.1%. This may represent a preferential loss of Sn from the film during polarization.

The O_{1s} spectra presented in Figure 4-8, recorded before and after polarization on 1 M NaOH, show evidence for a chemical change after polarization. There is a reduction in the initial peak intensity at 530 eV and development of a new peak after polarization. There is a clear shift to higher binding energy (to ca. 533 eV) upon polarization. Donley et al. fit this peak using four features: 529.5 eV, O in In_2O_3 ; 531.8 eV, O in hydroxides; and 530.6 eV, O

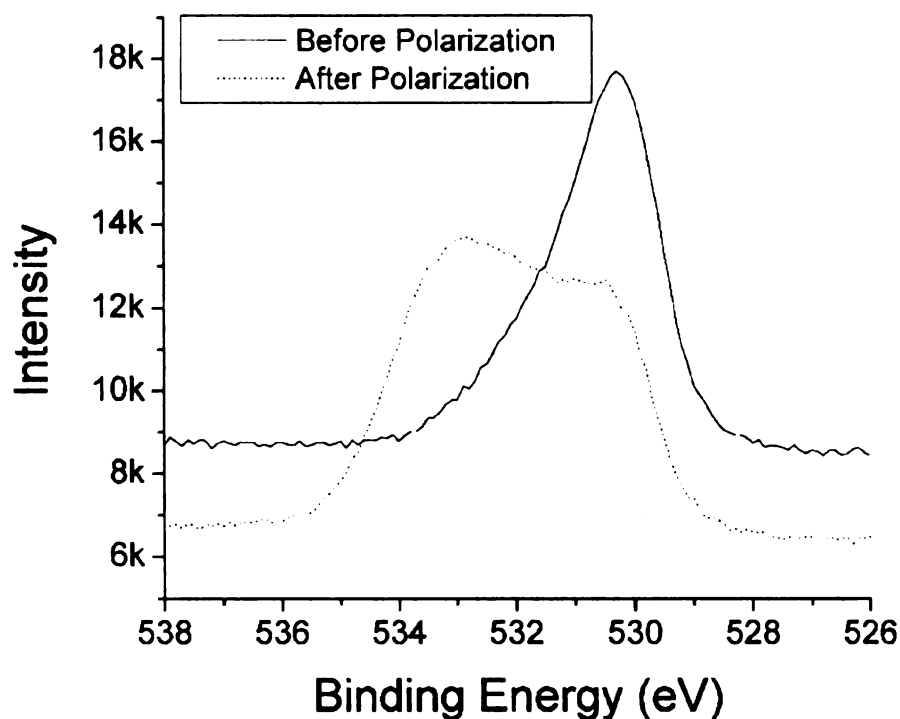


Figure 4-8. XPS Spectrum for O_{1s} in as-deposited ITO film (solid), and in ITO film after polarization in 1 M NaOH (dashed).

in the ITO lattice adjacent to oxygen deficiency sites. The observed 3 eV shift in Figure 4-8 reflects the existence of oxygen-containing species other than In_2O_3 , consistent with the formation of hydroxides. In fact, the shape of dashed trace in Figure 4-8 is similar to the spectrum reported by Donley et al. for an indium hydroxide standard. The observed shift in the O1s peak, possibly due to the formation of In and Sn hydroxides, is clear evidence that the ITO/quartz OTE is chemically unstable under polarization in 1 M NaOH. The blackening of the film and loss of light transmission discussed previously is consistent with the formation of hydroxide species on the ITO/quartz surface.

Electrochemical Atomic Force Microscopy (EC-AFM). Morphological changes in the surface of the diamond/quartz and ITO/quartz OTEs brought about by the electrochemical polarization were probed using electrochemical AFM. Noteworthy is the fact that no morphological changes were observed on the diamond/quartz surface after potential cycling in either acidic or alkaline media! The top row of AFM images in Figure 4-9 compares the surface of a diamond/quartz OTE surface before cycling (left), after 12 cycles in 1 M HNO_3 (center), and 12 cycles in 1 M NaOH (right). All potential cycling was from -2.5 to +2.5 V at 100 mV/sec. Film roughness is 17 nm before cycling, 17 nm after cycling in HNO_3 , and 16 nm after cycling in NaOH. The absence of any morphological changes is consistent with the stable optical transparency, as reflection and scattering losses would be sensitive to changes in the surface morphology. Also, no changes were observed in diamond/quartz OTE resistivity

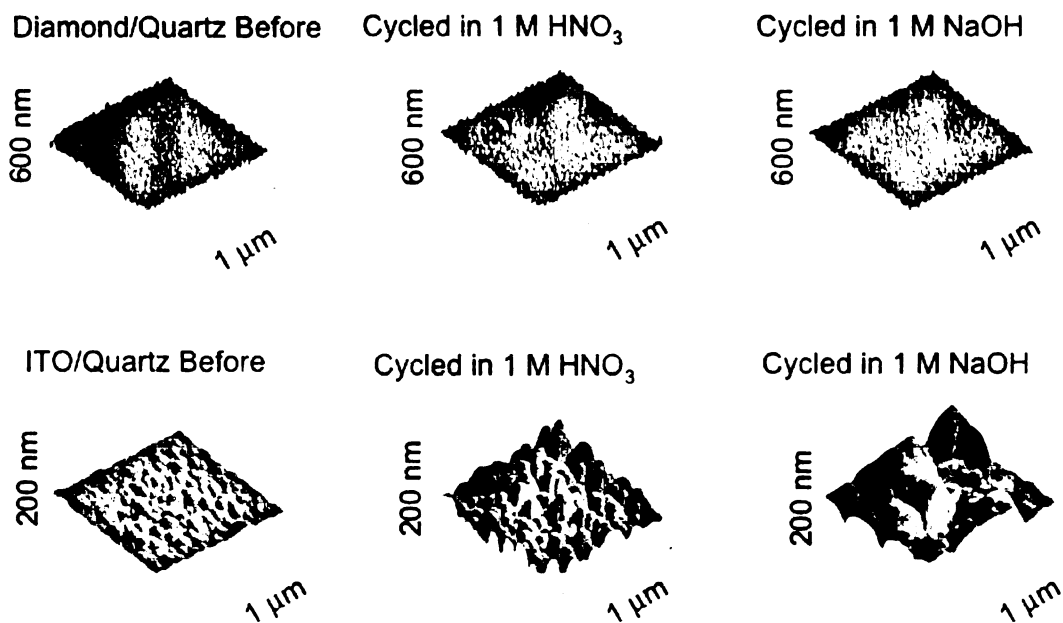


Figure 4-9. AFM micrographs of boron-doped diamond/quartz OTE (top row) and ITO (bottom row). In each row, as deposited (left), after cycling in 1 M HNO₃ (center) and after cycling in 1 M NaOH (right).

after these measurements, which reflects the stability of the electrical properties.

In contrast with the morphological stability of the diamond/quartz OTE, changes in the ITO/quartz surface are significant after polarization. The bottom row of AFM images in Figure 4-9 compares images of the ITO/quartz OTE surface before (left), after polarization in 1 M HNO₃ (center), and after polarization in 1 M NaOH (right). The surface before polarization has a nodular surface with an rms surface roughness of 3 nm. The surface features are ca. 100 nm in diameter and ca. 15 nm in height. The particles coalesce to form a

continuous film across the surface with boundaries where they join together. The image after 30 potential cycles in 1 M HNO₃ between +2.0 and -0.8 V shows significant roughening. The features have the same diameter as those for the film prior to polarization, but the nominal height is much greater, ca. 70 nm. Therefore, roughness increased from 3 to 17 nm. The change in particle height and film roughness reflects a change in morphology, perhaps due to dissolution of the film predominately at the grain boundaries. This is consistent with both the loss of electrical conductivity and the increase in optical transmissivity, as described above, and the loss of electrochemical signal. After the 30th cycle in 1 M HNO₃, no current response was measured for the electrode in the voltammogram. This indicates loss of electrical conductivity.

A more aggressive removal of material is evident after polarization in 1 M NaOH. This film was exposed to 20 potential cycles between -1.1 V and + 0.3 V. The potential did not exceed +0.3 V to ensure that any cathodic current observed was attributable to reduction of the ITO film and not to reduction of oxygen generated during the positive scan. The particles have a very large distribution of diameters, with many being larger than 200 nm. The surface roughness increased from 3 to 43 nm. The increase in particle size and roughness is consistent with reduction of oxides in surface particles to another material that is deposited in place, as suggested by XPS results. This observation is also consistent with the UV-vis transmission measurements, showing a decrease in transmission upon reduction in NaOH solution. The specific mechanisms of ITO

degradation during potential cycling in acidic and alkaline media are under further investigation, but these results indicate that morphological changes do occur which affect the optical transparency and electrical conductivity.

Electrochemical Probe Species. While electrical contact with ITO/quartz electrodes was lost after ca. 10-15 potential cycles in both acidic and alkaline media, the diamond/quartz OTE shows no such degradation. The electrochemical activity of the electrode before and after cycling in acidic and alkaline media was evaluated using two redox systems: $\text{Ru}(\text{NH}_3)_6^{3+/2+}$ and $\text{Fe}(\text{CN})_6^{4-/3-}$. A cyclic voltammetric i-E curve of 0.1 mM $\text{Ru}(\text{NH}_3)_6^{3+/2+}$ in 1 M KCl collected at 100 mV/sec showed nearly reversible electron transfer kinetics with a ΔE_p of 62 mV (100 mV/sec). After the diamond/quartz OTE was sequentially polarized for 1 h each in both 1 M NaOH and 1 M HNO_3 at 25 mV/sec, ΔE_p was unchanged at 62 mV. The oxidation and reduction peak currents were limited by semi-infinite linear diffusion as the peak currents scaled proportionally with the square root of the potential sweep rate ($R^2 > 0.99$) before and after cycling. The heterogeneous electron transfer rate constant for this redox couple has been shown to be relatively insensitive to surface cleanliness, surface microstructure, and surface chemistry at diamond and other carbon electrode surfaces.^{62, 72, 73} It is most sensitive to the density of electronic states at the electrode surface available for charge transfer. The nearly reversible kinetics indicate that the conductivity of this new OTE is stable, even under extended potential cycling in acidic and alkaline media, and sufficient for the

electrochemical measurements. For example, the film resistivity, measured before and after cycling, was $1.43(\pm 0.23) \times 10^{-5} \Omega\text{-cm}$ and $1.49(\pm 0.38) \times 10^{-5} \Omega\text{-cm}$, respectively.

Cyclic voltammetric i-E curves for 0.1 mM $\text{Fe}(\text{CN})_6^{4-/3-}$ collected at 100 mV/sec before polarization had a ΔE_p of 86 mV, with peak currents varying linearly with the square root of the scan rate ($R^2 = 0.98$). After the potential cycling treatment in both acidic and basic media, the ΔE_p is 81 mV. The surface chemistry was altered during the polarization changes from a hydrogen surface termination to one containing oxygen. The $\text{Fe}(\text{CN})_6^{4-/3-}$ couple is known to be sensitive to the presence of surface oxides at carbon electrodes, with increased kinetics at sp^2 -bonded carbon surfaces, like glassy carbon, and decreased kinetics at sp^3 -bonded diamond electrodes.⁵² The observation that ΔE_p does not significantly change must mean that little surface oxygen was incorporated during the polarization. Clearly, the electrochemical response for both redox systems is unchanged by the polarization.

$i_p^{\text{ox,red}}$ for both systems is close to the value predicted for this concentration according to the equation:

$$i_p = (2.69 \times 10^5) n^{3/2} A D_0^{1/2} v^{1/2} C_0^*$$

4.7 μA , assuming a diffusion coefficient of $7.6 \times 10^{-6} \text{ cm}^2/\text{sec}$ ⁷⁴ and a scan rate of

100 mV/sec. I_p^{ox} is 6.4 μA for $Fe(CN)_6^{4-/3-}$, and 4.1 μA for $Ru(NH_3)_6^{3+/2+}$, both after potential cycling.

4.4 Conclusion

The diamond/quartz OTE shows superb chemical stability in harsh chemical environments, compared to a commonly used OTE material, ITO. While ITO enjoys widespread use as an OTE, evidence presented herein demonstrates that it possesses limitations. The properties are unstable during exposure to dichloromethane, strongly acidic or basic solutions (some batches), and polarization at negative potentials greater than -1 V. When such potentials are applied to this electrode, evidence suggests reduction of ITO, likely to indium and tin hydroxides, which are dissolved in acid and deposited in alkaline media. OTE optical and electrochemical properties begin to resemble those of the substrate as treatment progresses in time. This instability in optical and electrical properties would be unacceptable in spectroelectrochemical measurements. In comparison, boron-doped diamond thin-films are optically and electrochemically stable under these conditions. After potential cycling in 1 M NaOH and 1 M HNO₃ for over two hours each, optical properties were unaffected in the UV-Visible region of the electromagnetic spectrum, as was the film morphology, as observed by EC-AFM. Resistivity of the films was likewise unaffected by this treatment. The diamond/quartz OTEs exhibit superb electrochemical stability under this harsh chemical treatment, as the electrochemistry of $Fe(CN)_6^{4-/3-}$ and $Ru(NH_3)_6^{3+/2+}$ at these electrodes remains

active after the polarization treatment.

The results demonstrate that the diamond/quartz OTE possesses material property stability far superior to that of ITO. The results portend the possibility of using the diamond/quartz OTE for chemical analysis in aggressive environments.

5 Cyclic Voltammetric Studies of 2-nitrophenol, 4-nitrophenol, and 2,4-dinitrophenol at Boron-Doped Diamond Electrodes

5.1 Introduction

Detection methods for trinitrotoluene (TNT), and related explosives and residues, are necessary in the search for land mines and for the characterization of munitions dumps and other environmental cleanup areas where TNT is present. A NATO workgroup "Detection of Explosives and Land Mines: Methods and Field Experience" in September 2001 reviewed the state of the art in land mine detection and concluded that "current sensor technologies are not sufficient for most mine action tasks. . ." ¹⁰⁰ Because the toxicity of these molecules is so potent, detection methods must be sensitive to detect toxicologically significant concentrations in environmental samples, including soil and water near military facilities. For example, the United States EPA Drinking Water Equivalent Levels (DWEL) are 200 ppb for 2-nitrophenol, and 20 ppb for 2,4,6-trinitrotoluene. ¹⁰¹ The DWEL is the chronic, non-cancer reference dose extrapolated to a concentration in drinking water for a person of 70 kg drinking 2 L per day. Reference dose is an estimate of a daily exposure level of a chemical that is not likely to cause disease. ¹⁰² Additionally, it is desirable to speciate the nitrotoluenes in environmental samples, as their toxicity varies.

The current EPA method for detecting nitroaromatics and nitroamines, Method 8330, involves reversed-phase HPLC separation on a C-18 column with UV detection at 254 nm, with confirmation by normal-phase HPLC separation on a cyano column with UV detection.¹⁰³ A field deployable, robust, rapid detection method with competitive figures of merit is foreseen using the spectroelectrochemical method with the diamond/quartz OTE, based on (i) the diamond potential window that extends to the negative potentials necessary to reduce the nitro functional group(s), (ii) the optical window of diamond that allows detection of the nitroaromatics in the UV-Vis region of the electromagnetic spectrum, and (iii) the stable optical and electrochemical properties of the diamond/quartz OTE in harsh chemical environments that would allow measurements of environmental samples of a wide range of pH conditions. For sure, the method would be useful to total nitroaromatic analysis and maybe be able to provide some specific information about the types of nitroaromatics present.

Electrochemical detection of the nitroaromatics is possible through the reduction of the nitro functional group(s) at potentials negative of ca. -800 mV. Cyclic voltammetric studies of the electrochemistry of nitrobenzene at Hg in aqueous media have been reported.¹⁰⁴⁻¹⁰⁶ A cyclic voltammetric i-E curve for 0.5 mM nitrobenzene in 50 mM LiCl at a DME (from reference 106) is presented in Figure 5-1. Starting at a potential near zero and scanning in a negative direction, a four-electron reduction wave is observed at ca. -800 mV. This four-electron

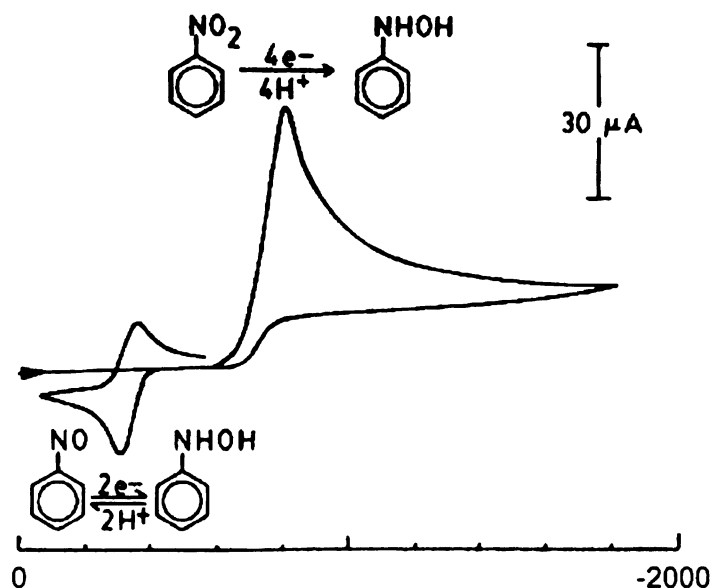


Figure 5-1. Cyclic voltammetric i-E curve for 0.5 mM NB in 50 mM LiCl at a mercury electrode (radius = 0.046 cm, scan rate = 50 mV/sec). (From McIntire, Blount, 1986)

reduction wave represents first, two one-electron, one-proton reductions ($0 e^-$ to $2 e^-$ in Figure 5-2), followed by a two-electron, two-proton reduction to hydroxylamine ($2 e^-$ to $4 e^-$ in Figure 5-2). In Figure 5-1, these reductions are observed as one combined wave, but the wave was separated into its two components when 50 mM sodium dodecyl sulfate (SDS) was added to the electrolyte solution. The first of these two waves, at less negative potentials, was chemically reversible. The larger wave, at more negative potentials than observed without SDS, was irreversible. Based upon ESR measurements, the first wave was attributed to the formation of a radical anion. It is thought that the SDS micelles provide a medium in which $NB^{\cdot-}$ is stabilized so that the first one-electron transfer is observed at less negative potentials than the reduction to hydroxylamine. The number of electrons per wave was determined by

chronocoulometry to be a ratio of ca. 1:4. The smaller wave was thus assigned to a one-electron reduction to $\text{NB}^{\cdot-}$. The larger wave was assigned to a four-electron reduction to phenylhydroxylamine.

Hydroxylamine can not be oxidized to nitrobenzene at Hg on positive sweeps from ca. -1800 mV, but a reversible, two-electron oxidation wave is observed at -1500 mV following the initial reduction to hydroxylamine. This oxidation wave was only observed following the formation of an hydroxylamine at ca. -800 mV, and it was assigned to the oxidation of phenylhydroxylamine to nitrosobenzene. On the subsequent negative sweep, a new two-electron reduction wave was observed at ca. -300 mV, representing the reduction of nitrosobenzene to hydroxylamine. The mechanism developed from this work is presented in Figure 5-2.

Rubenstein reported on the reduction of nitrobenzene at glassy carbon (GC) and Au electrodes, with the data being interpreted in light of the mechanism in Figure 5-2.¹⁰⁷ At pH 3 and 6, the reduction of NB to phenylhydroxylamine was observed, resulting in cyclic voltammetric i-E curves with the same shape as that presented in Figure 5-1. In both media, the four-electron reduction wave was larger on the first cycle than on subsequent cycles. After several cycles, the peak current for the reduction of nitrobenzene to hydroxylphenylamine reached a constant value at both electrodes. For both electrodes, the assignment of this wave to the four-electron reduction to hydroxylamine was based on the fact

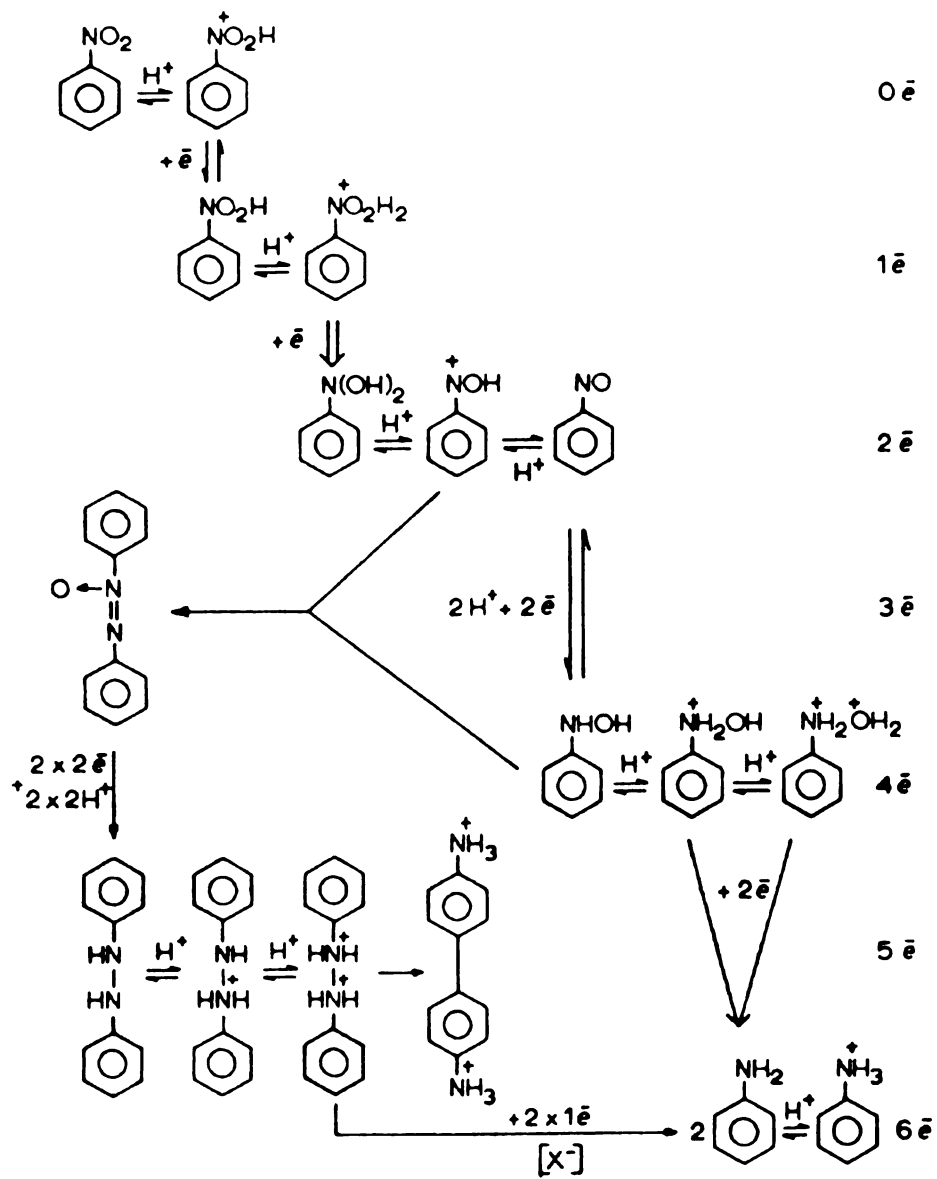


Figure 5-2. Proposed mechanism for nitrobenzene reduction, based on polarographic measurements at Hg. (From Heyrovsky and Vavricka, 1970)

that the first cycle peak current was consistent with the number of electrons transferred equal to 4-6. At both pH values, the kinetics were more reversible at Au than at GC. All three waves shifted by ca. 60 mV/pH unit at both electrodes,

indicating the involvement of equal numbers of protons and electrons in each redox process.

The voltammetric i-E curves were compared for nitrobenzene (NB) and nitrobenzene sulfonate (NBS) at Au in order to elucidate the effect of molecular structure on the electrode kinetics. For Au at pH 13, the reduction potential for NB was ca. 300 mV less negative than for NBS. The kinetics for both NB and NBS were more sluggish at GC than at Au. These observations demonstrate that the redox reaction proceeds through a specific interaction at both electrodes.

In the present study of the redox chemistry of nitroaromatics at diamond electrodes, preliminary studies were made using nitrophenols as model compounds. Nitrophenols have significantly lower toxicities than do the nitrotoluenes, but are expected to exhibit similar electrochemistry at diamond. Additionally, the UV-Vis absorbance features in the 225-300 nm range are expected to be similar. Selectivity for different nitrotoluenes may be possible based on differences in the reduction potential for the formation of phenylhydroxylamine, and to differences in the UV-Vis absorption spectrum. To investigate this, cyclic voltammetric i-E curves for 0.05 mM 2-nitrophenol, 4-nitrophenol, and 2,4-dinitrophenol were recorded at the diamond/quartz OTE in phosphate buffer, pH = 8, and are presented in Figure 5-3. The curves shown are for scan number ten, a point at which the i-E curve shape was unchanging.

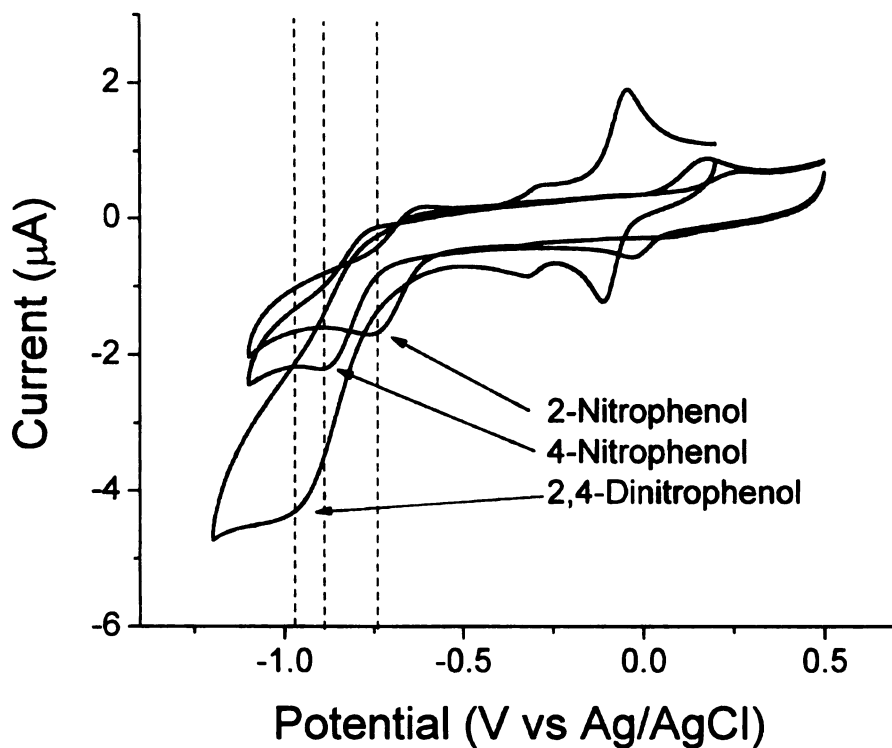


Figure 5-3. Cyclic voltammetric i-E curves for 0.05 mM 2-nitrophenol, 4-nitrophenol, and 2,4-dinitrophenol, in 10 mM phosphate buffer, pH 8.0. Scan rate, 50 mV/sec.

The primary reduction peak for 2-nitrophenol, 4-nitrophenol, and 2,4-dinitrophenol occurred at -750, -885 and -980 mV (E_p^{red}), respectively. The i_p^{red} for 2,4-dinitrophenol is twice as large as the values for 2-nitrophenol and 4-nitrophenol (4.5 vs 2.2 μA) due to the fact that the former has two nitro groups that can presumably be reduced. Clearly, the large reduction wave for the formation of phenylhydroxylamine for each of the nitrophenols is slightly shifted depending on the molecular structure. As discussed in Chapter 4, the diamond/quartz OTE is quite stable during cathodic polarization, while the

ITO/quartz OTE is not. Therefore, detecting these analytes electrochemically with ITO would be fraught with difficulty.

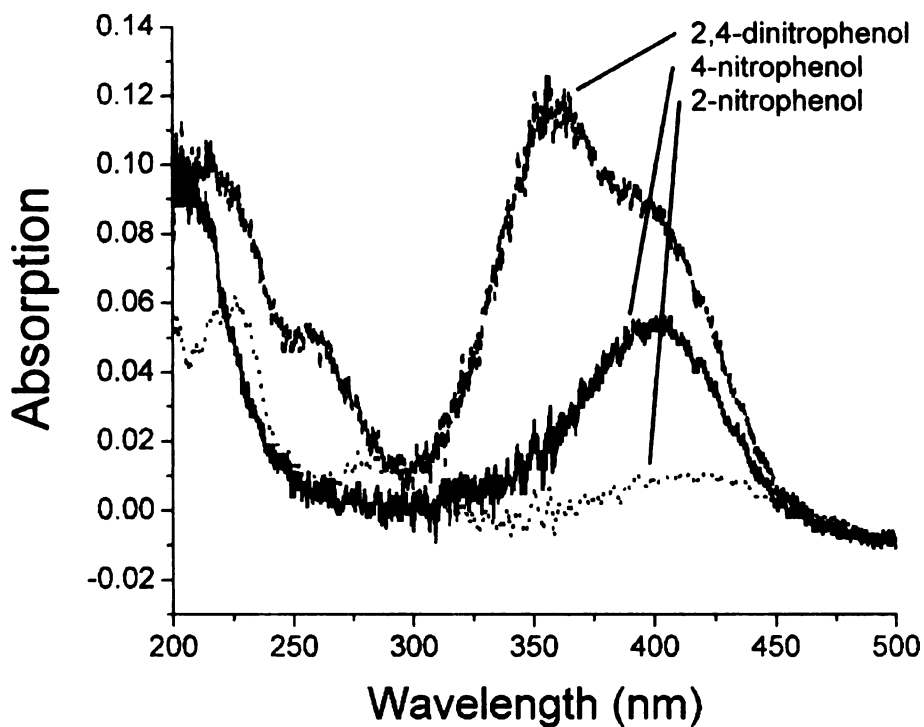


Figure 5-4. UV-Vis absorption spectra for 0.05 mM solutions of 2-nitrophenol, 4-nitrophenol, and 2,4-dinitrophenol in 10 mM phosphate buffer, pH 8.0.

In addition to the differences in the reduction peak potentials, differences in the absorption spectra of these molecules in the UV-vis region of the electromagnetic spectrum must also exist in order for a spectroelectrochemical measurement to provide any level of qualitative information. Figure 5-4 shows UV-Vis spectra for 2-nitrophenol, 4-nitrophenol, and 2,4-dinitrophenol. It can be seen that differences exist in the spectral features for each in the 200-500 nm

region. For example, both 2- and 4-nitrophenol have an absorption band attributed to a $\pi \rightarrow \pi^*$ transition of the aromatic ring (in the range from 250 to 350 nm), however, the λ_{max} shifts depending on the substituent group and position on the ring. The band is centered at ca. 280 nm for 2-nitrophenol and red shifted to ca. 320 nm for 4-nitrophenol. A band centered at ca. 350 nm is observed for 2,4-dinitrophenol, which may also be a $\pi \rightarrow \pi^*$ transition, is further red-shifted by the second nitro group.¹⁰⁸ A band centered at 260 nm is observed for 2,4-dinitrophenol, but not for either 2-nitrophenol or 4-nitrophenol. As discussed in Chapter 4, the diamond/quartz OTE possesses an optical window allowing spectroelectrochemical studies in the 200-300 nm region. The ITO/quartz OTE does not transmit light in this wavelength range. Detailed study of the difference UV-Vis absorption spectra for the compounds, a function of the redox state, is left for future study.

As discussed in Chapter 5, the optical, electric, and electrochemical properties of the diamond/quartz OTE are exceptionally stable during anodic and cathodic polarization in strongly acidic and alkaline media, as well as during exposure to different organic solvents. An example of a spectroelectrochemical detection method for environmental contaminants in a harsh chemical environment is the detection of ferricyanide in waste storage tanks at the Hanford Nuclear Storage Facility by Heineman, et al.¹⁰⁹ A spectroelectrochemical sensor constructed with an ITO/quartz OTE coated with a selective sol-gel was designed for insertion into waste storage tanks with the goal of determining the

concentration of ferricyanide present. However, the analysis suffered from changing background optical signals, which was attributed to dissolution of the ITO/quartz in the harsh chemical environment.¹¹⁰ A similar device constructed with the diamond/quartz OTE would be expected to perform reproducibly for significantly longer periods without signal degradation.

In the development of a spectroelectrochemical detection method for nitroaromatics, it is necessary to understand redox reaction kinetics and mechanisms at diamond. For example, is adsorption involved in the electrode reaction mechanism and how might the adsorption affect the electrochemical and optical signals? The research described herein represents our group's first effort to study the electrochemistry of the nitroaromatics (nitrophenol model compounds) at diamond. The existing body of literature on the electrochemistry of nitrobenzene at Hg, GC and Au electrodes served as a starting point. Given the toxicity of nitrotoluenes, we opted to perform these preliminary studies using the less dangerous nitrophenols. Nitrophenols are themselves EPA priority pollutants, but also serve as good model compounds for the nitrotoluenes in terms of their electrochemical behavior. The compounds studied were 4-nitrophenol, 2-nitrophenol and 2,4-dinitrophenol. The electrochemistry of 4-nitrophenol was also investigated as a function of pH and scan rate. The measurements were made using microcrystalline diamond deposited on Si, not quartz.

5.2 Experimental

Microcrystalline Boron-Doped Diamond Electrodes. The microcrystalline films were deposited on p-type Si(100) substrates ($\leq 10^{-3} \Omega\text{-cm}$, Virginia Semiconductor Inc., Fredricksburg, VA) in a commercial microwave CVD system (Astex, Woburn, MA). The surface of the Si substrate was mechanically scratched with 0-2 μm diameter diamond powder (GE Superabrasives, Worthington, OH), rinsed in 2-propanol and DI water, and then ultrasonicated in acetone. 1 kW of microwave power was used to sustain a plasma discharge from the source gases, hydrogen with 0.5% methane serving as a carbon source for diamond growth. The system was maintained at a pressure of 45 Torr with a total gas flow of 200 sccm. The substrate temperature (estimated by optical pyrometry) was 825°C. Ultrahigh purity (99.999%) methane and hydrogen were used as the source gases. B_2H_6 diluted in H_2 was introduced into the source gas mixture as a gas-phase source of boron. A B_2H_6 concentration of 10 ppm was used during the growth. After 10 hours of deposition, the methane and B_2H_6 flows were stopped, and the films remained subjected to an H_2 plasma for 10 min to ensure a hydrogen-terminated surface. After hydrogen plasma treatment, the films were cooled in the presence of atomic hydrogen to an estimated temperature of less than 300°C by slowly reducing the power and pressure over a 4 min period. This treatment removes adventitious nondiamond sp^2 carbon impurity, ensures full hydrogen surface termination, and prevents the surface from rearranging into π bonds. The film thickness was nominally 5 μm , and the

boron dopant concentration was in the low to mid 10^{20} cm^{-3} range, as determined from boron nuclear reaction analysis measurements of other films deposited using similar conditions. The film resistivity was ~ 0.01 $\Omega\text{-cm}$, or less, as measured with a tungsten four-point probe.

Nanocrystalline Boron-Doped Diamond Electrodes. The boron-doped nanocrystalline diamond thin-films were deposited on p-type Si(100) using the same microwave CVD system. The surface of the Si substrate was mechanically scratched with 0.1 μm diameter diamond powder (GE Superabrasives, Worthington, OH). The scratched substrate was then ultrasonicated in ultrapure water, isopropyl alcohol (IPA), and acetone to remove polishing debris. Ultrahigh purity CH_4 , Ar, and H_2 (99.999%) were used as the source gases at flow rates of 1, 94, and 5 sccm, respectively. B_2H_6 was used as the source gas for doping at a concentration of 10 ppm. The microwave power and system pressure were maintained at 800 W and 140 Torr, respectively. The substrate temperature was estimated by an optical pyrometer to be about 800°C . The deposition time was 2 h, giving approximately a 4 μm -thick film, as estimated from sample weight change. After deposition, the methane and B_2H_6 flow was stopped, and the films were subjected to an H_2 plasma for 10 min to ensure a hydrogen-terminated surface. The resistivity was 0.1 $\Omega\text{-cm}$ or less, as determined using the four-point probe method.

Glassy Carbon Electrodes. Tokai GC-20 (Tokai, Ltd.) was cut into ca. 1×1 cm^2

pieces and manually polished in alumina/water slurry. The electrode was polished using deagglomerated alumina powders in the order of 0.3, 0.1, and 0.05 μm (Buelher, Lake Bluff, IL) on a felt polishing pad (Buelher, Lake Bluff, IL). following each polishing step, the electrode was rinsed under a stream of ultrapure water and ultrasonicated in ultrapure water to remove polishing debris. After the final polishing and ultrasonication step, the electrode was rinsed with distilled 2-propanol, dried under an N_2 stream, and immediately mounted in the electrochemical cell. Following electrochemical measurements, the electrodes were rinsed with distilled 2-propanol, dried under an N_2 stream, and stored under ultrapure water.

Electrochemical Measurements. Electrochemical measurements were performed using a computer-controlled potentiostat (Model 1200, Cypress Systems, Inc., Lawrence, KS) in a standard, three-electrode configuration.⁶³ No IR correction was used in any of the reported measurements. The electrodes were clamped to the bottom of a single compartment, glass electrochemical cell. A Viton o-ring (i.d. 0.5 cm), placed between the cell opening and the electrode surface, ensured that a reproducible area of 0.2 cm^2 was exposed to electrolyte solution. Contact was made to the diamond electrode by pressing a piece of nickel foil against the entire film surface outside the o-ring. A neoprene rubber spacer was cut to the same dimensions as the nickel foil and used to force the foil into contact with the electrode surface. Contact was made to the GC on the backside with a copper plate current collector. The o-ring was sonicated for

10 min in ultrapure water, rinsed with distilled 2-propanol, and dried under a stream of N₂ before use. Diamond electrodes were soaked for 10 min in warm, distilled 2-propanol and dried under a stream of N₂ before use. Once mounted in the cell, the diamond or GC electrode was soaked in distilled 2-propanol for 20 min as a final surface cleaning step.¹¹¹ The cell was then rinsed thoroughly with distilled water and filled with the electrolyte solution of interest. N₂ was bubbled through the solution for 10 min to remove dissolved oxygen, and the solution was blanketed with the gas during the measurements. The counter electrode was a large-area carbon rod, which was cleaned before use by rinsing with liberal amounts of distilled 2-propanol and dried with laboratory tissue. The counter electrode was positioned normal to the working electrode. The reference electrode was a commercial Ag/AgCl electrode filled with 4 M KCl. The reference electrode was placed in a cracked-glass capillary filled with the supporting electrolyte. The end of the capillary extended to just above the surface of the working electrode in order to most accurately sample the potential drop at the working electrode. To prevent carry-over of nitrobenzene and nitrophenols from one measurement to the next, the assembled cell (glass cell, o-ring, working electrode, counter electrode and reference electrode capillary) was rinsed with methanol, and then with distilled 2-propanol between solution fillings.

UV-Vis Measurements: UV-vis absorption spectra were recorded for 2-nitrophenol, 4-nitrophenol, and 2,4-dinitrophenol solutions in 10 mM phosphate

buffer, pH 8, using a dual-beam Shimadzu UV-2401 PC spectrophotometer (Shimadzu Corp., Columbia, MD). A slit width of 0.5 nm and a 210 nm/sec monochromator scan rate were used along with a matched pair of quartz cuvettes with a pathlength of 1 cm. The cuvettes were rinsed three times with methanol (Aldrich, HPLC grade) and dried with an N₂ stream prior to a measurement. After allowing the instrument lamps to warm up for 30 min, a background spectrum was recorded from 200 to 900 nm with the cuvettes filled with buffer solution in both beam paths. This spectrum was automatically subtracted from all analyte spectra. Between measurements, the cuvettes were cleaned using the same methanol rinse and N₂ drying procedure.

Chemicals. 10 mM phosphate buffer was prepared by mixing 10 mM solutions of H₃PO₄ (Aldrich, 99.999%), NaH₂PO₄ · H₂O (Spectrum, ACS) and Na₂HPO₄ · 7H₂O (Spectrum, ACS) to achieve solution of desired pH. 4-nitrophenol (Alfa Aesar, 97%), 2-nitrophenol (Avocado Research Chemicals, 98%), 2,4-dinitrophenol (Lancaster Synthesis, 98%), and 4-nitrocatechol (Aldrich, 99.999%), methanol (HPLC), and KCl (Spectrum, ACS) were used as received. 0.1 mM stock solutions of all three nitrophenols were prepared and stored indefinitely. Phosphate buffer solutions were prepared daily to prevent bacterial growth. 1 M KCl (Spectrum, ACS) was prepared weekly. Fresh 1 mM Fe(CN)₆^{-3/-4} (Aldrich, 98%) in 1 M KCl for testing the polish quality of GC was prepared fresh daily. All solutions were prepared using 18 MΩ-cm ultrapure water from a Barnstead E-pure water purification system. 2-propanol (CCI, ACS) was distilled after storing

over activated carbon for at least one week, and filtering to remove carbon from the solvent. After distillation, 2-propanol was stored in glass.

Safety note: nitrophenols are potent toxins, causing liver and kidney damage. They are readily absorbed through the skin and permeate through latex and nitrile gloves. All work with nitrophenols must be done wearing viton rubber gloves and appropriate face protection. The nitrophenols have a vapor pressure, so all work should be done within a fume hood to prevent their inhalation.

5.3 Results and Discussion

Cyclic Voltammetry of 4-nitrophenol at Glassy Carbon. In order to determine whether the nitro group on 4-nitrophenol undergoes redox chemistry similar to that reported by Rubinstein for nitrobenzene, cyclic voltammetric i-E curves for 4-nitrophenol compound were measured at glassy carbon (GC). In 10 mM phosphate buffer solution, pH 8, the i-E curve is similar similar to that reported by Rubenstein for nitrobenzene (pH 6).¹⁰⁷ The cyclic voltammetric i-E curve (first scan) is presented in Figure 5-5A. Starting at -0.5 V, the potential is first swept positive to 0.5 V. A small anodic current is observed at 0 V, due to phenylhydroxylamine left in solution near the electrode surface from the preceding measurements, which was not fully removed by agitation with N₂. When the potential is then swept negative, no current above the background is observed until -700 mV at which point a cathodic peak forms at ca. -800 mV. The peak current is consistent with $n = 2$ for the given nitrophenol concentration,

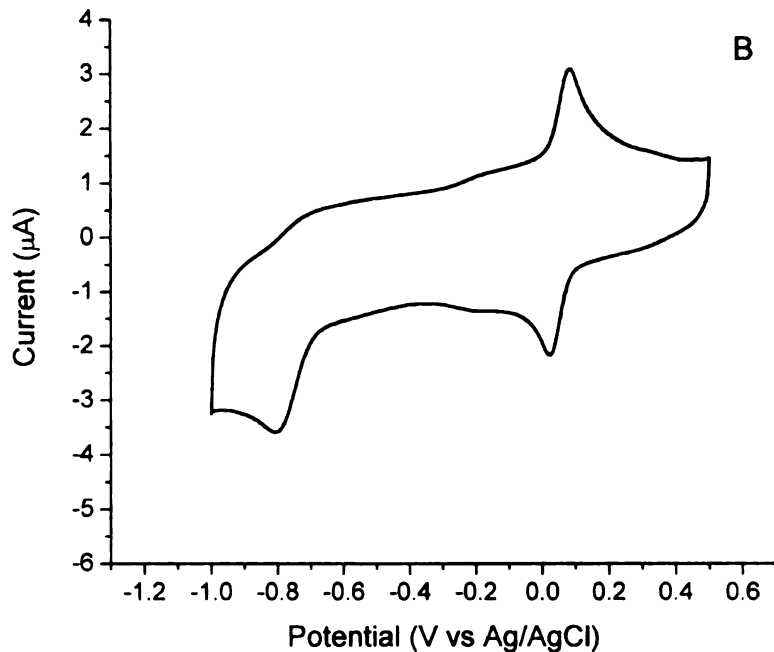
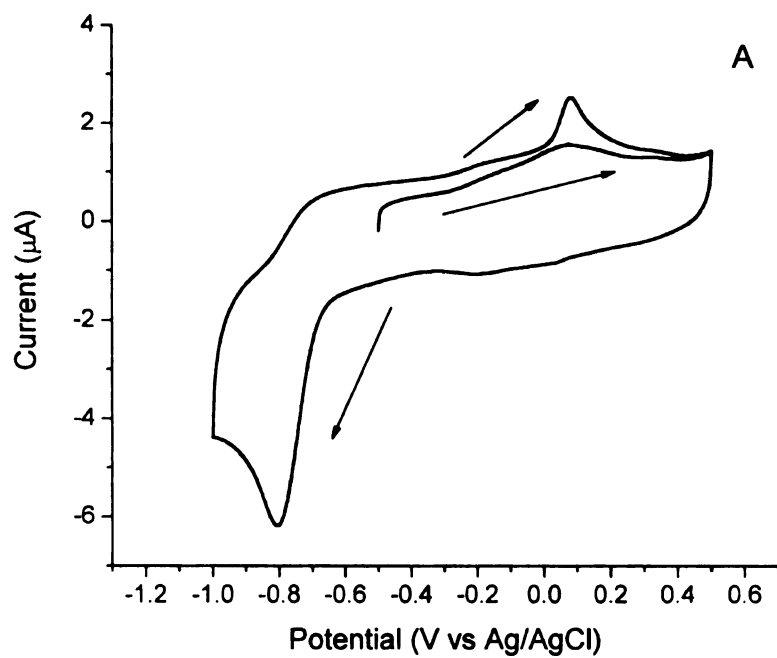


Figure 5-5. Cyclic voltammetric i-E curves for 0.05 mM 4-nitrophenol in 10 mM phosphate buffer, pH 8.0 at a polished, planar glassy carbon electrode. (A) First cycle following bubbling with N₂, (B) tenth cycle (features unchanging with cycle number). Scan rate=50 mV/sec.

an electrode area of 0.2 cm^2 , and a diffusion coefficient of $7.9 \times 10^{-6} \text{ cm}^2/\text{s}$.¹¹² In the following discussion, this will be referred to as peak A. This peak is presumably associated with the formation of the hydroxylamine.

When the potential is swept positive from the negative limit of -1.0 V , an anodic current feature is observed at ca. 100 mV , which we suppose corresponds to the oxidation of the hydroxylamine to nitrosophenol. This will be referred to as peak B. After repeated cycling of the potential between 0.5 and -1 V , an unchanging cyclic voltammetric i - E curve was obtained, and is presented in Figure 5-5B. The term “unchanging” means that the cyclic voltammetric i - E curve shape did not change with cycle number. The shape of the curve for the tenth scan looks similar to the first scan, except that when the potential is swept negative from 0.5 V , a new cathodic wave is observed at ca. 0.05 V , corresponding to the reduction of nitrosophenol to the hydroxylamine. This will be referred to as Peak C. Peaks B and C are associated with the same redox reaction and they are observed if the potential is scanned between -400 and -500 mV . However, they are not observed unless the potential cycle initially extends more negative to -1000 mV . This indicates they correspond to a product of the large reduction wave (Peak A). The peak potential for Peak A is shifted from ca. -650 mV for nitrobenzene at pH 6 in Rubenstein’s work to ca. -800 mV at pH 8 in the current work.¹⁰⁷ This 150 mV shift is close to the expected shift for a reaction involving a balanced number of electrons and protons, ($-60 \text{ mV}/\text{pH}$). As reported for nitrobenzene at GC, the Peak A current decreases with cycle number to a

stable value. The curve shape and appearance of the redox couple centered at 0.1 V suggests that the nitro group redox chemistry on nitrophenol proceeds through a similar mechanism at GC as does nitrobenzene. These results indicate that the nitro group redox chemistry for 4-nitrophenol is similar to that for nitrobenzene. Therefore, the nitrophenols are useful model compounds to start with, leading to the eventual study of nitrotoluenes.

The smaller than expected peak currents indicate a lower sensitivity for 4-nitrophenol at GC than nitrobenzene. We did not investigate this in any detail, but there are several possible reasons for this. One is the nature of the surface produced by pretreatment. Careful surface polishing procedures used in this research have been shown to reduce the amount of surface oxides.¹¹³ Rubinstein reported a lack of careful surface pretreatment in his work with nitrobenzene at GC as a possible reason for the larger ΔE_p observed for nitrobenzene at GC than at Au.¹⁰⁷ Vasquez et al. showed that an oxidative electrochemically pretreated electrode (more carbon-oxygen functionalities) showed greater than a three-fold increase in the reduction current for 4-nitrotoluene, as compared to a carefully polished electrode (a lower surface oxide content).¹¹⁴ More reversible kinetics for the redox couple (Peaks B and C) are observed in the present work than for nitrobenzene reported at GC by Rubinstein. The ΔE_p is 156 mV compared to ca. 200 mV at 100 mV/sec for nitrobenzene. This difference in redox reaction kinetics, as assessed from the ΔE_p values, is possible evidence for a difference in surface chemistry.

A Comparison of 4-nitrophenol, 2-nitrophenol, and 2,4-dinitrophenol Cyclic Voltammetry. With evidence that 4-nitrophenol behaves in a similar manner as nitrobenzene at GC, at least in terms of the peak positions, we next investigated the redox chemistry of the model nitrophenols at boron-doped diamond. A series of cyclic voltammetric i-E curve for 0.055 mM 4-nitrophenol in 10 mM phosphate buffer, pH 8,

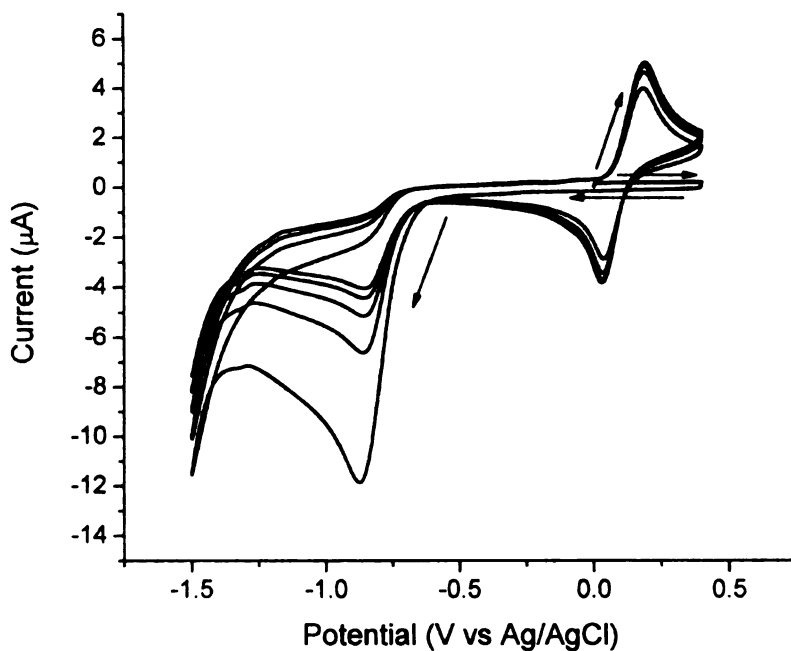


Figure 5-6. Cyclic voltammetric i-E curve for 0.055 mM 4-nitrophenol in 10 mM phosphate buffer, pH 8.0, at a planar, microcrystalline diamond electrode. Scan rate=50 mV/sec.

measured at 50 mV/s at a microcrystalline diamond electrode are presented in Figure 5-6. The potential sweep began at 0 V, with the initial scan in the positive direction to +0.4 V. Little current above the background is seen on the forward

sweep. During the reverse sweep, the curve is featureless until -0.75 V at which point cathodic current begins to flow. A reduction is observed with a peak current of ca. -0.88 V (Peak A). Additional cathodic current flows at -1.5 V at which point the potential sweep is reversed. On the positive going sweep, an anodic peak is observed at ca +0.3 V (Peak B). On subsequent cycles, a related cathodic peak is observed at ca. +0.1 V (Peak C). As observed for this compound at GC, the peak current for Peak A decreases with cycle number toward a constant value of ca. -4 μ A (a decrease of ca. 66%). The curve shape and relationship between the three peaks closely resembles that seen for 4-nitrophenol at GC. ΔE_p for the redox couple centered at 0 V is 199 mV, which is larger than 156 mV, the value observed at GC. Based solely on the similarity in the curve shapes, it is supposed that Peak A corresponds to the reduction of 4-nitrophenol to the phenylhydroxylamine. The similar curve shapes also indicate that Peaks B and C are associated with the reversible oxidation of the phenylhydroxylamine to nitrosophenol, and the reduction of nitrosophenol to the phenylhydroxylamine, respectively. The peak potentials and currents for these three peaks during the first cycle are presented in Table 5-1.

As shown in Table 5-1, the current for all three peaks at microcrystalline diamond electrodes is less than the theoretically predicted values. The theoretical values were calculated using the following equation:

$$i_p = 2.69 \times 10^5 \times n^{3/2} \times A \times D^{1/2} \times v^{1/2} \times C$$

where n is the number of electrons passed, A is the electrode area in cm^2 , D is the diffusion coefficient of the analyte molecule in cm^2/sec , v is the scan rate in V/sec , and C is the concentration of the analyte in mol/cm^3 . This calculation employs three assumptions: (i) the electrochemically active electrode area is equal to the geometric area (0.2 cm^2), (ii) the redox reaction rate is limited by semi-infinite linear diffusion with no effect of adsorption, and (iii) four electrons are passed for the reaction in Peak A, and two electrons are passed for the reactions in Peaks B and C. The observed peak currents for all three peaks are lower than the theoretically predicted values. For example, the predicted peak current for Peak A is $-15 \mu\text{A}$, while the observed peak current is $-11 \mu\text{A}$. The disagreement between the theoretical and observed peak currents on the first cycle indicates that one of these three assumptions is invalid.

Recent results have shown that the conductivity profile is inhomogeneous across the surface of microcrystalline diamond electrodes grown under the same conditions as those used in this research.^{37, 71} This suggests that assumption (i) may not be valid. The electrochemically active electrode area should be carefully determined by cyclic voltammetric or chronoamperometric measurements of well-defined redox systems at these electrodes in order to test this assumption. An electrochemically active area that is smaller than the nominal electrode area would account for the discrepancy between theoretical and observed peak current magnitudes for 4-nitrophenol.

Table 5-1. Cyclic voltammetric peak currents and peak potentials for 4-nitrophenol, 2-nitrophenol, and 2,4-dinitrophenol at a microcrystalline diamond electrode in 10 mM phosphate buffer, pH = 8.0. For 2-nitrophenol and 4-nitrophenol, values are reported for first cycle voltammetric curves. For 2,4-dinitrophenol, values are reported for unchanging voltammetric curves. Case 1 refers to peaks corresponding to 4-nitrophenol, and Case 2 refers to peaks corresponding to 2-nitrophenol. Theoretical peak current values were calculated using an analyte concentration of 0.05 mM, a diffusion coefficient of 9.19×10^{-6} cm²/sec, and the number of electrons as noted.

	Peak A	Peak B	Peak C
Theoretical Peak Current	-15 (μ A) (assuming n = 4)	5.2 (μ A) (assuming n = 2)	-5.2 (μ A) (assuming n = 2)
4-nitrophenol	$i_p^{ox} = -11$ (μ A) $E_p^{ox} = -876$ (mV)	$i_p^{ox} = 4.6$ (μ A) $E_p^{ox} = 155$ (mV)	$i_p^{ox} = -4.0$ (μ A) $E_p^{ox} = -44$ (mV)
2-nitrophenol	$i_p^{ox} = -5.2$ (μ A) $E_p^{ox} = -755$ (mV)	$i_p^{ox} = 0.39$ (μ A) $E_p^{ox} = 263$ (mV)	$i_p^{ox} = -0.11$ (μ A) $E_p^{ox} = -364$ (mV)
2,4- dinitrophenol (case 1)	$i_p^{ox} = -4.0$ (μ A) $E_p^{ox} = -881$ (mV)	$i_p^{ox} = 2.7$ (μ A) $E_p^{ox} = -57$ (mV)	$i_p^{ox} = -2.6$ (μ A) $E_p^{ox} = -116$ (mV)
2,4- dinitrophenol (case 2)	$i_p^{ox} = -3.0$ (μ A) $E_p^{ox} = -714$ (mV)	$i_p^{ox} = 0.44$ (μ A) $E_p^{ox} = 344$ (mV)	$i_p^{ox} = -0.34$ (μ A) $E_p^{ox} = -328$ (mV)

A similar cyclic voltammetric investigation was carried out for 2-nitrophenol. In Figure 5-7, the corresponding cyclic voltammetric i-E curve is presented. When the potential is swept from 0 to +0.5 V, no current above

background is observed. When the potential is swept negative from +0.5 V, no current above background is observed until the onset of cathodic current at ca. -0.4 V. The cathodic current peaks at -0.75 V (peak A). A new oxidation wave is observed on the subsequent positive sweep from -1.1 V, centered at ca. +0.3 V (peak B). As in the case of 4-nitrophenol, this peak is linked to the large reduction peak at ca. -0.8 V because it is not observed until Peak A is observed. When the potential is swept negative on subsequent cycles, a new cathodic current feature is observed at ca. -0.4 V. Like Peak C in the 4-nitrophenol voltammetric curve, Peak C is not observed until after Peak B is observed, indicating that Peak C corresponds to the reduction of a product of the reaction at Peak B.

The peak currents for the three peaks during the first cycle 2-nitrophenol voltammetric curve are significantly less than those predicted by theory for $n = 4$ (Peak A) or $n = 2$ (Peaks B and C). It is possible that the reactions at these peaks proceed by a different reaction mechanism than 4-nitrophenol. No measurements have been made to determine what reaction is occurring at the peaks in this voltammetric curve. However, the cleaning procedure used between measurements resulted in reproducible background voltammetric curves with no evidence of fouling by previously measured analytes. In order to accurately determine the reaction occurring at each peak, it is necessary to determine the number of electrons passed at the peaks. Measurements at a rotating disk electrode following careful determination of the active electrode area

by measurements with a well-defined redox system would provide this information.

Presented in Figure 5-8A are cyclic voltammetric i-E curves for a 0.05 mM solution of 2,4-dinitrophenol in 10 mM phosphate buffer, pH = 8.0, at a planar microcrystalline diamond electrode. Like 2- and 4-nitrophenol, no current features are observed when the potential is swept negative from +150 to -200 mV on the first cycle. As the potential is swept negative to -1200 mV, a cathodic current begins to flow at -650 mV, with peaks at ca. -720 mV and ca. -900 mV.

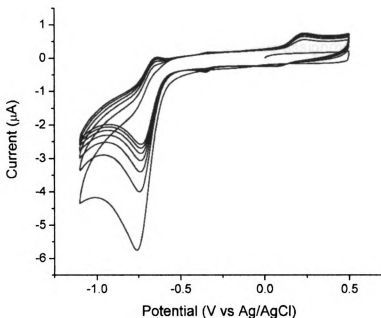


Figure 5-7. Steady state cyclic voltammetric i-E curve for 0.05 mM 2-nitrophenol in 10 mM phosphate buffer, pH 8.0 at planar, microcrystalline diamond electrode. Scan Rate = 50 mV/sec.

Both peaks decrease in current to a steady state value with cycle number. The

peak at -900 mV will be referred to as peak A, case 1, and the peak at -720 mV will be referred to as peak A, case 2. As shown in Table 5-1, the peak potentials for case 1 correlate with those for 4-nitrophenol, and the peak currents and peak potentials for case 2 correlate with those for 2-nitrophenol. Because the voltammetric curves presented represent the unchanging curve after several cycles (not the first cycle), no relationship between the peak currents for 2,4-dinitrophenol and the two former nitrophenols presented can be made. It is possible that Peak A, cases 1 and 2, represent the current for reduction of the two nitro groups on the molecule to the corresponding phenylhydroxylamines. Hilmi *et al.* reported three reduction waves for trinitrotoluene at glassy carbon electrodes in pH 8.7 borate buffer containing 5 mM SDS, attributing each wave to reduction of one nitro group.¹¹⁵ However, no clear assignment can be made until the number of electrons passed at each peak is determined by a measurement such as voltammetric *i*-*E* curves measured with a diamond rotating disk electrode with a carefully determined electrochemically active area.

On the positive sweep from -1200 to +150 mV in Figure 5-8, anodic waves are observed with peaks at ca. -350 mV and -50 mV. The peak at -50 mV may correspond to the oxidation of the para hydroxylamine group to a nitroso group (peak B, case 1). This peak is observed only after the peaks assigned as Peak A, cases 1 and 2, are observed. However, the peak potential for Peak B, case 1, is not close to that observed for Peak B in the 4-nitrophenol voltammetric curve (-57 mV for 2,4-dinitrophenol and 155 mV for 4-nitrophenol). Three new cathodic

peaks are observed on subsequent cycles, at -116, -350 and -400 mV. The feature at -116 mV is not observed until after Peak B, case 1 is observed, indicating that it represents the oxidation of the product of the reaction at Peak B, case 1. It is therefore tentatively assigned to the reduction of the 4-nitroso group, and referred to as Peak C, case 1. The E_p for this peak is not close to that observed for Peak C for 4-nitrophenol, as noted in Table 5-1 (-166 mV for 2,4-dinitrophenol and -44 mV for 4-nitrophenol). Therefore, clear assignment of this peak cannot be made until the number of electrons passed has been determined. The reaction represented by the other two peaks near -350 mV is the subject of further investigation. The anodic feature at -350 mV and cathodic feature at -400 mV persist when the solution is replaced with fresh buffer solution, and increase in peak current magnitude with increasing cycle number, as noted with the horizontal arrow in Figure 5-8A. This evidence indicates that these peaks are likely related to a surface-confined redox system.

In Figure 5-8B, the unchanging voltammetric curve for 2,4-dinitrophenol at microcrystalline diamond is plotted on the same axes as the unchanging voltammetric curve collected when the potential is swept further positive, to +500 mV (dashed line). When the potential is swept to +500 mV, an anodic peak is observed at +344 mV and the cathodic peak at ca. -300 mV has a larger peak current. The new anodic peak current and potential are close to those observed for the oxidation of the hydroxylamine to the nitroso group, as observed for 2-nitrophenol, therefore, it is referred to as peak B, case 2. As shown in Table 1,

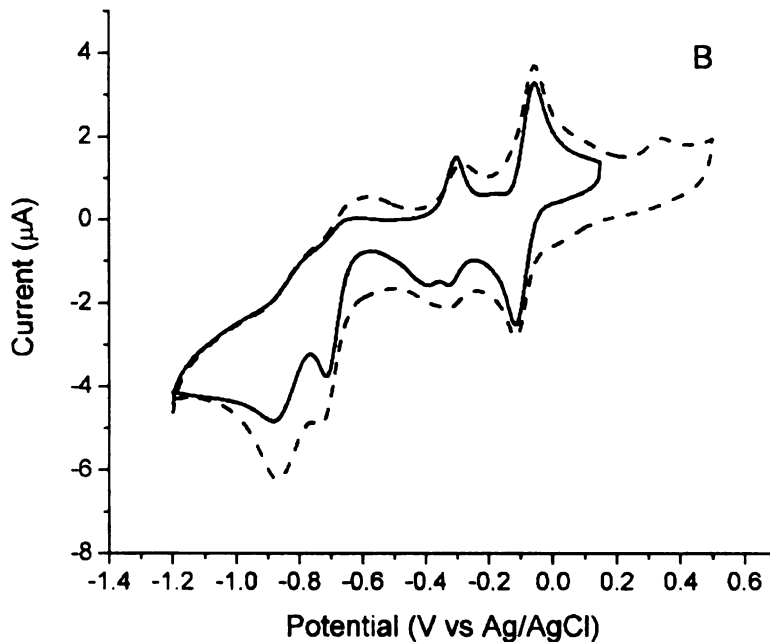
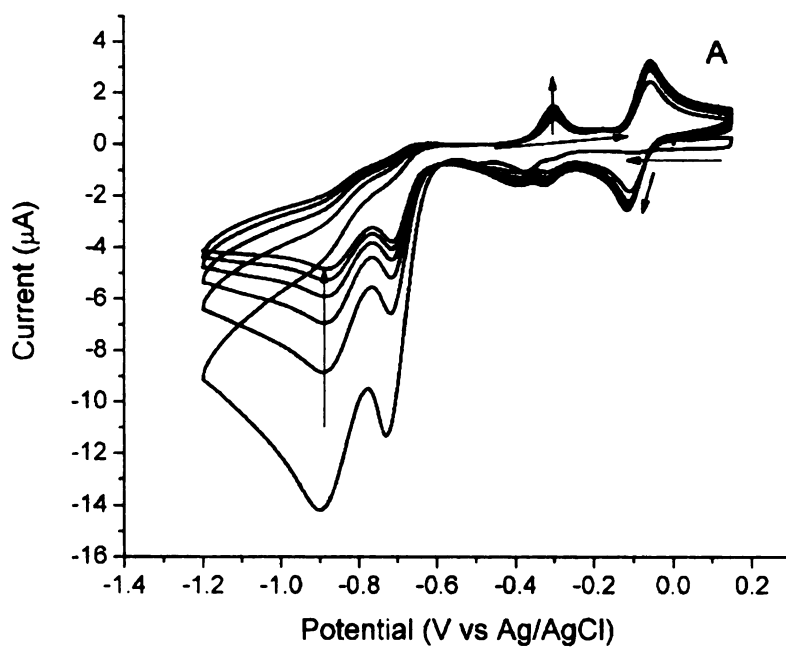


Figure 5-8. Cyclic voltammetric i-E curves for 0.05 mM 2,4-dinitrophenol in 10 mM phosphate buffer, pH 8.0, at a microcrystalline diamond electrode. Steady state curves are presented in (B). Scan rate = 50 mV/sec.

the E_p for Peak B, case c, (344 mV) is relatively close to that for the tentatively assigned nitrosophenol formation peak of 2-nitrophenol at this electrode (263 mV). The cathodic feature at -300 mV may represent current produced by both a surface confined reduction reaction discussed above and the reduction of the 2-nitroso group created at +344 mV. This peak is therefore referred to as peak C, case 2.

In summary, the voltammetric i-E curve for 4-nitrophenol measured at microcrystalline diamond have the same shape as those for 4-nitrophenol and nitrobenzene at GC, with peaks at slightly different potentials. Therefore, it seems that the peaks in the voltammetric i-E curve refer to the reduction of 4-nitrophenol to hydroxyphenylamine (Peak A), the oxidation of the hydroxyphenylamine to nitrosophenol (Peak B), and the reduction of nitrosophenol to the hydroxyphenylamine (Peak C), respectively. However, the peak current magnitudes at all three peaks at diamond are less than theoretically predicted, indicating that the assumptions made in the theoretical calculations must be tested. The voltammetric i-E curve for 2-nitrophenol has a similar shape, but with a significantly lower peak current magnitudes observed for Peaks A, B, and C. The reason for the low peak currents is not clear, but it is possible that the reaction mechanism is different for 2-nitrosophenol than 4-nitrosophenol at diamond. The voltammetry of 2,4-dinitrophenol at diamond can be described as a combination of peaks observed for 2- and 4-nitrophenol. First, irreversible

nitro group reduction peaks are observed at ca. -750 and -875 mV and are tentatively attributed to the reduction of two nitro groups in the molecule based on peak potentials. Second, a relatively reversible redox couple was observed near -100 mV, tentatively assigned to the nitro group located para to the phenol group (4-nitrophenol), as well as a quasi-reversible couple corresponding to the nitro group located ortho to the phenol group (2-nitrophenol). Overpotentials for the reactions responsible for these features are different than those for the singly nitrated phenols. As in the case of 2-nitrophenol, clear assignment of the reactions at each peak cannot be made until a careful determination of the

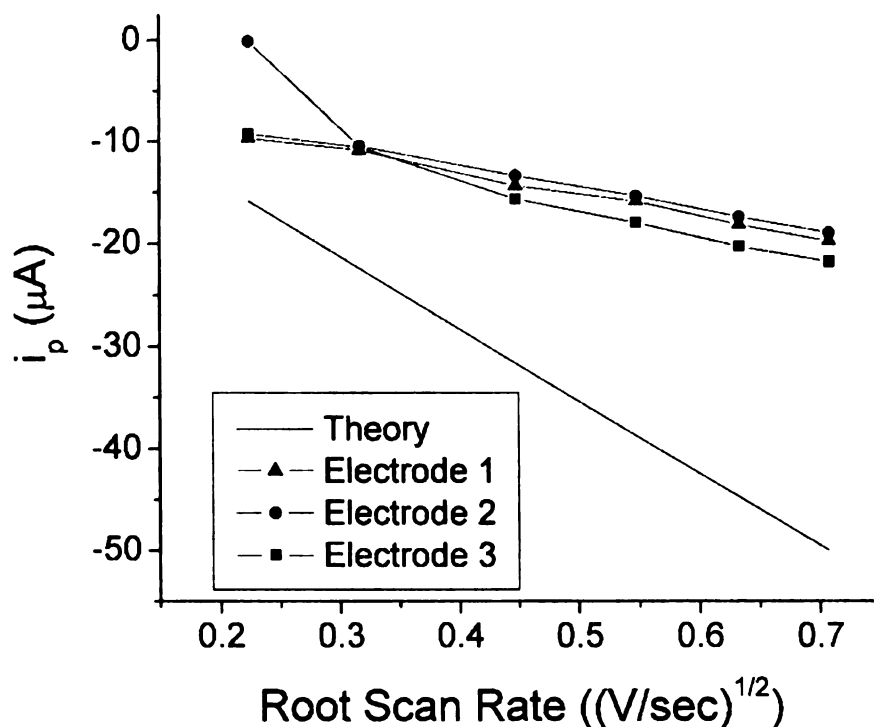


Figure 5-9. i_p values for 4-nitrophenol Peak A (first cycle) at three diamond electrodes and theoretically predicted i_p values plotted vs the square root of scan rate. 0.05 mM 4-nitrophenol in 10 mM phosphate buffer solution, pH 6.0.

number of electrons passed at each peak has been made.

4-nitrophenol pH and Scan Rate Studies. In an attempt to determine the number of electrons passed during the redox reaction of 4-nitrophenol at Peak A, peak currents were measured from cyclic voltammetric *i*-*E* curves collected at scan rates from 50 to 500 mV/sec in 10 mM phosphate buffer solution, pH 6.0, at three different diamond electrodes. Because the peak currents of this peak decay significantly with cycle number, the first cycles measured at each electrode were used. Shown in Figure 5-9 are i_p plotted vs the square root of scan rate, as well as the theoretically predicted i_p values. Theoretical peak currents at the same scan rates were calculated using the equation for i_p as above, using an assumed electrode area of 0.2 cm², a concentration of 0.05 mM, and a diffusion coefficient of 9.19x10⁻⁶ cm²/sec.¹¹² As shown in Figure 5-9, the peak current value for Electrode 2 at the lowest scan rate was erroneously low. Therefore, this data point was excluded from calculation of the linear correlation coefficient and line of best fit for the peak currents at Electrode 2. The correlation coefficients and slopes for lines of best-fit at all three electrodes are presented in Table 5-2. Also presented in Table 5-2 is the slope of the line of best-fit for theoretically predicted i_p values. However, the slopes of lines of best-fit are more than a factor of two lower than that predicted by theory. It is clear that one or more of the assumptions employed in making the prediction may be invalid. The linear dependence of the current with the square root of scan rate indicates semi-infinite linear diffusion control of the Peak A current. Therefore, the

assumption of semi-infinite linear diffusion, with no contribution of adsorption, is valid. It is likely, as reported by Holt et al. for similar electrodes,³⁷ that the actual active electrode area for these reactants is significantly less (ca. 50%) than the geometric electrode area. If the assumption that the reaction at Peak A involves four electrons, the ca. 50% discrepancy between the electrochemically active area and the geometric area would account for the ca. factor of two difference between the experimental and theoretical slopes. A clear determination of the number of electrons passed at Peak A cannot be made without making a determination of the electrochemically active area of the electrodes used.

Table 5-2. Linear correlation coefficients and slopes of steady-state cyclic voltammetric peak currents vs square root of scan rate ($\mu\text{A}/(\text{V}/\text{s})^{1/2}$) for 0.05 mM 4-nitrophenol solutions in 10 mM phosphate buffer, pH = 8.0, at three microcrystalline diamond electrodes. Scan rate = 100 mV/sec.

<i>Theory</i>	<i>Electrode 1</i>	<i>Electrode 2</i>	<i>Electrode 3</i>
1	0.992	0.999	0.998
$-71 \mu\text{A}/(\text{V}/\text{s})^{1/2}$	$-21 \mu\text{A}/(\text{V}/\text{s})^{1/2}$	$-22 \mu\text{A}/(\text{V}/\text{s})^{1/2}$	$-27 \mu\text{A}/(\text{V}/\text{s})^{1/2}$

The large decrease in the slope for the four-electron wave from the first to steady state cycle voltammograms may indicate a poisoning or deactivation of surface sites for the nitrophenol reduction reaction. This behavior was demonstrated for nitrobenzene at GC by Rubinstein,¹⁰⁷ and at Hg by McIntire et al.,¹⁰⁶ but explained by neither.

To determine the effect of pH on the reaction of 4-nitrophenol at diamond,

cyclic voltammetric i-E curves of 4-nitrophenol were measured at several microcrystalline diamond electrodes in 10 mM phosphate buffer at pH = 5, 6, and 8, at 100 mV/sec. The resulting peak potentials for steady state voltammograms are presented in Table 5-3. As the proposed reduction and oxidation reactions of the nitro group require a balanced number of electrons and protons, all peaks are expected to shift 60 mV/pH unit. However, peak A does not shift in the pH range studied. Peak B shifts 15 mV/decade negative from pH 5 to 6, and 49 mV/decade negative from pH 6 to 8. Peak C shifts 49 mV/decade *positive* from pH 5 to 6, and 96 mV/decade negative from pH 6 to 8, nearly twice the 60 mV/decade expected. These results show no clear trend, and therefore, cannot be used to deduce the role of protons in the reactions at Peaks A, B, and C. One likely reason no trend is observed is the deprotonation of 4-nitrophenol between pH 6 and 8, at a pKa of 7.15. In order to make any conclusions about the role of protons in the redox mechanism of 4-nitrophenol at diamond, it is necessary to repeat the measurements at new pH values, both above and below the nitrophenol pKa. Cyclic voltammetric i-E curves must be measured over a wider pH range, with a separation of 0.5 or 1 pH unit. Measurements should be made from pH 2 to 5, and from pH 8 to 11. Comparing the shift in peak potentials for cyclic voltammetric i-E curves measured at this wider range of pH values would better allow the determination of (i) the role of protons in the reaction mechanism at diamond, and (ii) differences in the reaction mechanism between the protonated (pH 2 to 5) and deprotonated (pH 8 to 11) forms of the molecule.

Table 5-3. Steady state cyclic voltammetric peak potentials for 0.05 mM 4-nitrophenol solution in 10 mM phosphate buffer, pH = 5, 6, and 8 at diamond. Values are averaged for measurements at three electrodes. Scan rate = 100 mV/sec.

<i>pH</i>	<i>Peak A</i> (<i>steady state</i>) (<i>V</i>)	<i>Peak B</i> (<i>V</i>)	<i>Peak C</i> (<i>V</i>)
5	-880±0.0	301±9.5	73.3±5.9
6	-823±41	286±18	122±1.2
8	-886±0.0	188±2.1	-70.0±4.2

The role of phenol oxidation in the Electrochemistry of 4-nitrophenol, 2-nitrophenol, and 2,4-dinitrophenol. In the study of nitrophenols at diamond, phenol oxidation must be considered. The oxidation of phenol and phenolic compounds have been described at GC, Au, and Ag electrodes. The reaction was demonstrated by Gattrell and Kirk to proceed through production of a phenoxy radical, which may be oxidized through anodic oxygen transfer to hydroquinone or catechol species, or through self-polymerization to form polymers containing active phenol groups, or both.¹¹⁶⁻¹¹⁹ This reaction was demonstrated at several electrode materials to cause severe signal attenuation because of fouling. In fact, fouling of metal electrodes following phenol oxidation was reported as a means to electrochemically coat metals with protective polymer films.¹²⁰

Muna *et al.* have recently demonstrated the oxidation of chlorophenols at hydrogen terminated diamond,⁴³ and Terashima *et al* have reported oxidation at heavily oxidized diamond.¹²¹ In Muna's work, oxidation waves occurred at

potentials positive of +900 mV, near the onset of oxygen evolution, through anodic oxygen transfer. In this mechanism, the oxidation occurs by addition of a new hydroxyl group to the aromatic ring. Voltammetric and scanning probe microscopic evidence of polymeric deposition of quinone/hydroquinone species on the electrode surface was reported, to a far lesser extent than at GC or metal electrodes. While some deposition of polymer was observed, no phenol oxidation signal attenuation was reported at diamond in a flow injection cell. Deposits were removed by soaking in warm 2-propanol. Peak current for the presumed anodic oxygen transfer varied linearly with the root of scan rate, indicating control by semi-infinite linear diffusion. Rodrigo *et al.* have demonstrated phenol oxidation of nitrophenols at heavily oxidized polycrystalline diamond electrodes in a mechanistic study preceding electroremediation efforts.¹²² In their work, peaks were observed that closely resembled the nitro group electrochemistry demonstrated for nitrobenzene at GC by Rubinstein, but these features are attributed to a quinone/hydroquinone transition. This assignment seems questionable, as the work makes no reference to the existing body of work regarding the reduction electrochemistry of nitrobenzene.

Figure 5-10 presents cyclic voltammetric *i*-*E* curves of 0.05 mM 4-nitrophenol in 10 mM phosphate buffer solution, pH = 8.0. In the dashed trace of Figure 5-10, cycled between -0.4 and +0.4 V, no peaks are observed, confirming that the redox couple observed in this potential range is related to the products of the reduction to hydroxylamine as discussed above. In the dotted trace, cycled

between -0.6 and +1.2 V, the redox couple centered at +0.2 V is still not observed. As the potential does not extend more negative than -0.4 V in the dashed trace, the hydroxylamine is not produced. However, as the potential sweeps positive in the dotted trace, and anodic current begins to flow at +750 mV and peaks at +1.0 V. This peak is attributed to anodic oxygen transfer to the benzene ring, as observed for chlorophenols at diamond electrodes, possibly forming 4-nitrocatechol.⁴³

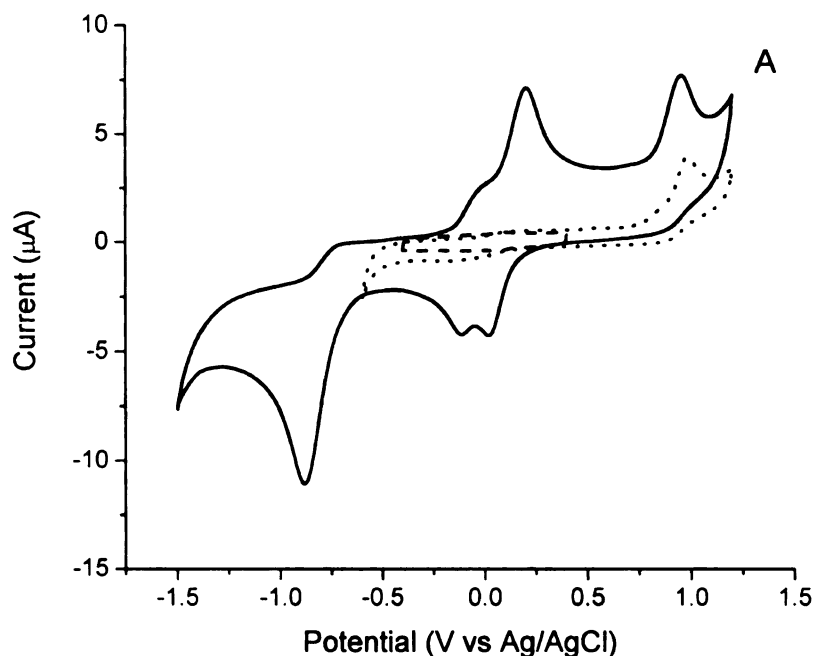


Figure 5-10. Cyclic voltammetric i-E curves for 0.05 mM 4-nitrophenol in 10 mM phosphate buffer, pH 8.0.

The solid trace in Figure 5-10 presents a cyclic voltammetric i-E curve with potential limits that include the reduction wave at -0.8 V and the oxidation wave

at +1.0 V. The nitro reduction peak and phenol oxidation peak are both observed, as is the redox couple centered at +0.2. However, two differences are observed when comparing this cyclic voltammetric i-E curve to that in Figure 5-6A. First, the peak currents for all three peaks observed in the steady state cycle of Figure 5-6 are roughly doubled in Figure 5-10. Second, two new current features are observed: a pair of peaks centered at 0 V, with a peak splitting of less than 60 mV, appearing as shoulders on the previously observed couple centered at +0.2 V. These peaks are not observed until after sweeping the potential through *both* the phenol oxidation *and* nitro reduction waves. It is therefore proposed that the nitro group on 4-nitrocatechol produced at the phenol oxidation wave can be reduced to a hydroxylamine species, as in the case of nitrophenol. It is further proposed that these peaks represent the oxidation of the hydroxylamine group on the catechol molecule and the reduction of this nitroso group back to hydroxylamine. The difference in nitro group overpotentials between phenol and catechol species may be explained by the influence of an additional hydroxyl group on the benzene ring. The increased current for the cathodic feature at -0.8 V may be explained by the combined reduction of the nitrophenol and nitrocatechol species. Evidence of phenol oxidation is also observed for 2- nitrophenol and 2,4-dinitrophenol.

To test the assignment of these features to nitrocatechol species, cyclic

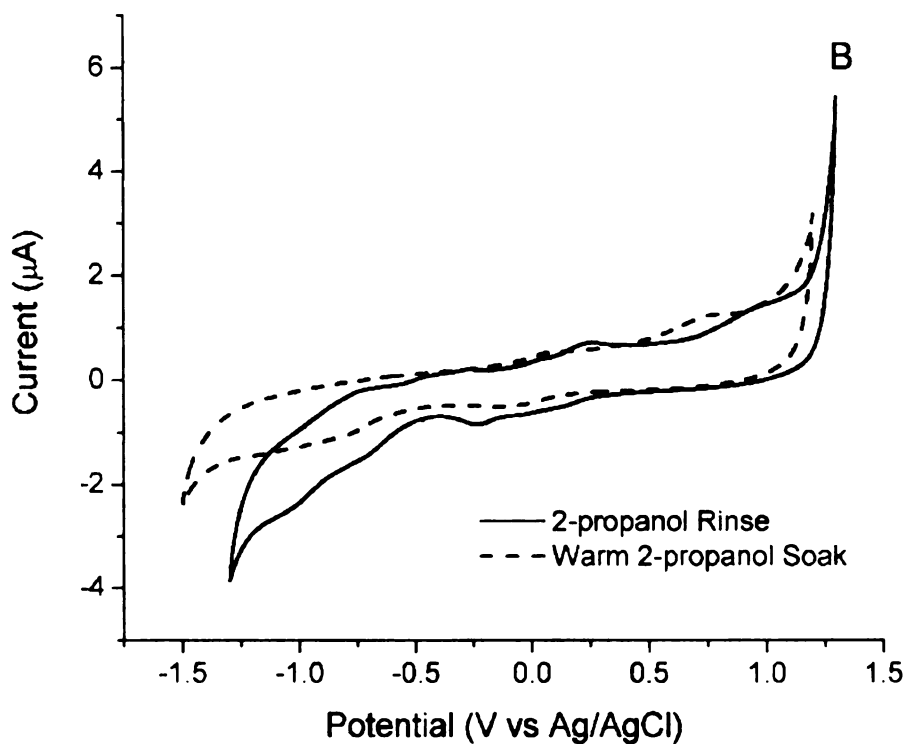
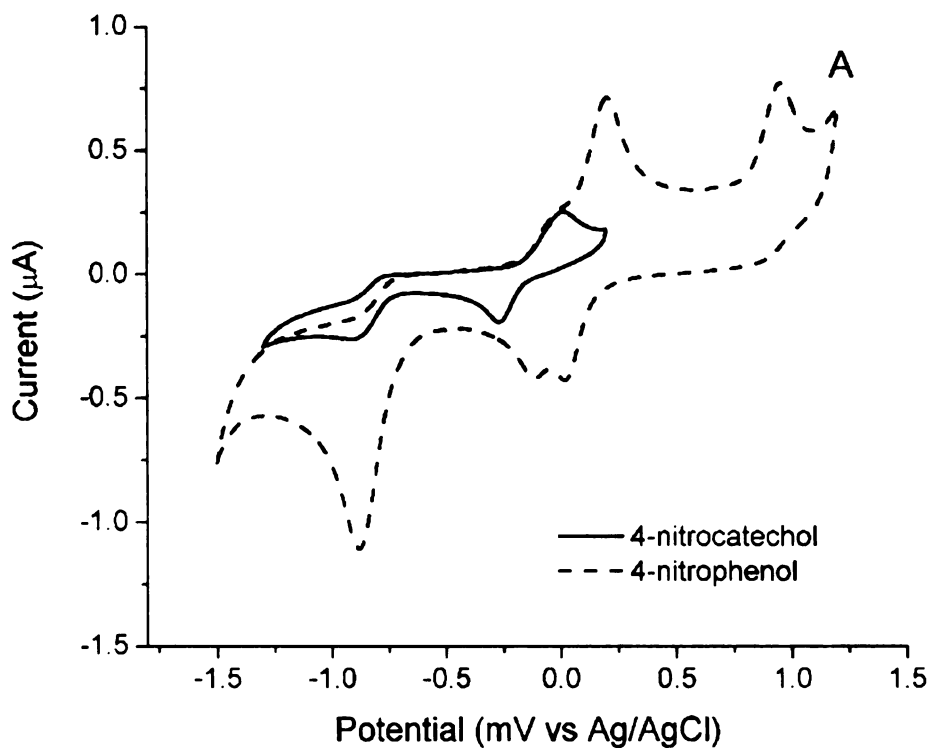


Figure 5-11. (a) Cyclic voltammetric i-E curves for 4-nitrophenol (dashed) and 4-nitrocatechol (solid). (b) Background cyclic voltammetric e-E curves after 4-np cycling and 2-propanol rinse (solid) and warm 2-propanol soak (dashed). Scan rate = 50 mV/sec.

voltammetric i-E curves for 4-nitrocatechol were measured. This is the expected molecule resulting from a transfer of a hydroxyl group to 4-nitrophenol, as the existing phenol group is an ortho director, and the nitro group is a meta director. Figure 5-11A shows a cyclic voltammetric i-E curve for a 0.05 mM solution of 4-nitrocatechol in 10 mM phosphate buffer, pH 8.0. The large reduction peak is shifted negative, as is the nitroso redox couple. When overlaid with a trace for a cyclic voltammetric i-E curve of 4-nitrophenol measured at the same conditions, the 4-nitrocatechol peaks roughly correspond with the peaks that appear in the 4-nitrophenol curve after cycling to positive far potentials where the phenol group is oxidized, supporting the assignment of these current features to a catechol species containing a nitro group.

Further supporting the anodic oxygen transfer is evidence electroactive reaction products species remain after rinsing the electrode with distilled 2-propanol. Polymerization of phenolic compounds following anodic oxygen transfer has been reported at metal and polished glassy carbon electrodes.^{116, 123} Muna *et al* reported self-polymerization in the electro-oxidation of chlorophenols at diamond electrodes.⁴³ In Figure 5-11B, background cyclic voltammetric i-E curves are presented in 10 mM pH = 8 phosphate buffer. The solid trace was recorded following the above cyclic voltammetric i-E curves and rinsing of the electrode with distilled 2-propanol. Cathodic features are observed at 0V and -0.2 V, as well as an anodic peak at +0.2 V. The dashed trace demonstrates that

these features can be removed by soaking the electrode for 20 minutes in *warm* distilled 2-propanol, as reported in the case of chlorophenols at diamond.

5.4 Conclusion

The voltammetry for three nitrophenols was investigated at boron-doped diamond electrodes. These molecules serve as models for a proposed spectroelectrochemical measurement method, using the diamond/quartz OTE, for nitrotoluene pollutants. 2-nitrophenol, 4-nitrophenol, and 2,4-dinitrophenol may be distinguished from one another by their slightly different voltammetric signatures. Preliminary measurements indicate that they may also be distinguished by differences in their absorption spectra in the 225-300 nm range. The negative potentials necessary to reduce these nitrophenols is more negative than the stable potential window of the ITO/quartz OTE. The spectroscopic features that distinguish the molecules in UV-Vis are in the 200-300 nm wavelength range, below the transparent range of ITO.

The cyclic voltammetric *i*-*E* curves for 2-nitrophenol and 4-nitrophenol have the same shape as curves reported for nitrobenzene at GC. A large reduction current is observed when potential is swept negative of ca. -800 mV, corresponding to the reduction of the nitro group to a hydroxylamine group. On subsequent cycles, a redox couple appears centered at ca. 0 V, presumably representing the oxidation of the hydroxylamine group to a nitroso group, and the reduction back to hydroxylamine. The ΔE_p for this couple is ca. 150 mV for 4-

nitrophenol, and over 600 mV for 2-nitrophenol. Peak currents for the large reduction wave for 4-nitrophenol at diamond scale linearly with the square root of scan rate, indicating semi-infinite linear diffusion of the analyte. However, a comparison of observed peak current magnitudes for the large reduction wave to theoretical values indicate that either (i) the electrochemically active area of the diamond electrodes is ca. 50% of the geometric area, or (ii) the reaction that occurs at this wave involves two electrons, not four electrons as shown for nitrobenzene at GC. In the limited pH range studied in this research, no trend is observed in changes to the peak currents of 4-nitrophenol with pH. If the reaction mechanism is the same as that reported at GC, Au, and Hg, the peak potentials are expected to shift 60 mV/pH unit. A more detailed study of the effect of pH is proposed to determine the role of protons in the reaction mechanism. While the redox reaction mechanism of the nitro groups of 2,4-dinitrophenol at diamond is still under investigation, the results may be summarized as a combination of the features of nitro reduction representing both the nitro groups, ortho and para, to the phenol group.

The redox reaction mechanisms of the nitrophenols is complicated by the addition of the phenol group to the aromatic ring. If potentials sufficiently positive for phenol oxidation are not reached, cyclic voltammetric *i*-*E* curves resemble those at GC, and reflect the electrochemistry proposed from polarography at mercury. When the phenol groups are oxidized, two complications are added. First, new, nitrated species with slightly different nitro group reduction

overpotentials are produced. Second, there is evidence of polymerization at the electrode surface caused by oxidation, depositing electroactive products on the electrode surface, as reported by Muna et al. These deposits are readily removed by soaking in warm solvent.

6 Conclusions

The goal of the present work was to develop and characterize a new boron-doped diamond thin-film on quartz in order to better exploit the superb optical properties of the material in the UV-Vis range. The first research question was whether adherent diamond thin-films could be reproducibly coated on quartz substrates. Chapter 2 demonstrated that adherent boron-doped diamond thin-films can be reproducibly deposited on quartz using microwave plasma chemical vapor deposition (MPCVD). Deposition conditions were a 0.5% CH₄/H₂ source gas mixture containing 1 to 10 ppm B₂H₆ (200 sccm total gas flow), a system pressure of 45 Torr, and a microwave power of 800 W. Raman spectroscopy confirmed the presence of a boron-doped diamond film. Atomic force microscopy revealed a crystallite size in the 100-300 nm range, and a surface roughness of 13 nm (rms).

The second research question was to determine the critical deposition parameters for an adherent and continuous film on quartz. Chapter 2 demonstrated that the two critical deposition parameters are (i) mechanical scratching and (ii) cleaning pretreatment of the quartz substrate prior to growth. Scratching was achieved by polishing the substrates with a diamond powder/water slurry. The high density of surface striations promotes a high instantaneous nucleation density, which leads to deposition of a continuous film of small microcrystallites (100-300 nm) in a short growth time. The meticulous cleaning of polishing debris from the surface striations prevents the large (up to

1000 um) diamond polish particles from serving as nucleation centers.

The third research question was to determine the optical, electronic, and electrochemical properties of the diamond/quartz OTE. Chapter 3 demonstrated that diamond/quartz OTEs have optical, electronic and electrochemical properties that may be adjusted for specific application through modifications in the deposition conditions. The boron doping level was adjusted so as to maximize the electrical conductivity while maintaining relatively high the optical transparency.

The ideal OTE would have optical properties allowing efficient transmission of light at the wavelengths of interest. The diamond/quartz OTE exhibited a useful optical window in the UV-visible region from ca. 225 to 900 nm. The transmission varied between 10 and 45% between 225 and 400 nm, and remained relatively constant at 50% from 400 to 900 nm. Loss of transmitted light was due mostly to reflection and absorption. The periodic variation in transmission was found to be due to reflection of light incident upon the film, varying from 0 to 20% across the 225 to 900 nm window. Absorption due to nitrogen impurities limited transmission from 20 to 80% from 225 to 300 nm. Absorption due to the boron dopant band limited transmission to ca. 40% from 600 to 900 nm.³⁹ The surface features (100 to 200 nm) were smaller than the wavelengths of light measured (225 to 900 nm), limiting the contribution of scattering to transmission losses.

The ideal OTE would have a sufficiently low resistivity to enable the measurements of rapid electron transfer kinetics. The resistivity varies inversely with carrier concentration and carrier mobility.⁶⁴ The dopant concentration of 10 ppm in the source gas mixture was chosen for a sufficiently conductive diamond thin-film. The diamond/quartz OTE has a high carrier concentration, 10^{20} cm^{-3} (holes), and low electrical resistivity ($0.058 \text{ } \Omega\text{-cm}$) laterally through the grains and grain boundaries. The film resistivities are ca. one order of magnitude higher than boron-doped polycrystalline films deposited under similar conditions on Si, due to the low carrier mobility (grain boundary scattering). However, the resistivity is low enough to allow for the measurement of relatively fast electron transfer reaction kinetics. In other words, the film resistivity is low enough such that ohmic effects do not severely distort the i-E curves.

The ideal OTE would have the following electrochemical properties: good electrical conductivity, a wide and stable potential window, a low and stable background current, and good activity for redox systems without the need for pretreatment. The electrochemical properties were similar to those reported for other high quality boron-doped diamond thin-film electrodes. This includes a wide potential window of nearly 3 V in aqueous solution, a low and stable background current, and fast, good electrochemical responsiveness for $\text{Fe}(\text{CN})_6^-$, $^{3/4}$, $\text{Ru}(\text{NH}_3)_6^{+2/+3}$, and $\text{CPZ}^{0/+}$. CP-AFM measurements indicate that the actual electrochemically active area is ca. 50% of the nominal area, which was further

confirmed by the i_p^{ox} of cyclic voltammetric i-E curves for $Fe(CN)_6^{-3/4}$. This is an important finding as the surfaces are not uniformly conducting.

The fourth research question was whether the diamond/quartz film could be used as an OTE to make reproducible spectroelectrochemical measurements in the UV-Vis region of the electromagnetic spectrum. In Chapter 3, the spectroelectrochemical performance of the diamond OTE was evaluated in a specially designed, thin-layer cell, using chlorpromazine. Well-defined, thin-layer voltammetry was observed with Q_p^{ox} values independent of scan rate, as expected for thin-layer behavior. For CPZ measurements, the linear dynamic range was from 20 to 100 μM and the estimated limit of detection was 0.5 μM (S/N = 3). A linear Nernst plot was observed with a slope of 56.9 mV, reflective of 1 electron being transferred per equivalent during the oxidation of CPZ and CPZ⁺ and an ordinate intercept of 0.41 V.

In order for the diamond/quartz OTE to be practical for application, it must also possess superb optical and electrochemical stability in a wide variety of chemical environments. The fifth research question was how the diamond/quartz OTE compared to the most commonly used OTE material, ITO in optical and electrochemical property stability. The results of Chapter 4 demonstrate that the diamond/quartz OTE possesses material property stability far superior to that of ITO. The diamond/quartz OTE shows superb chemical stability in harsh chemical environments. ITO optical and electrochemical properties are unstable

during exposure to dichloromethane, strongly acidic or basic solutions (some batches), and polarization at negative potentials greater than -1 V. ITO/quartz OTE optical and electrochemical properties began to resemble those of the substrate as treatment progressed in time. In comparison, boron-doped diamond thin-films are optically and electrochemically stable under these conditions. After potential cycling in 1 M NaOH and 1 M HNO₃ for over two hours each, optical properties, film morphology, and resistivity of the films were unaffected. The diamond/quartz OTEs exhibit superb electrochemical stability under this harsh chemical treatment, as the electrochemistry of Fe(CN)₆^{-3/-4} and Ru(NH₃)₆^{+2/+3} at these electrodes remains active after the polarization treatment.

While Chapter 4 more accurately detailed the conditions under which the ITO/quartz OTE is chemically unstable than has previously been reported, the nature of the chemical change occurring at the ITO/quartz surface during polarization in 1 M NaOH is still not clear.

In a step toward toward the development of a spectroelectrochemical measurement method for nitroaromatics utilizing the diamond/quartz OTE, the electrochemical behavior of three nitrophenols was investigated. Nitrophenols serve as models for other nitroaromatic compounds, such as nitrotoluenes. The cyclic voltammetric i-E curves for 2-nitrophenol and 4-nitrophenol have a shape similar to curves reported for nitrobenzene at GC, Au, and Hg electrodes,^{106, 107} including an irreversible reduction of the nitro group at potentials negative of -700

mV. This reduction wave is attenuated (up to 50%) on subsequent cycles. The initial peak current can be regained by agitating the solution. This means that the response attenuation is not due to permanent electrode fouling. While the redox reaction mechanism of the nitro groups of 2,4-dinitrophenol at diamond is still under investigation, the current results may be summarized as a combination of the features for the reduction of both the nitro groups (2-nitro and 4-nitro).

The redox reaction mechanism for the nitrophenols is complicated by the presence of the phenol group. When the phenol groups are oxidized, two complications are added. First, new nitrated species with slightly different nitro group reduction overpotentials are produced. Second, there is evidence of polymerization at the electrode surface caused by the oxidation, which results in the deposition of electroactive products on the electrode surface, as reported by Muna et al.⁴³ These deposits are readily removed by soaking in warm solvent.

7 References

- (1) Lopez-Palacios, J.; Colina, A.; Heras, A.; Ruiz, V.; Fuente, L. *Anal. Chem.* **2001**, *73*, 2883-2889.
- (2) Gui, J. Y.; Hance, G. W.; Kuwana, T. *J. Electroanal. Chem. Interfacial Electrochem.* **1991**, *309*, 73-89.
- (3) Dunphy, D. R.; Mendes, S. B.; Saavedra, S. S.; Armstrong, N. R. *Anal. Chem.* **1997**, *69*, 3086-3094.
- (4) Shi, Y.; Slaterbeck, A. F.; Seliskar, C. J.; Heineman, W. R. *Anal. Chem.* **1997**, *69*, 3679-3686.
- (5) Pruiksma, R.; McCreery, R. L. *Anal. Chem.* **1979**, *51*, 2253-2257.
- (6) Heineman, W. R.; Norris, B. J.; Goetz, J. F. *Anal. Chem.* **1975**, *47*, 79-84.
- (7) Norris, B. J.; Meckstroth, M. L.; Heineman, W. R. *Anal. Chem.* **1976**, *48*, 630-632.
- (8) Kenyhercz, T. M.; DeAngelis, T. P.; Norris, B. J.; Heineman, W. R.; Mark, H. B., Jr. *J. Am. Chem. Soc.* **1976**, *98*, 2469-2477.
- (9) Landrum, H. L.; Salmon, R. T.; Hawkridge, F. M. *J. Am. Chem. Soc.* **1977**, *99*, 3154-3158.
- (10) Sorrels, J. W.; Dewald, H. D. *Anal. Chem.* **1990**, *62*, 1640-1643.
- (11) Flowers, P. A.; Maynor, M. A.; Owens, D. E. *Anal. Chem.* **2002**, *74*, 720-723.
- (12) Norvell, V. E.; Mamantov, G. *Anal. Chem.* **1977**, *49*, 1470-1472.
- (13) Kuwana, T.; Darlington, R. K.; Leedy, D. W. *Anal. Chem.* **1964**, *36*, 2023-2025.

- (14) Meyerstein, D.; Hawkridge, F. M.; Kuwana, T. *J. Electroanal. Chem. Interfacial Electrochem.* **1972**, *40*, 377-384.
- (15) Cohen, D. H.; King, B. C.; Hawkridge, F. M. *J. Electroanal. Chem.* **1998**, *447*, 53-62.
- (16) Bradshaw, J. T.; Mendes, s. B.; Armstrong, N. R.; Saavedra, S. S. *Anal. Chem.* **2003**, *75*, 1080-1088.
- (17) Stotter, J.; Zak, J.; Behler, Z.; Show, Y.; Swain, G. M. *Anal. Chem.* **2002**, *74*, 5924-5930.
- (18) Kirkov, P. *Electrochim. Acta* **1972**, *17*, 533-547.
- (19) Kirkov, P. *Electrochim. Acta* **1972**, *17*, 519-532.
- (20) Bundy, F. P.; Hall, H. T.; Strong, H. M.; Wentorf, R. H., Jr. *Nature* **1955**, *176*, 51-55.
- (21) Angus, J. C.; Hayman, C. C. *Science* **1988**, *241*, 913-921.
- (22) Collins, A. T. *J. Phys.: Condens. Matter* **2002**, *14*, 3743-3750.
- (23) Ager, J. W., III; Walukiewicz, W.; McCluskey, M.; Plano, M. A.; Landstrass, M. I. *Appl. Phys. Lett.* **1995**, *66*, 616-618.
- (24) Gonon, P.; Gheeraert, E.; Deneuille, A.; Fontaine, F.; Abello, L.; Lucazeau, G. *J. Appl. Phys.* **1995**, *78*, 7059-7062.
- (25) Pleskov, Y. V.; Sakharova, A. Y.; Krotova, M. D.; Builov, L. L.; Spitsyn, B. *V. J. Electroanal. Chem. and Interfac. Electrochem.* **1987**, *228*, 19-27.
- (26) Landstrass, M. I.; Ravi, K. V. *Appl. Phys. Lett.* **1989**, *55*, 1391-1393.
- (27) Huang, B. R.; Reinhard, D. K. *Appl. Phys. Lett.* **1991**, *59*, 1494-1496.

- (28) Tzeng, Y.; Teh, C. K.; Phillips, R.; Joseph, A.; Srivinyunon, T.; Cutshaw, C.; Tin, C. C.; Miller, R.; Hartnett, T. H.; et al. *NATO ASI Ser., Ser. B* **1991**, *266*, 805-812.
- (29) Mermoux, M.; Roy, F.; Marcus, B.; Abello, L.; Lucazeau, G. *Diamond Relat. Mater.* **1992**, *1*, 519-524.
- (30) Mehandru, S. P.; Anderson, A. B. *J. Mater. Res.* **1994**, *9*, 383-395.
- (31) Swain, G. M.; Ramesham, R. *Anal. Chem.* **1993**, *65*, 345-351.
- (32) Strojek, J. W.; Granger, M. C.; Swain, G. M.; Dallas, T.; Holtz, M. W. *Anal. Chem.* **1996**, *68*, 2031-2037.
- (33) Fausett, B.; Granger, M. C.; Hupert, M. L.; Wang, J.; Swain, G. M.; Gruen, D. M. *Electroanalysis* **2000**, *12*, 7-15.
- (34) Pleskov, Y. V.; Mazin, V. M.; Evstefeeva, Y. E.; Varnin, V. P.; Teremetskaya, I. G.; Laptev, V. A. *Electrochim. Solid-State Lett.* **2000**, *3*, 141-143.
- (35) Mora, A. E.; Steeds, J. W.; Butler, J. E. *Diam. Rel. Mater.* **2002**, *11*.
- (36) Pleskov, Y. V.; Krotova, M. D.; Ralchenko, V. G.; Khomich, A. V.; Khmelnitskiy, R. A. *Electrochim. Acta* **2003**, *49*, 41-49.
- (37) Holt, K. B.; Bard, A. J.; Show, Y.; Swain, G. M. *J. Phys. Chem. B* **2004**, *108*, 15117-15127.
- (38) Pankove, J. I.; Qiu, C.-H. In *Synthetic Diamond: Emerging CVD Science and Technology*; Spear, K. E., Dismukes, J. P., Eds.; Wiley: New York, 1994, pp 401-418.
- (39) Tzeng, Y. *Diamond Films Technol.* **1991**, *1*, 31-54.
- (40) Wang, J.; Swain, G. M. *Electrochim. Solid-State Lett.* **2002**, *5*, E4-E7.

- (41) Witek, M. A.; Swain, G. M. *Anal. Chim. Acta* **2001**, *440*, 119-129.
- (42) Xu, J.; Chen, Q.; Swain, G. M. *Anal. Chem.* **1998**, *70*, 3146-3154.
- (43) Muna, G. W.; Tasheva, N.; Swain, G. M. *Environ. Sci. Technol.* **2004**, *38*, 3674-3682.
- (44) Zak, J. K.; Butler, J. E.; Swain, G. M. *Anal. Chem.* **2001**, *73*, 908-914.
- (45) Haymond, S.; Zak, J. K.; Show, Y.; Butler, J. E.; Babcock, G. T.; Swain, G. M. *Anal. Chim. Acta* **2003**.
- (46) Haymond, S.; Babcock, G. T.; Swain, G. *Electroanalysis* **2003**, *15*, 249-253.
- (47) Haymond, S.; Babcock, G. T.; Swain, G. M. *J. Am. Chem. Soc.* **2002**, *124*, 10634-10635.
- (48) Stotter, J.; Haymond, S.; Zak, J. K.; Show, Y.; Cvackova, Z.; Swain, G. M. *Electrochem. Soc. Interface* **2003**, 33-38.
- (49) Martin, H. B.; Morrison, P. W., Jr. *Electrochem. Solid-State Lett.* **2001**, *4*, E17-E20.
- (50) Kim, S.-H.; Kim, T.-G.; Kim, Y.-H.; Kim, D. U.; Lee, S. K.; Hosomi, T.; Maki, T.; Kobayashi, T. *J. Electrochem. Soc.* **2001**, *148*, C247-C251.
- (51) Ulczynski, M. J.; Wright, B.; Reinhard, D. K. *Diam. Relat. Mater.* **1998**, *7*, 1639-1646.
- (52) Granger, M. C.; Swain, G. M. *J. Electrochem. Soc.* **1999**, *146*, 4551-4558.
- (53) Bennett, J.; Wang, J.; Show, Y.; Swain, G. *J. Electrochem. Soc.* **2004**, *151*, E306-E313.
- (54) Knight, D. S.; White, W. B. *J. Mater. Res.* **1989**, *4*, 385.

- (55) Fayette, L.; Marcus, B.; Mermoux, M.; Rosman, N.; Abello, L.; Lucazeau, G. *Adv. New Diamond Sci. Technol., Int. Conf., 4th 1994*, 135-138.
- (56) Marcus, B.; Fayette, L.; Mermoux, M.; Abello, L.; Lucazeau, G. *J. Appl. Phys.* **1994**, *76*, 3463-3470.
- (57) Mermoux, M.; Marcus, B.; Swain, G. M.; Butler, J. E. *J. Phys. Chem. B* **2002**, *106*, 10816-10827.
- (58) Windischmann, H.; Epps, G. F.; Cong, Y.; Collins, R. W. *J. Appl. Phys.* **1991**, *69*, 2231.
- (59) Fayette, L.; Marcus, B.; Mermoux, M.; Rosman, N.; Abello, L.; Lucazeau, G. *J. Appl. Phys.* **1994**, *76*, 1604-1608.
- (60) Ogasawara, A.; Inushima, T.; Shiraishi, T.; Ohya, S.; Karasawa, S.; Shiomi, H. *Diam. Rel. Mater.* **1997**, *6*, 835-838.
- (61) Zaitsev, A. M. *Optical Properties of Diamond*; Springer-Verlag: Berlin, 2001.
- (62) Granger, M. C.; Witek, M.; Xu, J.; Wang, J.; Hupert, M.; Hanks, A.; Koppang, M. D.; Butler, J. E.; Lucazeau, G.; Mermoux, M.; Strojek, J. W.; Swain, G. M. *Anal. Chem.* **2000**, *72*, 3793-3804.
- (63) Bard, A. J.; Faulkner, L. R. *Electrochemical Methods: Fundamentals and Applications*; Wiley & Sons: New York, 1980.
- (64) Schroder, D. K. In *Semiconductor Material and Device Characterization*, 2nd ed.; John Wiley & Sons, Inc.: New York, 1998, pp 1-39.
- (65) Collins, A. T. *J. Phys. D: Appl. Phys.* **1982**, *15*, 1431-1438.
- (66) Miyata, K.; Kumagai, K.; Nishimura, K.; Kobashi, K. *J. Mater. Res.* **1993**, *8*, 2845-2857.
- (67) Deneuve, A. In *Thin-Film Diamond I*; Nebel, C. E., Ristein, J., Eds.; Elsevier Academic Press: New York, 2003; Vol. 76, pp 183-238.

- (68) Han, S.; Pan, L. S.; Kania, D. R. In *Diamond: Electronic Properties and Applications*; Pan, L. S., Kania, D. R., Eds.; Kluwer Academic Publishers: Boston, 1995, pp 241-284.
- (69) Malta, D. M.; von Windeim, J. A.; Fox, B. A. *Appl. Phys. Lett.* **1993**, *62*, 2926.
- (70) Show, Y.; Witek, M. A.; Sonthalia, P.; Swain, G. M. *Chem. Mater.* **2003**, *15*, 879-888.
- (71) Wang, S.; Swain, G. M. *Unpublished Results* **2004**.
- (72) Chen, P.; McCreery, R. L. *Anal. Chem.* **1996**, *68*, 3958-3965.
- (73) Chen, P.; Fryling, M. A.; McCreery, R. L. *Anal. Chem.* **1995**, *67*, 3115-3122.
- (74) Rice, R. J.; McCreery, R. L. *Anal. Chem.* **1989**, *61*, 1637-1641.
- (75) Granger, M. C.; Xu, J.; Strojek, J. W.; Swain, G. M. *Anal. Chim. Acta* **1999**, *397*, 145-161.
- (76) Yang, H.-H.; McCreery, R. L. *Anal. Chem.* **1999**, *71*, 4081-4087.
- (77) Xu, J. Doctoral Thesis, Utah State University, Logan, Utah, 1999.
- (78) Cheng, H. Y.; Sackett, P. H.; McCreery, R. L. *J. Am. Chem. Soc.* **1978**, *100*, 962-967.
- (79) Ates, S.; Somer, G. *J. Chem. Soc., Faraday Trans. 1* **1981**, *77*, 859-867.
- (80) Cheng, H. Y.; Sackett, P. H.; McCreery, R. L. *J. Med. Chem.* **1978**, *21*, 948-952.
- (81) Kuwana, T.; Winograd, N. *Electroanal. Chem.* **1974**, *7*, 1-78.

- (82) Hubbard, A. T.; Anson, F. C. *Anal. Chem.* **1966**, *38*, 58-61.
- (83) Haymond, S.; Zak, J. K.; Show, Y.; Butler, J. E.; Babcock, G. T.; Swain, G. M. *Analytica Chimica Acta* **2003**.
- (84) Stotter, J.; Zak, J. K.; Behler, Z.; Show, Y.; Swain, G. M. *Anal. Chem.* **2002**, *74*, 5924-5930.
- (85) Eisgruber, I. L.; Engel, J. R.; Hollingsworth, R. E.; Bhat, P. K.; Wendt, R. J. *Vac. Sci. Tech. A* **1998**, *17*, 190-197.
- (86) Hamberg, I.; Granqvist, C. G. *J. App. Phys.* **1986**, *60*, R123-R159.
- (87) Nadaud, N.; Lequeux, N.; Nanot, M.; Jove, J.; Roisnel, T. *J. Solid State Chem.* **1998**, *135*, 140-148.
- (88) Kirkov, P. *Electrochim. Acta.* **1972**, *17*, 519-532.
- (89) Kirkov, P. *Electrochim. Acta.* **1972**, *17*, 533-547.
- (90) Laitinen, H. A.; Vincent, C. A.; Bednarski, T. M. *Journal of the Electrochemical Society* **1968**, *115*, 1024-1028.
- (91) Elliott, D.; Zellmer, D. L.; Laitinen, H. A. *Journal of the Electrochemical Society* **1970**, *117*, 1343-1348.
- (92) Armstrong, N. R.; Lin, A. W. C.; Fujihira, M.; Kuwana, T. *Anal. Chem.* **1976**, *48*, 741-750.
- (93) Moulder, J. F.; Stickle, W. F.; Sobol, P. E. *Handbook of X Ray Photoelectron Spectroscopy*; Perkin-Elmer, Physical Electronics Division, 1993.
- (94) Donley, C.; Dunphy, D.; Paine, D.; Carter, C.; Nebesny, K.; Lee, P.; Alloway, D.; Armstrong, N. R. *Langmuir* **2002**, *18*, 450-457.
- (95) Galus, Z. In *Encyclopedia of Electrochemistry of the Elements*; Bard, A. J.,

Ed.; M. Dekker: New York, 1975; Vol. 4, pp 223-269.

- (96) Losev, V. V.; Molodov, A. I. In *Encyclopedia of electrochemistry of the elements*; Bard, A. J., Ed.; M. Dekker: New York, 1976; Vol. 6, pp 1-32.
- (97) Liao, Y.-H.; Scherer, N. F.; Rhodes, K. J. *Phys. Chem. B* **2001**, *105*, 3282-3288.
- (98) Chaney, J. A.; Pehrsson, P. E. *App. Surf. Sci.* **2001**, *180*, 214-226.
- (99) Lin, A. W. C.; Armstrong, N. R.; Kuwana, T. *Anal. Chem.* **1977**, *49*, 1228-1235.
- (100) NATO In *Scientific Affairs Newsletter*, 2002, pp 3.
- (101) US Environmental Protection Agency: Washington, DC, 2004.
- (102) Benson, B.; Foureman, G.; Hofmann, L.; Kimmel, C.; Kimmel, G.; Makris, S.; Murphy, D.; Ohanian, E.; Orme-Zavaleta, J.; Rice, D.; Seed, J.; Tilson, H.; Vu, V.; U.S. Environmental Protection Agency: Washington, DC, 2002, pp 192.
- (103) US Environmental Protection Agency: Washington, DC, 1994.
- (104) Heyrovsky, M.; Vavricka, S. *J. Electroanal. Chem.* **1970**, *28*, 409-420.
- (105) Lund, H. In *Organic Electrochemistry: An Introduction and a Guide*; Baizer, M. M., Ed.; Marcel Dekker, Inc.: New York, 1973, pp 315-345.
- (106) McIntire, G. L.; DChiappardi, D. M.; Casselberry, R. L.; Blount, H. N. *J. Phys. Chem.* **1982**, *86*, 2632-2640.
- (107) Rubinstein, I. *J. Electroanal. Chem. and Interfac. Electrochem.* **1985**, *183*, 379-386.
- (108) Silverstein, R. M.; Morrill, T. C.; Bassler, C. *Spectrometric Identification of Organic Compounds*; John Wiley and Sons, 1991.

- (109) Maizels, M.; Stegemiller, M.; Ross, S.; Slaterbeck, A.; Shi, Y.; Ridgway, T. H.; Heineman, W. R.; Seliskar, C. J.; Bryan, S. A. *ACS Symposium Series* **2001**, *778*, 364-378.
- (110) Zudans, I.; Seliskar, C. J.; Heineman, W. R. *Thin Solid Films* **2003**, *426*, 238-245.
- (111) Bowling, R.; McCreery, R. L. *Anal. Chem.* **1988**, *60*, 605-608.
- (112) Niesner, R.; Heintz, A. *J. Chem. Eng. Data* **2000**, *45*, 1121-1124.
- (113) Hu, I. F.; Karweik, D. H.; Kuwana, T. *J. Electroanal. Chem. Interfacial Electrochem.* **1985**, *188*, 59-72.
- (114) Vasquez, R. E.; Hono, M.; Kitani, A.; Sasaki, K. *J. Electroanal. Chem.* **1985**, *196*, 397-415.
- (115) Hilmi, A.; Luong, J. H.; Nguyen, A.-L. *Anal. Chem.* **1999**, *71*, 873-878.
- (116) Gattrell, M.; Kirk, D. W. *Can. J. Chem. Eng.* **1990**, *68*, 997-1003.
- (117) Gattrell, M.; Kirk, D. W. *J. Electrochem. Soc.* **1993**, *140*, 903-911.
- (118) Gattrell, M.; Kirk, D. W. *J. Electrochem. Soc.* **1993**, *140*, 1534-1540.
- (119) Gattrell, M.; Kirk, D. W. *J. Electrochem. Soc.* **1992**, *139*, 2736-2744.
- (120) Kirk, D. W.; Gattrell, M. *Proc. - Electrochem. Soc.* **1993**, *93-28*, 147-158.
- (121) Terashima, C.; Rao, T. N.; Sarada, B. V.; Tryk, D. A.; Fujishima, A. *Anal. Chem.* **2002**, *74*, 895-902.
- (122) Canizares, P.; Saez, C.; Lobato, J.; Rodrigo, M. A. *Ind. Eng. Chem. Res.* **2004**, *43*, 1944-1951.
- (123) Mengoli, G.; Musiani, M. M. *J. Electrochem. Soc.* **1987**, *134*, 643C-651C.

MICHIGAN STATE UNIVERSITY LIBRARIES



3 1293 02504 0050